Microstructured fibers with liquid crystals: Tuning of optical transmission and dispersion

Von der Naturwissenschaftlichen Fakultät
der Universität Paderborn genehmigte
Dissertation
zur Erlangung des akademischen Grades
Doktor der Naturwissenschaften
– Dr. rer. nat. –

vorgelegt von

Markus Wahle

Paderborn, 2017

Inhaltsverzeichnis

Summary

Liquid crystal filled optical fibers offer multiple ways to control optical signals by actively modulating the optical properties of the liquid crystal. This thesis describes the coupling of light guided inside a solid glass core fiber with liquid crystal filled inclusions. By applying an external electric field, the interaction of the guided light with the liquid crystal can be controlled.

The first part of this thesis is concerned with microstructured optical fibers, which consist of a solid glass core and a single liquid crystal inclusion. The investigation of these microstructured fibers is focused on the characterization of electrically induced polarization effects of light in the visible and infrared spectrum. The experimental results are compared to the predictions of the coupled mode theory.

In the second part, photonic crystal fibers are investigated. These fibers possess a central glass core, which is surrounded by a periodic array of liquid crystal inclusions. The main focus lies on the propagation characteristics of optical pulses such as group velocity and dispersion. These properties can be influenced by an external electric field. Finally, the possibility of four wave mixing in these fibers is discussed, which would allow for an electrically tunable frequency conversion.

Zusammenfassung

Flüssigkristall-gefüllte optische Fasern bieten vielseitige Möglichkeiten optische Signale zu kontrollieren, da die optischen Eigenschaften von Flüssigkristallen aktiv moduliert werden können. Die vorliegende Dissertation beschreibt Untersuchungen zur Kopplung von lichtleitenden Glaskernen in optischen Fasern mit integrierten Flüssigkristallinklusionen. Durch das Anlegen von externen elektrischen Feldern kann die Interaktion des geführten Lichts mit dem Flüssigkristall kontrolliert werden.

Der erste Teil dieser Arbeit ist mikrostrukturierten Fasern gewidmet, die aus einem festen Glaskern und einer einzelnen Flüssigkristallinklusion bestehen. Der Fokus der Untersuchung dieser mikrostrukturierten Fasern liegt auf der Charakterisierung von elektrisch induzierten Polarisationseffekten im sichtbaren und im infraroten Spektralbereich. Die experimentellen Ergebnisse werden mit den Vorhersagen der Theorie der gekoppelten Moden verglichen.

Im zweiten Teil werden photonische Kristallfasern behandelt. Diese Fasern besitzen einen Glaskern, welcher von einer periodischen Anordnung von Flüssigkristallinklusionen umgeben ist. Das Hauptaugenmerk liegt dabei auf den Ausbreitungseigenschaften von optischen Pulsen wie Gruppengeschwindigkeit und Dispersion. Diese Charakteristika können durch das Anlegen elektrischer Felder an die Flüssigkristallinklusionen beeinflusst werden. Abschließend wird die Möglichkeit der Vierwellenmischung in diesen Fasern diskutiert. Dies würde eine elektrisch justierbare Frequenzkonversion erlauben.

Chapter 1

Introduction

Optical fibers and liquid crystals share a similar timeline with regards to their historical development. They both have been discovered in the second half of the 19th century but both needed about 100 years to revolutionize their respective commercial fields. Optical fibers are nowadays ubiquitous in modern telecommunication systems as liquid crystals are as display materials.

In the last two decades, the progress in manufacturing optical fibers made it possible to combine fiber technology with liquid crystals. This is possible due to the invention of photonic crystal fibers and the consequent development of more versatile designs in microstructured optical fibers. The combination of optical fibers and liquid crystals leads to highly tunable waveguiding structures. Here, we want to give a very brief overview on the historical developments of optical fibers and liquid crystals.

1.1. History of optical fibers

The history of optical fibers dates back to the 1840s when Daniel Colladon and Jacques Babinet proved that light can be guided within jets of water [1]. The light followed the curvature of the jets due to total internal reflection at the water-air interface and could be observed on the receiving end. From here on it still took more than 100 years until in the 1960s and 1970s the first low loss optical fibers as we know them today were produced [2].

After this milestone, the research in optical fibers spiked. Much of the fundamental theoretical framework on the transmission through optical fibers based on solving Maxwell's equations was done by Gloge [3–5], Marcuse [6–8] and Snyder [9–11].

The next important step in the development of optical fibers was established in the 1990s when photonic crystal fibers (PCFs) were invented [12, 13]. These fibers guide light due to a photonic cladding, which usually is made of multiple air inclusion

in a periodic array. The light guiding core is then formed by a defect, e. g. a missing air inclusion [14–16].

Even though these fibers can be modeled reasonably well as step index fibers, they have unique properties like endlessly single mode behavior and a constant mode field diameter over a broad wavelength range. Due to the broadband single mode behavior, these fibers are employed in the delivery of high optical powers by utilizing large core sizes, which minimizes non-linear optical effects [17]. In contrast, these fibers are designed to promote non-linear optical effects by small core sizes. This concept is used in supercontinuum lasers [18–20].

With the expertise gained in producing photonic crystal fibers, other geometries were explored. This led to so-called microstructured optical fibers (MOFs). The MOFs we will be interested in are especially simple in design. They are basically step index fibers with a solid core and a single hollow inclusion running parallel to to the core. These fibers have been used to study the optical properties of liquids [21] and the excitation of plasmons in gold nanowires [22].

1.2. History of liquid crystals

Liquid crystal research started out as a purely scientific topic since their discovery in 1888 by Austrian chemist Friedrich Reinitzer [23], who turned to German physicist Otto Lehmann [24] for help in the interpretation his findings. During his investigations of cholesteryl derivatives he discovered a the liquid crystalline phase, which showed blue reflections which indicated some kind of order but it was a liquid.

It took a considerable amount of time until the commercial interest in liquid crystals rose in the 1960s. The breakthrough came in the 1970s with the developement if liquid crystal displays (LCDs) [25]. At the time LCDs started to replace the cathode ray tubes and still today most TVs use LCDs.

Even though liquid crystals have their main application in display technology, they have spread to other fields. One example are liquid crystal based spatial light modulators (SLMs), which are devices with an electrical addressable liquid crystal array. These devices are used to modulate the phase of incoming light. SLMs can be used to shape optical pulses or the spatial shape of beams. The two-dimensional SLM arrays are commonly used to generate computer-controlled holograms [26].

1.3. Photonic crystal fibers, microstructured optical fibers & liquid crystals

It was soon realized that the combination of photonic crystal fibers and liquid crystals (LCs) has great potential due to the tuning capabilities of the LC. The infiltration of photonic crystal fibers with LCs has led to numerous inventions relying on the strong response of LCs to external stimuli. The tuning of the transmission through

these fibers by electric fields [27–29] or by thermal changes [30–32] are among the most common methods.

For optical devices, external electric fields are preferred as they are much faster compared to thermal tuning. Among these tunable devices are polarizers [29, 33], tunable attenuators [34, 35] and phase shifter [36].

However, due to the complicated structure of LCPCFs it is difficult to find an accurate analytic description. Therefore, to understand the basic interactions between a waveguide and liquid crystals it is useful to study microstrucured optical fibers (MOFs), which possess a much more simple structure. Consquently, the first part of this thesis is devoted to the investigation of the optical properties of LC filled MOFs and how these properties can be tuned electrically.

The complicated structure of the LCPCFs lead to unique properties regarding group velocity and dispersion of optical pulses due to the photonic cladding. Some of these properties have been invesitgated for PCFs made from glass [37–39]. But so far they have not been investigated in LCPCFs, thus the tuning capabilities have not been utilized. Thus, our research on the electrical control of the dispersion properties of LCPCFs will form the second part of this thesis.

The thesis is therefore organized as follows. After introducing the basic properties of liquid crystals in Chap. 2, we turn to the basic description of optical waveguides. Especially the coupling between different waveguides will be discussed in Chap. 3. In Chap. 4, we describe the experiments and the results obtained for the liquid crystal filled microstructured optical fibers. Here, the focus lies on the interaction of the solid core and the liquid crystalline inclusion and how the interaction can be controlled by external electric fields. In Chap. 5, we move to liquid crystal filled photonic crystal fibers and focus on the group delay and dispersion properties of these fibers. Finally, in the Chap. 6, we conclude this thesis and give an outlook to how this work can be continued in the future.

Part I.

Theoretical background

Chapter 2

Liquid crystals

2.1. Basic properties of nematic liquid crystals

Most people are aware of three states of matter, namely solid, liquid and gaseous. But between the solid and the liquid phase a multitude of different states of matter can be found which are called *mesophases*[†]. These mesophases form due to anisotropic interactions between molecules.

Liquid crystalline phases are an example of such mesophases. They are formed by molecules with a strongly anisometric shape. In the simplest case the liquid crystal (LC) molecules can be represented by a rod as shown in Fig. 2.1 for the molecule 5CB (4-pentyl-4'-cyanobiphenyl). This model is justified by the stiff biphenyl group.

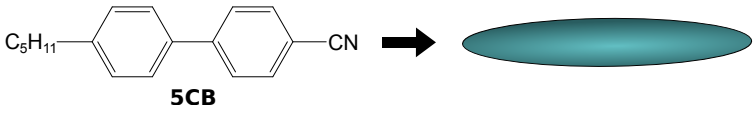

Figure 2.1. Molecular structure of the liquid crystalline molecule 5CB and its representation as a simple rod.

If we consider the bulk phase consisting of an ensemble of molecules displayed in Fig. 2.1 , we find three different condensed phases. At low temperatures, there exists a crystalline phase, in which – under the assumption of a perfect crystal – all molecules have fixed position and perfectly aligned parallel to each other [Fig. 2.2 (a)]. At sufficiently high temperatures, we find an isotropic phase, in which the molecules do not have a fixed position but are somewhat randomly distributed throughout the space. Also, in the isotropic phase we do not find an orientational order. The direction of the molecules is arbitrary.

Between these two phases a third phase exist [Fig. 2.2 (b)], which is called the *nematic* phase. In this state, the molecules exhibit a preferred direction due to

[†]From Ancient Greek (mésos, "middle")

their anisotropic intermolecular interaction. This type of order is therefore called a directional order. The nematic phase does not have a positional order unlike the crystalline state but it can flow like a liquid.

There exist many more liquid crystalline phases which form due the specific interactions of the molecules. For example, in a smectic phase the molecules additionally to the orientational order assemble into layers instead of being randomly distributed [40]. There even exist LCs which form three dimensional structure but still retain their fluidity. Those truly liquid crystals are called blue phases [41]. For this thesis, only the nematic phase is of importance. Consequently we will focus on this phase in the following.

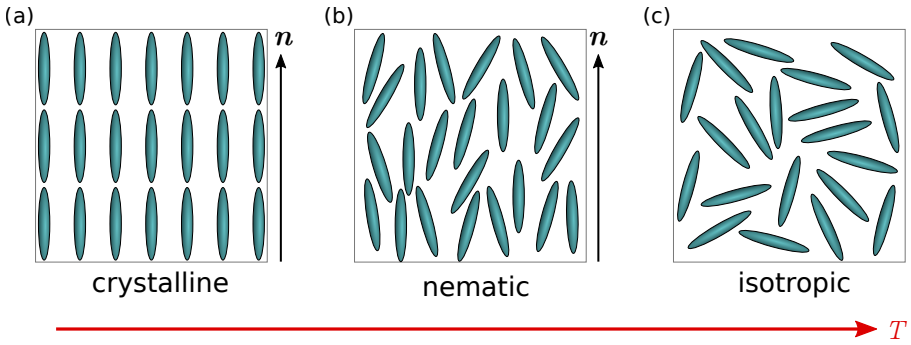

Figure 2.2. Schematic of the different phases of a liquid crystalline material upon heating. The director $\boldsymbol{n}$ can be assigned in the crystalline and liquid crystalline phases.

As already mentioned, in the nematic phase the LC molecules are oriented along a common direction which is given by the director $\boldsymbol{n}$ [cf. Fig. 2.2 (b)]. The director is a unit vector and depends on the position $\boldsymbol{r}$ within the medium

$$\boldsymbol{n} = \boldsymbol{n}(\boldsymbol{r}), \quad \boldsymbol{n} \cdot \boldsymbol{n} = 1, \quad \text{with } \boldsymbol{r} \in \mathbb{R}^3. \tag{2.1}$$

The transformation $\boldsymbol{n} \to -\boldsymbol{n}$ does not effect any of the physical properties of the nematic phase, thus the sign of $\boldsymbol{n}$ does not play a role. The director then fulfills the definition of a pseudovector. This is again in agreement with modeling the molecules as rods.

2.1.1. Order parameter

The orientational order indicated by the director in the nematic phase is not perfect. The molecular axes assumes a non-zero angle to the director $\boldsymbol{n}$ (Fig. 2.3), which averages out to zeros. The deviations are caused by thermal fluctuations and they increase with increasing temperature as the deviations are Boltzmann distributed [42, 43]. At high temperatures the orientational order breaks down and the LC undergoes a phase transition to the isotropic phase. A measure for the orientational

order is the scalar order parameter S, which was introduced by Tsvetkov [44]

$$S = \frac{1}{2}\left\langle 3\cos^2\theta - 1 \right\rangle . \tag{2.2}$$

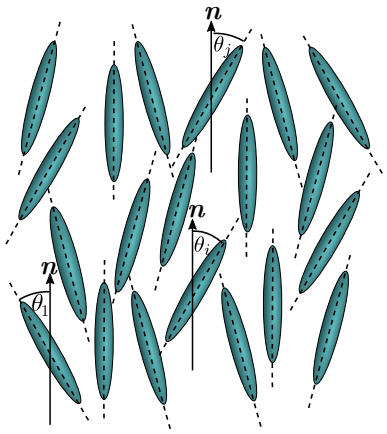

Figure 2.3. Orientational distribution of liquid crystal molecules, which assume the angles θ_k, $k = 1, \ldots, i, j, \ldots$ with respect to the average director $\boldsymbol{n}$.

For a perfectly ordered crystal, Eq. (2.2) gives $S = 1$. For total disorder, i. e., when each angle is equally probable, $S = 0$ holds. The order parameter for the nematic LC phase typically lies between 0.4 and 0.8.

Maier and Saupe derived a universal fit for S [42] whose only parameter is the phase transition temperature T_{NI} between the nematic and the isotropic phase

$$S(T) = (1 - 0.98\,T_{\mathrm{red}})^{0.22} \quad \text{with} \quad T_{\mathrm{red}} = \frac{T v^2}{T_{\mathrm{NI}} v_{\mathrm{NI}}^2}, \tag{2.3}$$

where T is the temperature, v the mole volume and v_{NI} the mole volume at the phase transition. Figure 2.4 shows the order paramter S as a function of temperature calculated via Eq. (2.3). The order parameter is continuously decreasing until $T_{\mathrm{red}} = 1$ is reached, which is the point of phase transition. At this point the order parameter discontinuously drops to zero. The nematic order is lost and the system enters the isotropic state. Equation (2.3) is not valid here.

2.1.2. Anisotropic properties

The orientational order in the nematic phase has strong effect on many material properties. In the nematic phase, properties like viscosity, refractive index and dielectric permittivities depend on the orientation of the director $\boldsymbol{n}$. For example, there are two permittivities: $\epsilon_{\parallel}$ if the electric field is parallel to the director ($\boldsymbol{E} \parallel \boldsymbol{n}$) and $\epsilon_{\perp}$ if $\boldsymbol{E} \perp \boldsymbol{n}$.

The difference between the two permittivities is a very important property for liquid crystal displays (LCDs) as it characterizes the response of the nematic phase

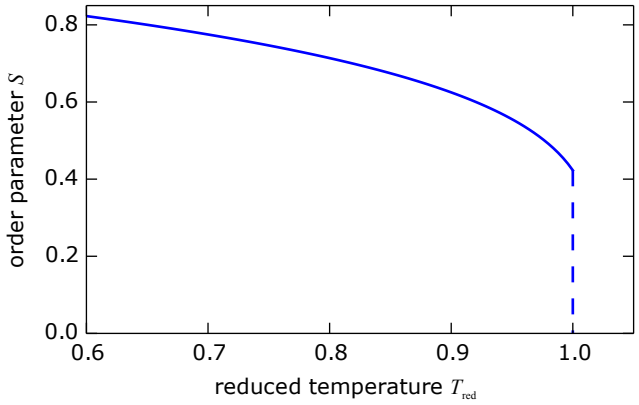

Figure 2.4. The order parameter S as a function of T_{red}.

to an external electric field. It therefore has its own name: the dielectric anisotropy

$$\Delta\epsilon = \epsilon_{\parallel} - \epsilon_{\perp}. \tag{2.4}$$

We will discuss the details of the permittivites in greater detail in Sec. 2.2.1.

Typically, the dielectric permittivites are used to describe the interaction with electric fields at low frequencies (0 Hz to 10^6 Hz). When we go to higher frequencies like the optical regime (10^{14} Hz to 10^{15} Hz), we often use the refractive index

$$n^2 = \epsilon. \tag{2.5}$$

Similar to the permittivities, the refractive index is also anisotropic. The refractive indices are labeled the ordinary refractive index ${n_{\mathrm{o}}}^2 = \epsilon_{\perp}$ and the extraordinary refractive index ${n_{\mathrm{e}}}^2 = \epsilon_{\parallel}$. These notations origin from the optical properties of solid crystals. The difference of n_{o} and n_{o} was named the optical anisotropy or birefringence

$$\Delta n = n_{\mathrm{e}} - n_{\mathrm{o}} \tag{2.6}$$

The birefringence is a key feature of LCDs. We will discuss the basic principle of LCDs in connection to the birefringence in Sec. 2.3.

2.1.3. Losses due to light scattering

Optically transparent media scatter light due to density fluctuations inside the medium. In liquid crystals additionally to the density fluctuations we have fluctuations in the order parameter. Due to the optical anisotropy, this leads to extremely strong light scattering compared to isotropic liquids. Figure shows a nematic LC sample which appears white due to the scattering

The strong scattering poses a problem for pure LC waveguides [45] and also for LC filled photonic crystal fibre. According to de Gennes, the amplitudes of the

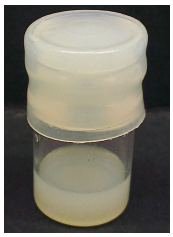

Figure 2.5. Liquid crystal mixture MLC2048. The white color originates from light scattering due to differently aligned liquid crystal domains.

fluctuations can be derived from the equipartition theorem [46]. Based on this approach, Hu and Whinnery [45] derived an approximate formula for the attenuation due to these fluctuations which can be described by an imaginary refractive index $n^{\imath}$

$$n^{\imath} = \frac{k_{\mathrm{B}}T}{8K\lambda}\frac{n_{\mathrm{e}}^2 - n_{\mathrm{o}}^2}{n_{\mathrm{o}}^2}\frac{1}{\lg(\mathrm{e})} \tag{2.7}$$

where k_{B} is the Boltzmann constant, T the temperature, K the elastic constant, λ the wavelength and n_{o} and n_{e} are the ordinary and extra ordinary refractive indices of the LC, respectively. As the order of $n^{\imath}$ is about 10^{-5} to 10^{-4}, $n^{\imath}$ is small compared to the real part of the refractive index. The imaginary part of the dielectric constant $\operatorname{Im}\epsilon$ is determined by

$$\operatorname{Im}\epsilon = 2n^{\mathrm{r}}n^{\imath}, \tag{2.8}$$

where n^{r} is real part of the refractive index.

2.1.4. The Frank-Oseen free energy

When we introduced the director $\boldsymbol{n}$ in Eq. (2.1), we included that $\boldsymbol{n}$ may vary with position $\boldsymbol{r}$. The nematic phase in the absence of external fields and far away from any boundary favors a uniform orientation. This means that the lowest energy is assumed when the director is constant over the whole volume. However, this may change in the presence of external fields or specific boundary condition. A description involving the free energy densities for elasticity, external fields and boundaries has been developed by Oseen [47] and Frank [48]

$$F = \int_{\Omega}(f_{\mathrm{e}} + f_{\mathrm{d}}) + \int_{\partial\Omega} f_{\mathrm{s}}. \tag{2.9}$$

Here, F is the free energy which consist of three energy densities in a spatial domain $\Omega \in \mathbb{R}^3$ with the boundary $\partial\Omega$. f_{e} describes the free energy density for elastic deformations, f_{d} the dielectric contributions and f_{s} the influences of the boundary. In the following, we discuss these three terms individually. We assume that the order parameter S is constant over the domain Ω. This is an approximation but it holds as long as there are no defects present.

2.1.4.1. Elastic free energy

For the elastic free energy, all derivatives of second order are taken into account which fulfill the symmetries provided by the nematic phase and the local coordinate system[48]. Then the elastic free energy density can be shown to be [49, §2.2]

$$\begin{aligned} f_\mathrm{e} = &+ \frac{1}{2}K_{11}(\nabla \cdot \boldsymbol{n})^2 + \frac{1}{2}K_{22}(\boldsymbol{n} \cdot \nabla \times \boldsymbol{n})^2 + \frac{1}{2}K_{33}(\boldsymbol{n} \times \nabla \times \boldsymbol{n})^2 \\ &+ \frac{1}{2}(K_{24} - K_{22})\nabla \cdot [\boldsymbol{n} \cdot (\nabla \cdot \boldsymbol{n}) + \boldsymbol{n} \times (\nabla \times \boldsymbol{n})]. \end{aligned} \tag{2.10}$$

The different terms can be identified as different types of deformation: splay, twist and bent. Each of these has a specific elastic constant K_{11},K_{22} and K_{33}, which are all positive. These types are displayed in Fig. 2.6. The last term in Eq. (2.10) involving the elastic constants K_{22} and K_{24} is called the saddle splay term. It can be shown by use of the divergence theorem [50, §3.8] that it actually contributes to the surface free energy density, thus does not influence the bulk free energy.

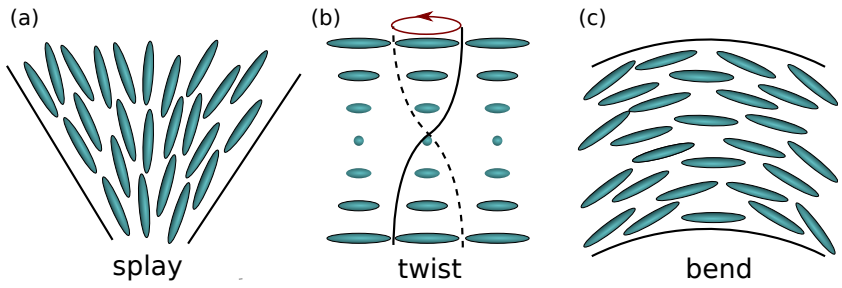

Figure 2.6. Schematic representation of the different types of deformation a nematic phase can exhibit: (a) splay, (b) twist and (c) bend.

The elastic deformation for twist, bend and splay all involve the square of the derivative (divergence or curl), which makes them positive in any case. Thus any kind of distortion will cause the free energy density to increase. This is in agreement with the above statement, that the nematic phase favors a homogeneous director field in the absence of any external fields or boundary conditions.

Under the assumption that all elastic constants are equal, i. e. $K = K_{11} = K_{22} = K_{33}$, Eq. (2.10) simplifies considerably to

$$f_\mathrm{e}^\mathrm{oca} = \frac{1}{2}K\left((\nabla \cdot \boldsymbol{n})^2 + (\nabla \times \boldsymbol{n})^2\right). \tag{2.11}$$

This is the free energy density in the one constant approximation (OCA).

2.1.4.2. Dielectric energy

In the presence of an electric field $\boldsymbol{E}$ the contribution to the free energy density is given by classical electromagnetic theory [51],

$$f_\mathrm{d} = -\frac{1}{2}\boldsymbol{D} \cdot \boldsymbol{E}, \tag{2.12}$$

where $\boldsymbol{D}$ is the displacement field. If we consider the liquid crystal to be an optically linear medium, $\boldsymbol{D}$ can be written as $D = \bar{\bar{\epsilon}}\boldsymbol{E}$. The permittivity $\bar{\bar{\epsilon}}$ is a second rank tensor [46] given by

$$\bar{\bar{\epsilon}} = \epsilon_\perp \cdot I_3 + (\epsilon_\parallel - \epsilon_\perp) \cdot (\boldsymbol{n} \otimes \boldsymbol{n}), \tag{2.13}$$

where $\epsilon_\perp$ and $\epsilon_\parallel$ are the permittivities perpendicular and parallel to the director, respectively. I_3 is the identity matrix and $\boldsymbol{n} \otimes \boldsymbol{n}$ the tensor product. The difference between the parallel and perpendicular permittivites we already defined as the dielectric anisotropy

$$\Delta\epsilon = \epsilon_\parallel - \epsilon_\perp. \tag{Eq. (2.4)}$$

The dielectric anisotropy can be positive or negative depending on the type of liquid crystal which has important practical implications. We will discuss the dielectric properties of LCs in more detail in Sec. 2.2.1

With the permittivity tensor defined in Eq. (2.13) we can write the dielectric free energy density as

$$\begin{aligned} f_\mathrm{d} &= -\frac{1}{2}\left(\bar{\bar{\epsilon}}\boldsymbol{E}\right) \cdot \boldsymbol{E} \\ &\overset{(2.13)}{=} -\frac{1}{2}\epsilon_0 \left[\left(\epsilon_\perp \cdot I_3 + \Delta\epsilon \cdot (\boldsymbol{n} \otimes \boldsymbol{n})\right)\boldsymbol{E}\right]\boldsymbol{E} \\ &= -\frac{1}{2}\epsilon_0 \left(\epsilon_\perp \boldsymbol{E}^2 + \Delta\epsilon(\boldsymbol{E} \cdot \boldsymbol{n})^2\right). \end{aligned} \tag{2.14}$$

From this equation it is clear that the lowest energy is reached if $\boldsymbol{E}$ and $\boldsymbol{n}$ are parallel in the case $\Delta\epsilon > 0$ or perpendicular in the case $\Delta\epsilon < 0$. This is the key principle how liquid crystal displays (LCDs) are operated by the application of electric fields. We will describe one possible realization of a single LC cell in Sec. 2.3 for the case $\Delta\epsilon > 0$.

2.1.4.3. Surface energy

Typically, liquid crystals are confined to some kind of geometry. This leads to interactions at the shared interfaces of the liquid crystal and the confining material. These interaction can have strong influence on the resulting director field. Much effort has been invested to tailor the surface interactions in order to facilitate a specific LC orientation.

In the context of this work we will discuss two types of alignment: planar and homeotropic. The different kinds of alignment are typically facilitated modifying the surface of a glass substrate chemically and/or topologically. Here, we describe some principles about the alignment types. We will consider only the interaction of the LC with a single planar substrate. Different substrates with different alignment types can then be combined to form cells with of a specific alignment type.

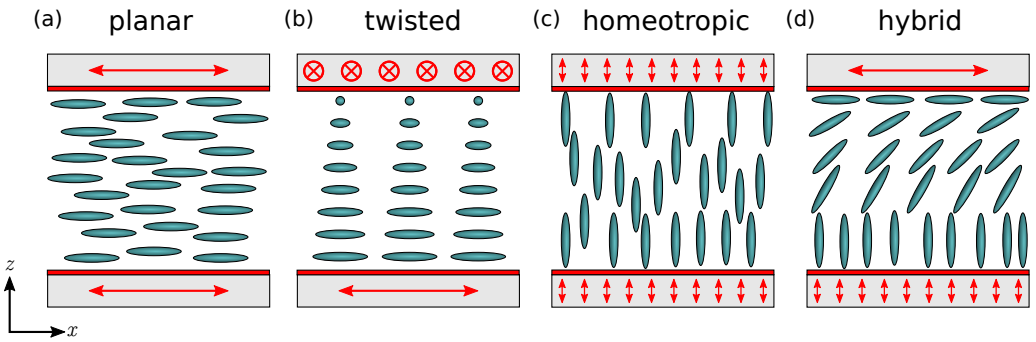

Figure 2.7. Liquid crystal cells composed of substrates with alignments layers (red), the direction of which is indicated by the red arrows: (a) Parallel planar, (b) twisted, (c) homeotropic and (d) hybrid configuration.

Some possible configurations are shown in Fig. 2.7. All these types can be used for LCDs, but have to be run by a different driving scheme. Figure 2.7 (a) shows the most simple cell with a parallel planar alignment. We will use this cell to describe the electrooptic switching in Sec. 2.3. In Sec. 2.4 we will discuss how these alignment layers are prepared in practice. And in Sec. 2.5 we will see how the alignment layer effect the director field in a circular capillary.

Planar alignment

The planar alignment refers to the case where the molecule long axis is parallel to the surface as shown in Fig. 2.8 (a, b). For homogeneous planar anchoring Fig. 2.8 (a), all molecules have a preferred direction. In terms of the coordinate system in Fig. 2.8 (c) this means that the polar angle θ is zero, $\theta = 0$, and the azimuthal angle ϕ has some fixed angle ϕ_0.

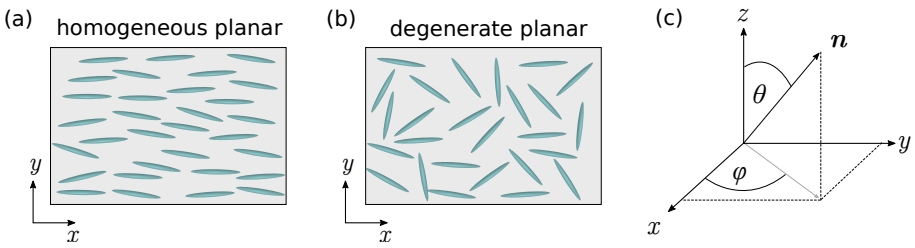

Figure 2.8. Planar alignment of a liquid crystal on the surface. (a) Homogeneous orientation of the molecules along a specific axis in the plane. (b) The degenerate planar configuration where the LC is confined to a plane but does no have a fixed azimuthal angle ϕ. (c) Coordinate system with the polar angle θ and the azimuthal angle ϕ.

The degenerate planar configuration [Fig. 2.8 (b)] forces the molecules to be aligned parallel to the substrate but there is no preferred direction within the plane. This means that θ is zero and the azimuthal angle ϕ is arbitrary for each LC molecule.

Homeotropic alignment

While under planar anchoring the LC molecules are parallel to the surface ($\theta = \pi/2$), under homeotropic anchoring [Fig. 2.9 (a)] the molecules are perpendicular to the surface ($\theta = 0$). The azimuthal angle ϕ then plays no role. A related anchoring condition is the tilted configuration, where $0 < \theta < \pi$ and the ϕ angle plays a role again.

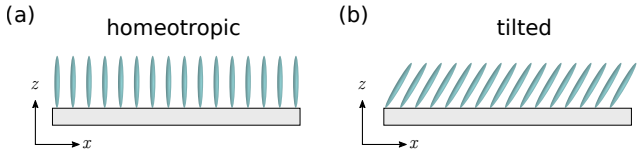

Figure 2.9. Homeotropic alignment of a LC molecules on the surface. (a) Perpendicular to the surface i. e. with $\theta = \pi$ and (b) titled with a polar angle $\theta < \pi$.

Rapini Papula potentials

The anchoring conditions we discussed above all describe a fixed configuration on the surface. A more realistic model is provided by Rapini and Papoular [52]. This model allows for deviations from the prescribed angles at the cost of increasing energy

$$f_s^\chi = \frac{1}{2} W_\chi \sin^2(\chi - \chi_0), \quad \chi = \{\varphi, \theta\}, \quad \chi_0 = \{\varphi_0, \theta_0\}, \tag{2.15}$$

where W_χ describes the anchoring energies for the polar and azimuthal direction.

Within this model, the planar anchoring type is characterized by an infinite polar anchoring energy, i. e. $W_\theta \to \infty$. For the degenerate planar case, the azimuthal anchoring energy is zeros ($W_\phi = 0$). For the homogeneous planar case it is infinite ($W_\phi \to \infty$).

The homeotropic anchoring is characterized by $W_\theta \to \infty$ and $\theta = 0$. If the homeotropic anchoring energy is finite, the actual orientation directly on the surface is influenced by the elastic and the dielectric energies and might in reality look more like the tilted configuration in Fig. 2.9 in order to decrease the total free energy.

2.1.5. Euler Lagrange equations

We have completed the discussion of the different energy densities of the total free energy density (Eq. (2.9)). This means we are able to calculate the energy of a specific director field. In reality, what we are usually looking for is the equilibrium configuration of the director field under the given constraints of the boundary and the applied electric field. This equilibrium configuration corresponds to the minimizer of the free energy Eq. (2.9) and can thus be found by the Euler Lagrange equation.

The Euler Lagrange equation is a set of partial differential equations (PDEs), the solutions of which (for given boundary conditions) will give the equilibrium

director field. In practice, finding this director field can be a very challenging task as the equations are highly non-linear. In order to establish a qualitative picture, it is sufficient to use the free energy density within the one constant approximation Eq. (2.11) and assume Dirichlet boundary conditions. Dirichlet boundary conditions are given by prescribing a fixed director field on the boundaries as we have done in the description of the planar and homeotropic anchoring. Then the PDE to solve takes the rather simple form

$$\begin{cases} \Delta\epsilon(\boldsymbol{n}\cdot\boldsymbol{E})\boldsymbol{E} - \frac{1}{2}K\Delta\boldsymbol{n} = \boldsymbol{0}, & \text{for } \boldsymbol{r}\in\Omega, \\ \boldsymbol{n} = \boldsymbol{\nu}, & \text{for } \boldsymbol{r}\in\partial\Omega, \end{cases} \tag{2.16}$$

where Δ is the Laplace operator, $\Delta\epsilon$ the dielectric anisotropy, K the elastic constant and $\boldsymbol{\nu}$ a function describing a specific director field on the surface.

2.2. Dielectric and optical properties of liquid crystals

In Sec. 2.1.4.2 we introduced the second rank tensor which describes the dielectric properties of liquid crystals. Here we want to discuss the dielectric properties in more details. In Fig. 2.10 (a) we show the liquid crystal molecule PCH5. Due to the anisometric shape, there are two polarizabilities, $\alpha_{\parallel}$ and $\alpha_{\perp}$, parallel and perpendicular to the molecular axis, respectively. Further, the molecule carries a permanent dipole moment μ due to the polar cyano headgroup.

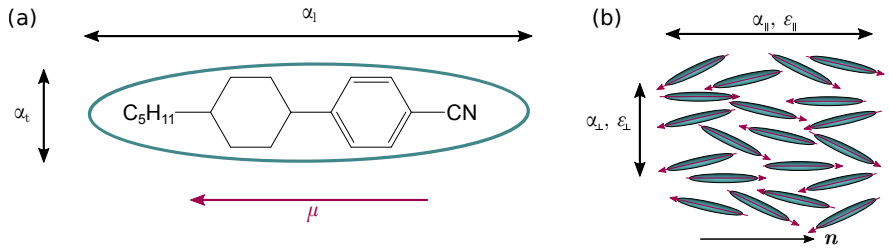

Figure 2.10. (a) Liquid crystal molecule with molecular polarizabilities , α_l and α_t, and the dipole moment μ. (b) Ensemble of molecules in the nematic phase with macroscopic polarizabilities, $\alpha_{\parallel}$ and $\alpha_{\perp}$, permittivites $\epsilon_{\perp}$ and $\epsilon_{\parallel}$ and the director $\boldsymbol{n}$. The dipole moments are marked with a red arrow.

If we look at an ensemble of molecules in the nematic phase [Fig. 2.10 (a)], the polarizablities $\alpha_{\parallel}$ and $\alpha_{\perp}$ are the quantities describing the macroscopic behavior. These deviate from the molecular polarizabilities due to the fluctuation in orientation (cf. Sec. 2.1.1). The macroscopic dipole moment of the ensemble averages out to zero as the dipoles cancel each other. But in the presence of an external electric field the dipoles orient parallel to the field similar to the induced dipoles.

Both, the polarizabities and the dipoles, can contribute to the macroscopic dielectric permittivities $\epsilon_{\parallel}$ and $\epsilon_{\perp}$. As the behavior of the permanent dipole contribution is strongly frequency dependent, we divide the remaining discussion in two parts:

First, we describe the behavior for electric fields which oscillate at frequencies in the kHz to the MHz range. These are of particular interest for addressing the liquid crystal in LC cells. Secondly, we will turn to the optical regime where the frequency of the electric field is much higher (10^{14} Hz to 10^{15} Hz).

2.2.1. Dielectric properties

2.2.1.1. Positive dielectric anisotropy

As already mentioned, the liquid crystal molecules can be oriented due to an external electric field. Due to their anisometric shape, the reorientation of dipoles can be strongly frequency dependent.

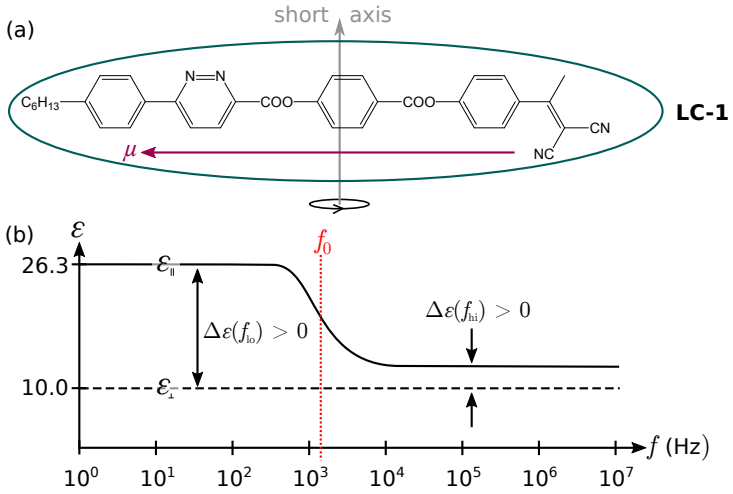

Figure 2.11. (a) Liquid crystal molecule LC-1 with positive dielectric anisotropy [53] due to strong dipole moment μ along the molecular axis. (b) Dielectric frequency spectrum with perpendicular and parallel dielectric constants $\epsilon_\perp$ and $\epsilon_\parallel$. f_0 marks the critical frequency where rotation about the short axis becomes hindered.

In Fig. 2.11 (a) we show a liquid crystal molecule (LC-1) with a strongly anisometric shape and a permanent dipole moment along the long axis of the molecule. Under the application of an electric field parallel to the molecular axis, the LC-1 molecule will reorient its dipole along the oscillating electric field. This strongly contributes to the dielectric constant. The dielectric frequency spectrum of this compound is shown in Fig. 2.11 (b). At around the critical frequency $f_0 \approx 1.4\,\text{kHz}$, the parallel dielectric constant $\epsilon_\parallel$ drops rapidly. Above this frequency the rotation around the short axis becomes hindered and the permanent dipole can no longer contribute to the permittivity.

2.2.1.2. Negative dielectric anisotropy

A second LC molecule (LC-2) is shown in Fig. 2.12 (a). Here, the molecule has a strong dipole perpendicular to the molecular long axis, meaning that the molecule

will orient perpendicular to an external electric field. Thus, for this molecule the dielectric anisotropy is negative ($\Delta\epsilon < 0$). LC-2 does not show a critical frequency in the dielectric spectrum [Fig. 2.12 (b)] in contrast to molecule LC-1 in Fig. 2.11 (a). This is a consequence of the rotation around the long axis of the molecule LC-2, which is much faster than about the short axis. Eventually, this rotation will also become hindered but at much higher frequencies ($\sim 10^9$ Hz).

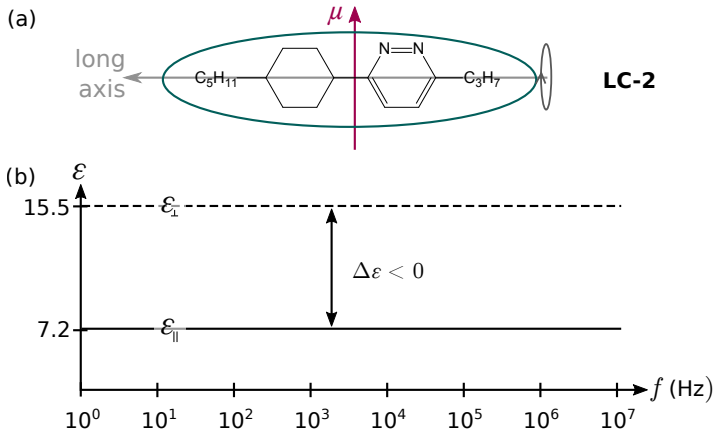

Figure 2.12. (a) Liquid crystal molecule LC-2 with negative dielectric anisotropy [53] due to strong dipole moment μ perpendicular to the molecular axis. (b) Dielectric frequency spectrum with perpendicular and parallel dielectric constants $\epsilon_\perp$ and $\epsilon_\parallel$.

2.2.1.3. Dual frequency behavior

Liquid crystal molecules can be deliberately designed to exhibit a dipole moment which is oblique to the molecular axis [54–56]. An example of such a molecule is shown in Fig. 2.13 [55]. The dipole moment is skew to the molecular axis due to the polar chlorine attached to the phenyl ring.

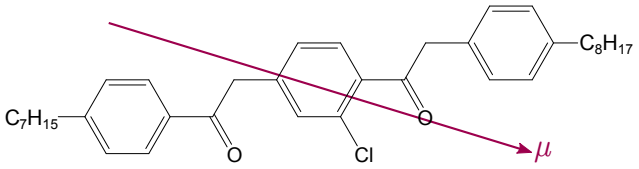

Figure 2.13. Liquid crystal molecule which has a dipole moment μ skew to the molecular axis. Due to its structure it shows dual frequency behavior. [55]

At low frequencies, the molecular reorientation with the complete molecular dipole is fast enough to follow the electric field. At high frequencies, the reorientation around the short axis becomes hindered [cf. Fig. 2.11 (a)] and only the rotation around the long axis persists. Consequently, at low frequencies the molecules align parallel to the electric field and perpendicular to it at high frequencies (Fig. 2.14). Liquid crystal components with exhibit this behavior are called to be dual frequency addressable.

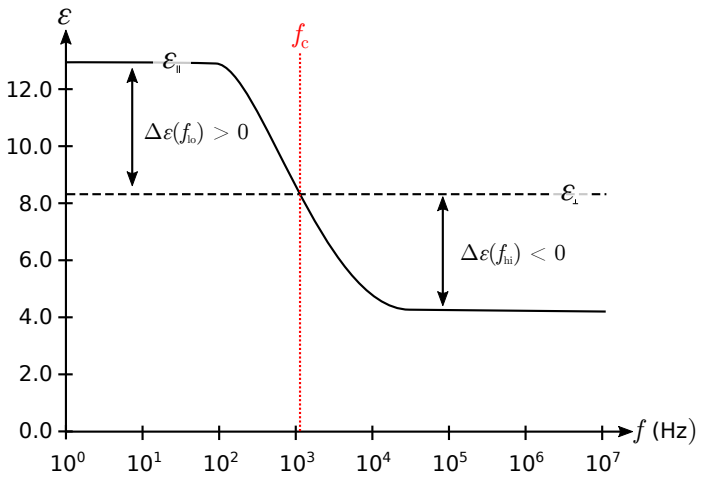

Figure 2.14. Perimittivity spectrum for liquid crystal (LC) molecule with a skew dipole moment. Below the critical frequency f_c, the LC has a positive dielectric anisotropy ($\Delta\epsilon > 0$). For $f > f_c$, $\Delta\epsilon$ becomes negative.

The dual frequency behavior has some advantages over the purely positive or negative dielectric materials. In liquid crystal cells, the response to the external field can be tuned by changing the frequency. At low frequencies, the LC will orient parallel to the electric field, at high frequencies the molecules will be perpendicular. This can be used to enhance the switching speed in liquid crystal displays [57]. Usually, the switching-on process is initiated at low frequencies with positive $\Delta\epsilon$, thus the molecules align parallel to the external field. The switching-on speed depends on the electric field strength and can be enhanced with higher fields. In contrast, the switching-off process usually does not depend on the electric field strength. Here, the application of a high frequency field will force the director field to relax faster into the initial state.

But the dual frequency behavior also brings certain disadvantages. As it usually consist of a mixture of materials with positive and negative dielectric anisotropy, the absolute value of $\Delta\epsilon$ is usually smaller than in the pristine components. This weakens the response to electric electric fields and leads to higher operation voltages. From a practical point of view, dual frequency components will always require to be able to apply two different frequencies below and above the cross-over frequency which leads to more complicated experimental realization.

2.2.2. Optical properties

Liquid crystals are most commonly used in displays as a light valve thus the interaction with light is an important topic in LC science. As light can be described as an electromagnetic wave, there are many similarities between the interaction of a LC with light and the interactions with electric fields. One important difference is the considered frequency range. Before, we discussed the electric fields oscillating at 10^3 Hz to 10^7 Hz while light is vibrating at frequencies from 10^{14} Hz to 10^{15} Hz.

In the latter frequency region, any rotation of the molecules cannot follow the electric field. Thus only the polarizability of the electrons contribute to the dielectric function. As we mentioned earlier, the refractive index n and the dielectric function are related by $\epsilon = n^2$.

We already saw that due to the anisometric shape of the liquid crystal molecules and the consequent appearance of a nematic phase, that there exist two permittivities: parallel and perpendicular to the director. This is also true for the refractive indices. They are called the ordinary refractive index n_o and the extraordinary refractive index n_e. The ordinary index n_o is related to $\epsilon_\perp$ and n_e to $\epsilon_\parallel$ via Eq. (2.5). An average refractive index $\bar{n}$ of the ordinary and the extraordinary index is defined by

$$\bar{n} = \left(\frac{2}{3} {n_\mathrm{o}}^2 + \frac{1}{3} {n_\mathrm{e}}^2 \right)^{\frac{1}{2}} . \tag{2.17}$$

Figure 2.15 shows the three refractive indices n_o, n_e, and $\bar{n}$ in the nematic phase of the molecule PCH5 (cf. inset for the molecular structure) as a function of temperature. We observe that at low temperature n_o and n_e are far apart and become closer with increasing temperature. This is directly connected to the order parameter S we discussed in Sec. 2.1.1. With the increasing temperature the medium becomes more disordered (S decreases) and the indices become more alike. This is until the phase transition from nematic to isotropic occurs, which is characterized by a discontinuous disappearance of the ordinary and extraordinary refractive index.

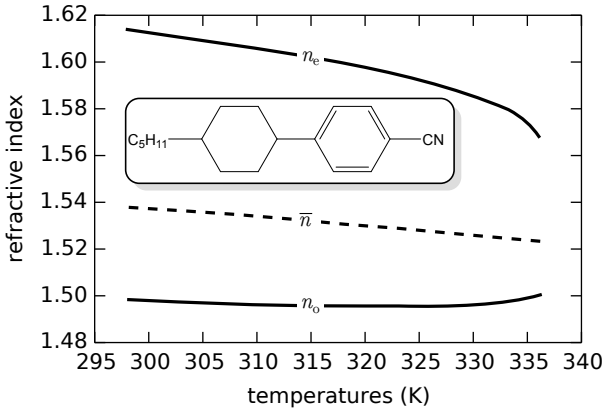

Figure 2.15. Refractive indices of liquid crystal molecule PCH5 (inset) as a function of temperature. Ordinary index n_o, extraordinary refractive index n_e and average index $\bar{n}$. The phase transition from nematic to isotropic is around 337 K.

We also observe that the average index decreases in an approximately linear manner. This is due to thermal expansion of the medium which decreases the density and thus the refractive index. Beyond the phase transition temperature, only the isotropic index can be measured. The isotropic refractive index can be approximated by extrapolating the average refractive index $\bar{n}$ beyond the phase transition temperature. There are some difference as the loss of the nematic order is accompanied

by a small decrease in density and thus in refractive index.

Analog to the dielectric anisotropy we earlier defined the optical anisotropy or birefringence

$$\Delta n = n_\mathrm{e} - n_\mathrm{o}. \tag{2.6}$$

The birefringence plays a major role in many applications of liquid crystals, especially for liquid crystal displays (LCDs). The basic principle of one type of LCD will be discussed next.

2.3. Liquid crystal displays: Basic principle

2.3.1. Light transmission through birefringent media

The birefringence of a liquid crystal cell is the key feature of liquid crystal displays as it can be tuned electrically. The basic principle of how a birefringent medium influences the light transmission is shown in Fig. 2.16 (a).

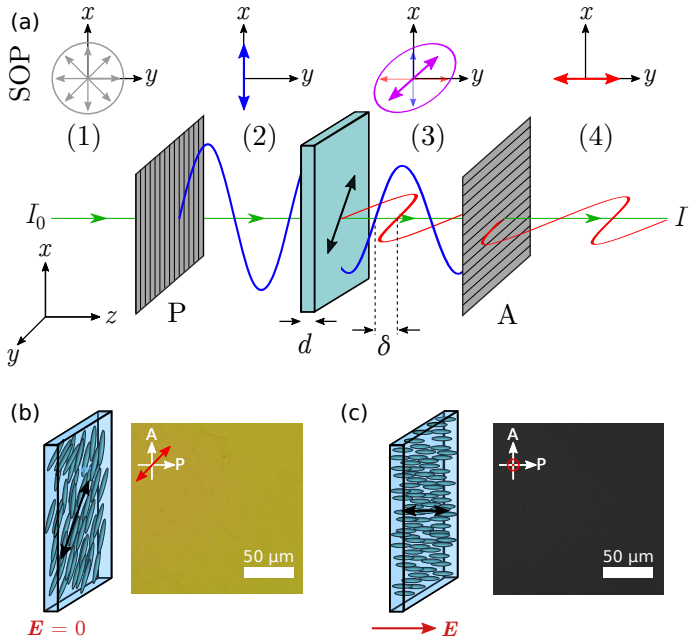

Figure 2.16. (a) Basic principle of a liquid crystal cell. The arrows indicate the state of polarization (SOP). (1) Unpolarized light passes through a polarizer (P) and is polarized along the x direction (2). After passing through the liquid crystal cell in which the director is oriented in a non-zero angle with regards to polarizer and analyzer, the light light is elliptically polarized (3). Through the analyzer only the y-polarized part is transmitted (4). (b) Director field for a planar aligned cell (left) in the absence of a voltage. The LC cell is birefringent and light is transmitted between crossed polarizers (right). (c) Director field under the application of a voltage perpendicular to the cell. Here, the optical axis is parallel to the propagation of light and no light is transmitted (right).

Light of arbitrary polarization is polarized along the x-axis by the polarizer P and passes through a parallel planar oriented liquid crystal cell [cf. Fig. 2.7 (a)] of thickness d. If the orientation of the LC director is 45° with respect to the polarizer,

the polarization component parallel to the director $\boldsymbol{n}$ will be phase shifted by δ with respect to the component perpendicular to $\boldsymbol{n}$. The phase shift is determined by

$$\delta = \frac{2\pi}{\lambda} d\Delta n. \tag{2.18}$$

The state of polarization after the LC cell will therefore in general be elliptically; the part polarized along the y-axis will pass the analyzer A leading to a bright state [Fig. 2.16 (b)]. The intensity transmitted through the system depends on the phase shift δ and for crossed polarizers can be shown to be [44]

$$I = \frac{1}{2} \sin^2\left(\frac{\delta}{2}\right) I_0. \tag{2.19}$$

The director $\boldsymbol{n}$ can be reoriented by an external electric field, which is parallel to the cell normal [Fig. 2.16 (c)]. Consequently, the LC molecules are also oriented along the cell normal (z-direction). In that case the light travels along the optical axis and no birefringence acts on it. Therefore, the light after the LC cell is still linear polarized along the x-axis and will not pass the analyzer. This corresponds to the dark state and resembles a homeotropically aligned cell [cf. Fig. 2.7 (c)].

The reorientation of the LC molecules due to the electric field from the parallel planar configuration [bright state, Fig. 2.16 (b)] to a homeotropically aligned cell [dark state, Fig. 2.16 (c)] is called a Fréedericks transition [58, 59].

2.3.2. The Fréedericksz transition

The director field in Fig. 2.16 (c) shows a very simplified picture of deformation of the director field under an applied electric field. Figure 2.17 shows a more realistic representation for (a) the field-off state and (b) the director field under an electric field. In this representation, strong homogeneous planar anchoring is assumed.

The strong anchoring leads to a homogeneous planar orientation of the LC molecules for $\boldsymbol{E} = 0$ [Fig. 2.17 (b)]. In the field-on state [Fig. 2.17 (c)], the anchoring on the surface still is prescribed by the boundary conditions. But inside the bulk the liquid crystal molecules orient along the external field. The transition from one state to the other does not occur continuous with the applied external field but there exists a critical electric field $\boldsymbol{E}_c$ below which no change in director configuration is observed. For the Fréedericksz transition, the critical electric field E_c is given by [60, Chap. 5]

$$E_c = \frac{\pi}{d}\sqrt{\frac{K_{11}}{\epsilon_0 \Delta\epsilon}}, \tag{2.20}$$

where d is the cell thickes, K_{11} the splay eleastic constant, ϵ_0 the vacuum permittivity and $\Delta\epsilon$ the dielectric anisotropy. The critical field strength usually is of the order of $\sim 1\,\mathrm{V\,\mu m^{-1}}$.

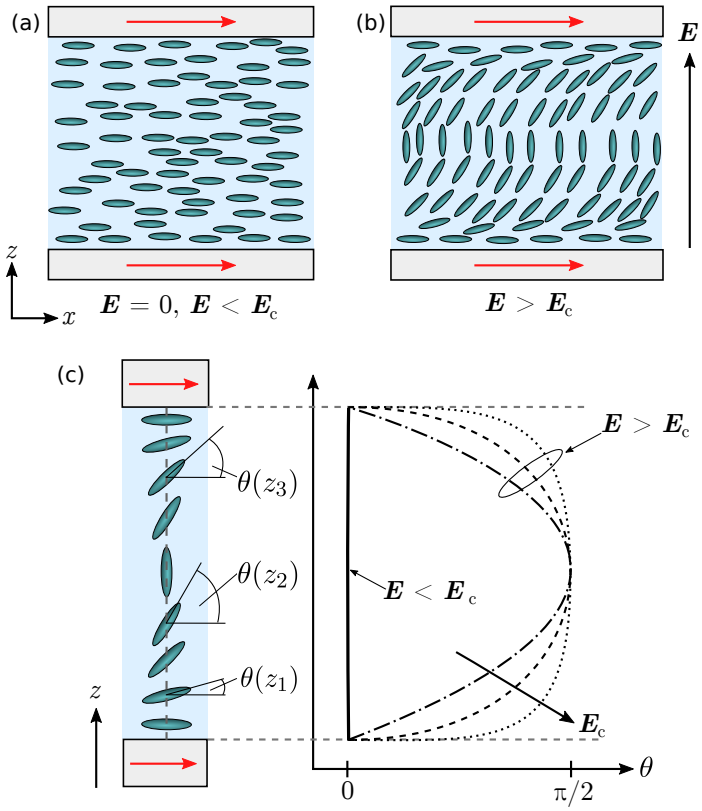

Figure 2.17. Liquid crystal cell with a homogeneous planar aligned liquid crystal (indicated by the red arrows): (a) without electric field ($\boldsymbol{E} = 0$) or with an electric field lower than the critical field $|\boldsymbol{E}| < |\boldsymbol{E}_c|$ and (b) with an electric field $\boldsymbol{E}$ exceeding $\boldsymbol{E}_c$ perpendicular to the cell surface. (c) z-dependent angle between the liquid crystal director and the direction of the planar alignment for different electric field strengths.

Figure 2.17 (c) shows the director field in a LC cell calculated by numerically solving Eq. (2.16). If we assume that the director is only reoriented within the xz-plane, the director field is fully determined by the angle θ. For $E < E_c$, the director remains in his initial condition. Even though the molecules experience some torque from the presence of the electric field, the elastic deformation would cost to much energy.

Above the threshold electric field E_c, the angle θ in the middle of the cell jumps from 0 to $\pi/2$. Further increase of the electric field increases the deformation of the director field close to the surfaces due to the higher torque.

For liquid crystal display, the switching times are of great interest. For the Fréedericksz transition the formulas for the switching off time τ_{off} and the switching on time τ_{on} read

$$\tau_{\text{off}} = \frac{\gamma_1}{K_{11}} \left(\frac{d}{\pi}\right)^2 \tag{2.21}$$

$$\tau_{\text{on}} = \frac{\gamma_1}{K_{11}} \left(\frac{d}{\pi}\right)^2 \left[\left(\frac{E}{E_c}\right)^2 - 1\right]^{-1} = \tau_{\text{off}} \left[\left(\frac{E}{E_c}\right)^2 - 1\right]^{-1}, \tag{2.22}$$

where γ_1 is the rotational viscosity of the liquid crystal. From this equations we see that both switching times increase quadratic with the cell gap.

2.4. Alignment techniques for liquid crystals

In Sec. 2.1.4.3 we introduced the different types of anchoring a liquid crystal can exhibit on a surface. Here, we discuss how the different anchoring conditions are facilitated by modifying the surfaces. An emphasize is put on techniques which do not require direct access to the surface as for this work the liquid crystal will be confined to micrometer-sized capillaries which prohibits direct contact.

2.4.1. Degenerate planar anchoring

A degenerate planar configuration [cf. Fig. 2.8 (a)] can be achieved in different ways. Most common are the chemical solution deposition of polyvinyl alcohol (PVA, [61]), polyimide (PI, [62]) or poly-methyl methacrylate (PMMA, [63]) films. The liquid crystal molecules typically favor an orientation parallel to the polymer chains. During the deposition step, the polymeric chains orient parallel to the surface but with no specific azimuthal angle. This random planar orientation is transferred to the liquid crystal.

Besides the long polymeric chains, smaller molecules like (3-glycidoxypropyl)tri"-methoxy"-silane [glymo, Fig. 2.18] can also lead to degenerate planar anchoring.

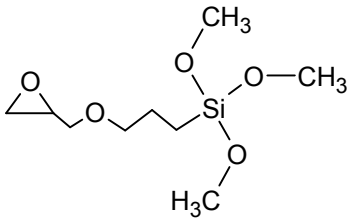

Figure 2.18. Molecular structure of glymo.

Typically, surfaces with degenerate planar anchoring can be turned into homogeneous planar anchoring by rubbing the surface in a specific direction. This leads to an orientation of the polymer molecules along the rubbing direction. Rubbing is the preferred method in industry as it is an easy method and can be applied to large scales.

2.4.2. Homogeneous planar anchoring

A contact-free method to align the polymer chains and thus the liquid crystal molecules in a homogeneous fashion is based on linearly polarized photopolymerization, e. g. polyvinylmethoxy-cinnamate (Fig. 2.19) [64, 65]. This polymer has a polyvinyl back bone to which cinnamate groups are attached [Fig. 2.19 (a)]. Two cinnamate

groups can undergo a 2+2-cyclo-addition reaction which crosslinks two polymer chains. This reaction is induced by using linearly polarized UV light thus only cinnamate groups with their long axis parallel to the polarization of light are crosslinked. As the cinnamate groups are perpendicular to the polymer chain [Fig. 2.19 (b)], the latter will align perpendicular to the polarization of light. This will lead to a homogeneous film of parallel aligned polyvinyl chains which form the alignment layer.

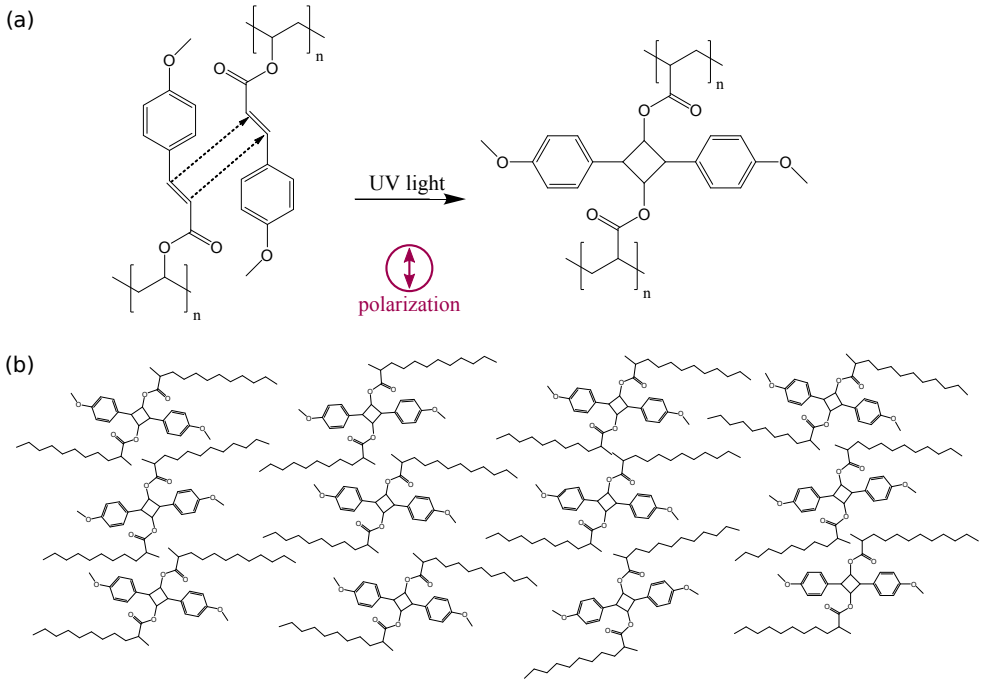

Figure 2.19. (a) 2+2-cycloaddition is initiated via UV light if the polymer backbone is perpendicular to the polarization of the light. (b) Ensemble of cinnamate dimers after reaction. The polymer backbones are oriented parallel which will induce a parallel orientation of the liquid crystal molecules.

The photo-alignment technique provides some advantages over the conventional rubbing techniques. As there is no contact necessary it is applicable to curved or confined surfaces. And it does not contaminate the substrate with ions or dust. Therefore, this technique has already found its application in industry. For example Apple is using it in the fabrication of the iMac [66]. A drawback, however, is that the azimuthal anchoring strength is lower compared to surfaces prepared via the rubbing technique [67].

2.4.3. Homeotropic anchoring

A standard method to obtain homeotropic anchoring is the deposition of amphiphilic molecules on a substrate [68], which form a self assembled monolayer. Commonly employed chemical compounds are lecithin, octadecyltrichlorosilane [OTS, Fig. 2.20 (a)] or cetyl trimethylammonium bromide[Fig. 2.20 (b)] [69]. The polar

head group will anchor on the silica surface. If the density of amphiphilic molecules is high enough, the apolar tail group will be perpendicular to the surface. The tail group then leads to perpendicular anchoring of the LC [Fig. 2.20 (c)]. In the case of OTS, the silane will bind covalently on the silica surface [Fig. 2.20 (d)].

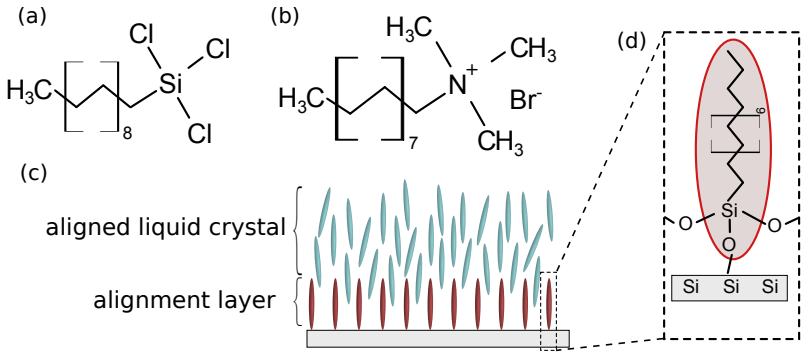

Figure 2.20. Homeotropic alignment agents: (a) octadecyltrichlorosilane (OTS) and (b) hexadecyltrimethylammonium bromide (CTAB). (c) Homeotropic alignment of the LC on the surface due to a monolayer of surfactant molecules. The polar head group of the surfactant anchors on the substrate, the non-polar tail group is perpendicular to the surface. (d) Anchoring of OTS on a silica surface.

2.5. Liquid crystals in circular capillaries

A last piece to close the discussion on the director field configurations and the corresponding energies concerns the geometry the LC is confined to. For the purpose of this work only circular geometries as can be found in capillaries are discussed. The investigated capillaries have an inner diameter of about a few micrometer.

The axial alignment of the liquid crystal, where all molecules are oriented parallel to the fiber axis as shown in Fig. 2.21 (a), can be achieved by degenerate planar or homogeneous planar alignment. In the latter case the preferred direction has to be along the z-axis [65]. The axial configuration has no elastic deformations, the corresponding elastic energy [Eq. (2.10)] is therefore zero.

Homeotropic anchoring leads to a different director configuration called *escaped radial* depicted in Fig. 2.21 (b,c). In the case of infinite polar anchoring strength ($W_\theta \to \infty$), which we discussed in Sec. 2.4.3, the molecules are perpendicular to the surface [Fig. 2.21 (c)]. Or equivalently, $\Omega(r = R) = \pi/2$, where r is the radial position and Ω the angle between the molecule axis and the z-axis, and R the inner radius. The director then changes continuously to $\Omega(r = 0) = 0$. The director field is rotational symmetric and can be described by $\Omega(r) = 2\tan^{-1}\left(\frac{r}{R}\right)$ within the one constant approximation [70].

If the anchoring energy is finite ($0 < W_\theta < \infty$), the molecules will be tilted on the surface and the anchoring angle $\alpha = \Omega(r = R)$ will be smaller than $\pi/2$. The angle

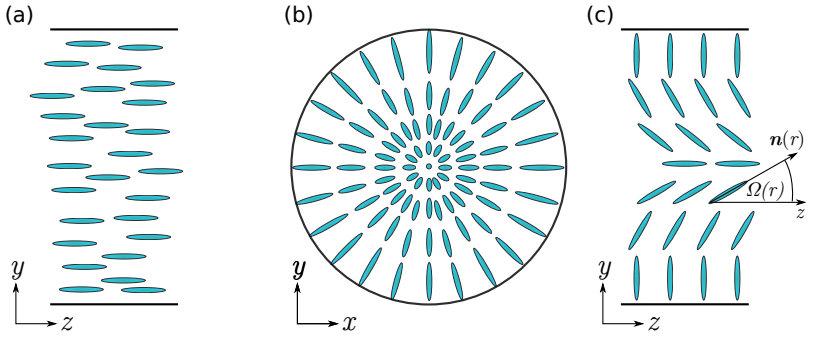

Figure 2.21. Liquid crystal configurations inside a microcapillary. (a) The parallel alignment leads to an axial director field along the capillary axis. (b) Homeotropic anchoring induces a escaped radial director field which is perpendicular on the inner surface and makes a continuous transition to a parallel alignment in the center in the capillary.

is given by [70]

$$\alpha = \Omega(R) = \cos^{-1}\left(\frac{k^{\frac{1}{2}}}{(\sigma^2 + k - 1)^{\frac{1}{2}}}\right), \tag{2.23}$$

where $k = \frac{K_{33}}{K_{11}}$ is the ratio of the bend and the splay elastic constant. A dimensionless surface parameter σ is introduced

$$\sigma = \frac{RW_\theta}{K_{11}} + \frac{K_{24}}{K_{11}} - 1, \tag{2.24}$$

where K_{24} is the saddle splay constant and R the capillary radius. The parameter σ is a handy way of characterizing the anchoring as it bundles multiple parameters. In Fig. 2.22 (a) the angle α is plotted against σ for different bend/splay ratios. Setting

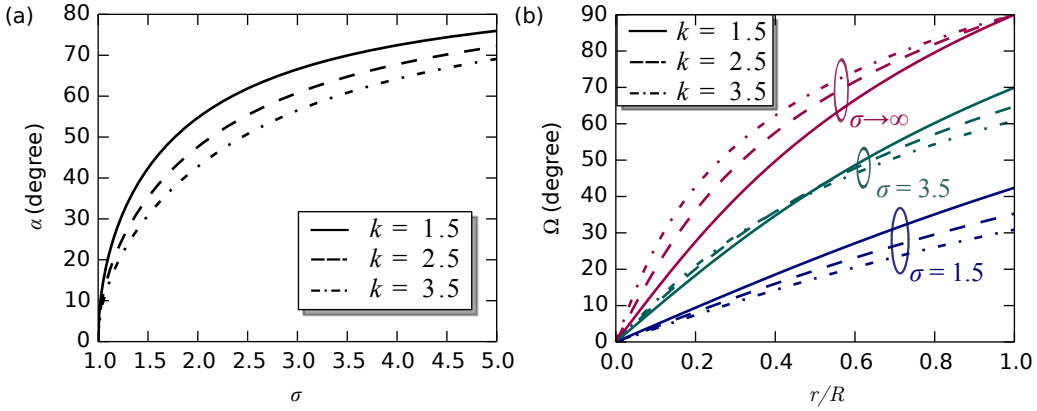

Figure 2.22. (a) Surface angle α as function of the ratio of the elastic constants bend and splay k. (b) Radial distribution of Ω for different k and σ.

$\sigma = 1$ leads to parallel surface anchoring ($\alpha = 0$), i. e. the planar configuration. For $\sigma \to \infty$ the director will be perpendicular to the surface ($\alpha = \pi/2$). The plot also reveals that the anchoring angle varies rapidly for small values of σ. The director field inside the capillary, i. e. for $0 < r < R$ can be found by minimizing Eq. (2.9) under the assumption of a radial symmetric director field which leads to implicit

equation [70]

$$\frac{r}{R} = \left(\frac{\sigma+1}{\sigma-1}\right)^{\frac{1}{2}} \left(\frac{\Delta - \beta' \cos\Omega(r)}{\Delta + \beta' \cos\Omega(r)}\right)^{\frac{1}{2}} \times \exp\left[\frac{\beta}{\beta'} \sin^{-1}(\beta \cos\alpha)\right] \exp\left[-\frac{\beta}{\beta'} \sin^{-1}[\beta \cos\Omega(r)]\right], \tag{2.25}$$

where $\Delta = \left[1 - \beta^2 \cos^2\Omega(r)\right]^{\frac{1}{2}}$, $\beta = |k-1|\, k^{-1}$ and $\beta' = k^{-1}$. This equation can be solved easily by numerical means. The results of different values of σ and k are plotted in Fig. 2.22 (b). An increase in σ, which effectively is an increase in anchoring strength, leads to a higher anchoring angle on the surface α. In the limit of $\sigma \to \infty$, α assumes 90°. For finite σ, α decreases as the surface anchoring energy has to compete with the elastic deformations which increase with α. The bend/splay ratio has only minor influence on the shape of the curve.

Chapter 3

Basic fiber optics

3.1. Introduction

In this section we will derive the wave equations from Maxwell's equations which are necessary to describe light propagation in optical waveguides. The results will then be applied to uniaxial step index fibers. On the basis of the latter, we present an approximate picture for the modes of a system of waveguides, which couple with each other due to their close vicinity. This picture will help us to understand the basics of photonic crystal fibers and photonic band gap fibers. At last we will turn to the disperion properties of the above mentioned waveguides, which will play a major role in the discussion of pulse propagation and the non-linear optical effect of four wave mixing.

3.2. Maxwell equations

We start out with Maxwell's equations in a perfect dielectric without sources, which gives us the following equations [71]

$$\nabla \cdot \boldsymbol{D} = 0 \tag{3.1}$$

$$\nabla \cdot \boldsymbol{B} = 0 \tag{3.2}$$

$$\nabla \times \boldsymbol{E} = -\imath\omega \boldsymbol{B} \tag{3.3}$$

$$\nabla \times \boldsymbol{H} = \imath\omega \boldsymbol{D}, \tag{3.4}$$

where $\boldsymbol{D}$ is the electric displacement field, $\boldsymbol{B}$ the magnetic induction, $\boldsymbol{E}$ the electric field, $\boldsymbol{H}$ the magnetic field and ω denotes the angular frequency. Here we assumed the harmonic time dependency $\boldsymbol{D}, \boldsymbol{B}, \boldsymbol{E}, \boldsymbol{H} \propto \mathrm{e}^{\imath\omega t}$. The magnetic induction and the magnetic field are related by

$$\boldsymbol{B} = \mu_0 \overline{\overline{\mu}}_r \boldsymbol{H}, \tag{3.5}$$

where μ_0 is the vacuum permeability and $\overline{\overline{\mu}}_r$ the material permeability tensor. The latter is assumed to be unity ($\overline{\overline{\mu}}_r = 1$) throughout this work as we are only working with non-magnetic materials. Analogous, there is a material relation for the electric field and the electric displacement

$$\boldsymbol{D} = \epsilon_0 \overline{\overline{\epsilon}}_r \boldsymbol{E}, \tag{3.6}$$

where ϵ_0 is the vacuum permittivity and $\overline{\overline{\epsilon}}_r$ is the second rank tensor of the material permittivity. The second rank tensor is necessary in this case in order to be able to describe liquid crystals [cf. Eq. (2.13) in Sec. 2.1.4.2].

In order to obtain the wave equation, we now apply the curl operator to Eq. (3.3) and use Equations (3.4), (3.5) and (3.6) to arrive at

$$\nabla \times (\nabla \times \boldsymbol{E}) = -\imath\omega \left(\nabla \times \boldsymbol{B}\right) = \omega^2 \mu_0 \epsilon_0 \overline{\overline{\epsilon}}_r \boldsymbol{E}, \tag{3.7}$$

where Δ is the Laplace operator. The left hand side can be further transformed by the vector identity $\nabla \times (\nabla \times \boldsymbol{E}) = \nabla(\nabla \cdot \boldsymbol{E}) - \Delta \boldsymbol{E}$ to yield

$$\nabla(\nabla \cdot \boldsymbol{E}) - \Delta \boldsymbol{E} = \omega^2 \mu_0 \epsilon_0 \overline{\overline{\epsilon}}_r \boldsymbol{E}. \tag{3.8}$$

By using the product rule on Eq. (3.1) with Eq. (3.6), we obtain

$$\begin{aligned} \nabla \cdot \boldsymbol{D} &= \nabla \cdot \left(\epsilon_0 \overline{\overline{\epsilon}}_r \boldsymbol{E}\right) \\ &= \epsilon_0 \left(\nabla^{\mathrm{T}} \overline{\overline{\epsilon}}_r\right) \boldsymbol{E} + \epsilon_0 \left(\overline{\overline{\epsilon}}_r^{\mathrm{T}} \nabla\right) \boldsymbol{E} \\ &= 0 \\ \Leftrightarrow \quad \nabla \cdot \boldsymbol{E} &= -\left(\nabla^{\mathrm{T}} \overline{\overline{\epsilon}}_r\right) \left(\overline{\overline{\epsilon}}_r^{\mathrm{T}}\right)^{-1} \boldsymbol{E}, \end{aligned} \tag{3.9}$$

where $\nabla^{\mathrm{T}} = \left(\frac{\partial}{\partial x}, \frac{\partial}{\partial y}, \frac{\partial}{\partial z}\right)$ is the transpose of ∇, $\overline{\overline{\epsilon}}_r^{\mathrm{T}}$ and $\left(\overline{\overline{\epsilon}}_r^{\mathrm{T}}\right)^{-1}$ are the transposed and the inverse of the transpose of $\overline{\overline{\epsilon}}_r$. The products $\nabla^{\mathrm{T}} \overline{\overline{\epsilon}}_r$ and $\overline{\overline{\epsilon}}_r^{\mathrm{T}} \nabla$ are interpreted as matrix products. The former is also known as the divergence of the tensor $\overline{\overline{\epsilon}}_r$, i. e. $\nabla^{\mathrm{T}} \overline{\overline{\epsilon}}_r = \nabla \cdot \overline{\overline{\epsilon}}_r$.

Then Eq. (3.8) will result in the inhomogeneous vector wave equation

$$\Delta \boldsymbol{E} + k^2 \overline{\overline{\epsilon}}_r \boldsymbol{E} = -\left(\nabla^{\mathrm{T}} \overline{\overline{\epsilon}}_r\right) \left(\overline{\overline{\epsilon}}_r^{\mathrm{T}}\right)^{-1} \boldsymbol{E}, \tag{3.10}$$

where $k = \omega/c$ is the free space wave number. In a homogeneous material the right hand side vanishes due to $\nabla \overline{\overline{\epsilon}}_r = 0$ which gives the homogeneous vector wave equation

$$\Delta \boldsymbol{E} + k^2 \overline{\overline{\epsilon}}_r \boldsymbol{E} = 0. \tag{3.11}$$

Analogous one can derive the a inhomogeneous and homogeneous vector wave equation relying on the magnetic field

$$\Delta \boldsymbol{H} + k^2 \bar{\bar{\epsilon}}_r \boldsymbol{H} = -\nabla \cdot \left\{ \left[\left(\nabla^{\mathrm{T}} \bar{\bar{\epsilon}}_r \right) \left(\bar{\bar{\epsilon}}_r^{\mathrm{T}} \right)^{-1} \right] \times (\nabla \times \boldsymbol{H}) \right\}, \tag{3.12}$$

$$\Delta \boldsymbol{H} + k^2 \bar{\bar{\epsilon}}_r \boldsymbol{H} = 0. \tag{3.13}$$

3.3. Uniaxial step index fiber

With the Eqs. (3.10) and (3.12) we are now able to find eigenmodes of a huge variety of waveguiding structures. For this work, we restrict ourselves to circular waveguides. But before we start deriving the modes of the waveguides, it is instructive to use the ray picture in order to get a basic understanding of how the guidance of light is facilitated.

3.3.1. The ray picture

Figure 3.1 (a) shows a schematic of a dielectric circular waveguide, i. e. an optical fiber. This fiber consists of a high refractive index core and a low refractive index cladding [Fig. 3.1 (b)] . Here, we assume that both, core and cladding, are isotropic. From the ray picture of light, we know that light is guided in this structure by total internal reflection [8, 72, 73]. Therefore, light coupled into the core propagates through this fiber by bouncing of the walls [Fig. 3.1 (c)].

This zigzag path through the fiber can be further characterized by the vacuum wave vector $\boldsymbol{k}$, the propagation vector $\boldsymbol{\beta}$ and the transverse propagation vector $\boldsymbol{\beta}^{\mathrm{t}}$. The vacuum wave number k is given by

$$k = |\boldsymbol{k}| = \frac{2\pi}{\lambda,} \tag{3.14}$$

where λ is the vacuum wavelength. The wave vector $\boldsymbol{k}$ describes the actual direction of the ray. The propagation constant $\boldsymbol{\beta}$ gives an effective value for the propagation constant along the fibers. Geometrically, $\boldsymbol{\beta}$ is the projection of $n_{\mathrm{co}}\boldsymbol{k}$ on the fiber axis, thus $\boldsymbol{\beta} = \beta \boldsymbol{e}_z = n_{\mathrm{co}} \boldsymbol{k} \sin(\alpha) \boldsymbol{e}_z$, where α is the angle between the ray and the surface normal and $\boldsymbol{e}_z$ is the unit vector pointing in the z-direction. Here we use $n_{\mathrm{co}}\boldsymbol{k}$ because the ray is propagating in a medium, which decreases λ and consequently increases the wave number in the medium.

Consequently, $\boldsymbol{\beta}$, $\boldsymbol{\beta}_{\mathrm{t}}$ and $\boldsymbol{k}$ have to fulfill the equations

$$\begin{aligned} n_{\mathrm{co}} \boldsymbol{k} &= \boldsymbol{\beta} + \boldsymbol{\beta}^{\mathrm{t}} \quad \text{and} \\ n_{\mathrm{co}}^2 k^2 &= \beta^2 + (\beta^{\mathrm{t}})^2, \end{aligned} \tag{3.15}$$

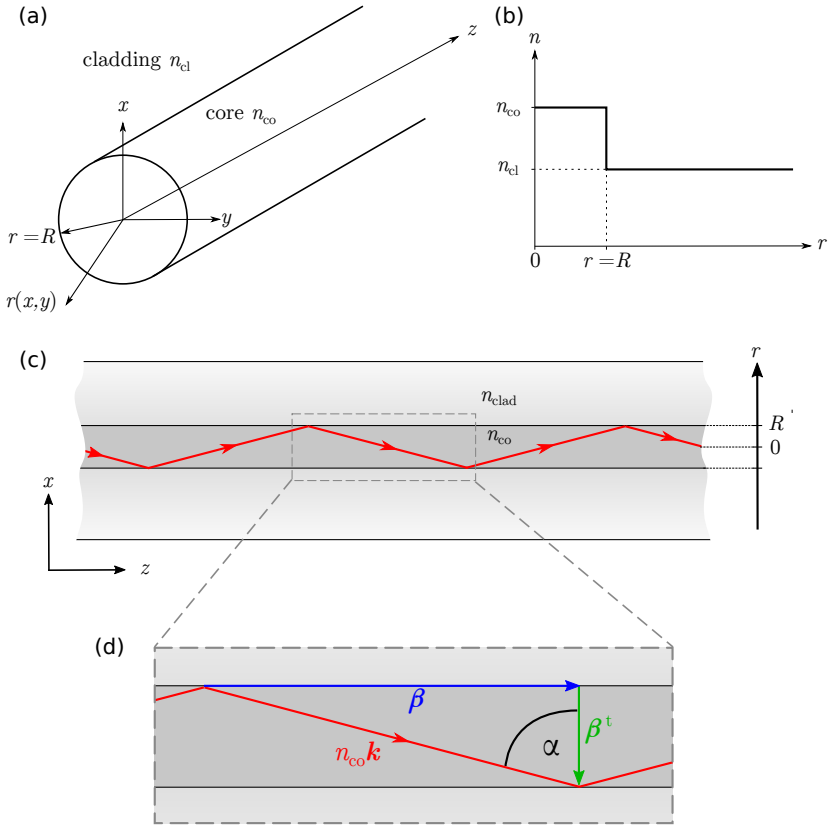

Figure 3.1. (a) Sketch of a circular step index fiber with core radius R, core refractive index n_{co} and cladding refractive index n_{cl}. The origin of the coordinate system is placed in the center of the fiber. (b) Refractive index distribution as function of the radius. (c) Side view of a fiber with a propagating ray confined to the core by total internal reflection. (d) Magnified section of the core depicting the wave vector $\boldsymbol{k}$, the propagation vector $\boldsymbol{\beta}$ and the transverse propagation vector vector $\boldsymbol{\beta}_t$.

where $\beta^t = |\boldsymbol{\beta}^t|$. The absolute values of $\boldsymbol{\beta}$ and $\boldsymbol{\beta}^t$ are called the propagation constant and the transverse propagation constant, respectively. Another quantity of high importance is the effective refractive index

$$n_{eff} = \frac{\beta}{k}. \tag{3.16}$$

The effect refractive index (or effective index) is often used to characterize the wave propagation. The larger the angle α the higher n_{eff}. The upper limit of n_{eff} is therefore given by n_{co} for $\alpha \to \pi/2$ because then the direction of ray approaches the propagation vector, i. e. $n_{co}\boldsymbol{k} \to \boldsymbol{\beta}$. From Eq. (3.16) then follows that $n_{eff} \to n_{co}$.

The lower limit is set by n_{cl} due to Snell's law [51, p. 33-1]. If $n_{eff} < n_{cl}$, the ray does not fulfill the requirement for total internal reflection and would lose power while propagating. Consequently, the range for n_{eff} is

$$n_{co} > n_{eff} > n_{cl}. \tag{3.17}$$

Even though there are more properties, which can be extracted from the ray picture (see for example [72, Chap. 2]), we have captured the essence and therefore we conclude the discussion here. In the following, we will describe the circular waveguide in terms of the wave equation we derived above (Eq. (3.10)). With this approach we will be able to take into account the anisotropy of the materials.

3.3.2. Wave equation for optical waveguides

3.3.2.1. Formulation of the wave equation

For the discussion of the ray picture we assumed that core and cladding in the wave guiding structure in Fig. 3.1 are isotropic. However, in the inhomogeneous wave equations (3.10) and (3.12) we use a second rank tensor to be able to describe wave guiding in media, which are generally ansiotropic. This is very useful for handling wave guiding in liquid crystals especially in structures like the radial escaped director field we discussed in Sec. 2.5.

However, often there are no analytic solutions for a given dielectric tensors. Then numerical methods, e. g. finite element methods, have to be used. One prominent example for which analytical solutions exist is the uniaxial step index fiber. In this case both, the core and the cladding material, can be unixial.

As it turns out, the axial orientation of a liquid crystal inside a microcapillary (cf. Sec. 2.5) can be described as a unixial core material. As the cladding material is silica, the cladding is isotropic (even though the uniaxial step index fiber model is capable of handling a uniaxial cladding as well). So, the structure we will treat within this section is a step index fiber with an uniaxial core and an isotropic cladding.

With these restrictions, the dielectric tensor takes the form

$$\bar{\bar{\epsilon}}_r = \begin{cases} \mathrm{diag}\left((n_{\mathrm{co}}^{\mathrm{t}})^2, (n_{\mathrm{co}}^{\mathrm{t}})^2, (n_{\mathrm{co}}^{z})^2\right), & \text{inside the core,} \\ I_3 \cdot n_{\mathrm{cl}}^2, & \text{otherwise.} \end{cases}$$

Here, $n_{\mathrm{co}}^{\mathrm{t}}$ is the transverse refractive index and n_{co}^{z} the refractive index along the z-axis [†], diag$(\cdot)$ denotes a diagonal matrix and I_3 is the identity matrix. Even though in reality the cladding is of finite extent, for the analytical calculation an infinite cladding is assumed.

The solutions of Eqs. (3.10) and (3.12), which we are looking for, are time periodic and should not change their shape while propagating along the fiber axis (z-direction) except spatial oscillations according to the propagation constant β.

[†] In the case of the axially aligned liquid crystal in a microcapillary, we set $n_{\mathrm{co}}^{\mathrm{t}} = n_{\mathrm{o}}$ and $n_{\mathrm{co}}^{z} = n_{\mathrm{e}}$, where n_{o} and n_{e} are the ordinary and the extraordinary refractive index of the liquid crystal.

Consequently, the solutions will have the form

$$\boldsymbol{E}(x,y,z,t) = \boldsymbol{E}(x,y)\exp\left[\imath\left(\omega t - \beta z\right)\right]. \tag{3.18}$$

With these restrictions to the sought-after solutions, Eqs. (3.10) and (3.12) read [72]

$$\left[\nabla_\mathrm{t}^2 + k^2 n_z^2 - \beta^2\left(\frac{n_z}{n_\mathrm{t}}\right)^2\right] E_z = -\imath\beta\left(\boldsymbol{E}_\mathrm{t}\cdot\nabla_\mathrm{t}\ln n_\mathrm{t}^2\right) \tag{3.19a}$$

$$\left[\nabla_\mathrm{t}^2 + k^2 n_\mathrm{t}^2 - \beta^2\right] H_z = \left(\nabla_\mathrm{t} H_z - \imath\beta\boldsymbol{H}_\mathrm{t}\right)\nabla_\mathrm{t}\ln n_\mathrm{t}^2 \tag{3.19b}$$

where $\nabla\mathrm{t} = \left(\frac{\partial}{\partial x}, \frac{\partial}{\partial y}, 0\right)$ and $\boldsymbol{E}_\mathrm{t}$ and $\boldsymbol{H}_\mathrm{t}$ are the transverse components of $\boldsymbol{E}$ and $\boldsymbol{H}$, respectively. In the above equations, we only consider the fields in z-direction because if those are known, the transverse fields $\boldsymbol{E}_\mathrm{t}$ and $\boldsymbol{H}_\mathrm{t}$ can be obtained by [72]

$$\boldsymbol{E}_\mathrm{t} = \frac{\imath}{k^2 n^2 - \beta^2}\left[\beta\nabla_\mathrm{t} E_z - \left(\frac{\mu_0}{\epsilon_0}\right)^{\frac{1}{2}} k\boldsymbol{e}_z\times\nabla_\mathrm{t} H_z\right] \tag{3.20a}$$

$$\boldsymbol{H}_\mathrm{t} = \frac{\imath}{k^2 n^2 - \beta^2}\left[\beta\nabla_\mathrm{t} H_z + \left(\frac{\epsilon_0}{\mu_0}\right)^{\frac{1}{2}} kn^2\boldsymbol{e}_z\times\nabla_\mathrm{t} E_z\right]. \tag{3.20b}$$

As the core and the cladding are homogeneous, the terms on the right hand side of Eqs. (3.19a) and (3.19b) only come into play at the boundaries. Within the core and the cladding the homogeneous versions of Eq. (3.19) hold:

$$\left[\nabla_\mathrm{t}^2 + k^2 n_z^2 - \beta^2\left(\frac{n_z}{n_\mathrm{t}}\right)^2\right] E_z = 0 \tag{3.21a}$$

$$\left[\nabla_\mathrm{t}^2 + k^2 n_\mathrm{t}^2 - \beta^2\right] H_z = 0 \tag{3.21b}$$

To find the solutions to these equations, we first transform them from Cartesian coordinates (x, y) into cylindrical coordinates (r, ϕ), which gives

$$\left(\frac{\partial^2}{\partial\rho^2} + \frac{1}{\rho}\frac{\partial}{\partial\rho} + \frac{1}{\rho^2}\frac{\partial^2}{\partial\phi^2} + U^2\right) E_z = 0 \quad \text{for} \quad 0 \le \rho \le 1 \tag{3.22a}$$

$$\left(\frac{\partial^2}{\partial\rho^2} + \frac{1}{\rho}\frac{\partial}{\partial\rho} + \frac{1}{\rho^2}\frac{\partial^2}{\partial\phi^2} - W^2\right) E_z = 0 \quad \text{for} \quad 1 < \rho < \infty \tag{3.22b}$$

where $\rho = r/R$ is the normalized radial component and U and W are given by

$$U = R\left[k^2(n_{\mathrm{co}}^{\mathrm{t}})^2 - \beta^2\kappa_{\mathrm{co}}^2\right]^{\frac{1}{2}}, \tag{3.23}$$

$$W = R\left[\beta^2 - k^2 n_{\mathrm{cl}}^2\right]^{\frac{1}{2}}, \tag{3.24}$$

$$V = R\left[k^2(n_{\mathrm{co}}^{\mathrm{t}})^2 - k^2 n_{\mathrm{cl}}^2\right]^{\frac{1}{2}} = \left[U^2 + W^2\right]^{\frac{1}{2}}, \tag{3.25}$$

where $\kappa_{\mathrm{co}} = \frac{n_{\mathrm{co}}^z}{n_{\mathrm{co}}^{\mathrm{t}}}$. Additionally to U and W we listed the V parameter which is also called the normalized frequency. This parameter is an important quantity in characterizing optical fibers and we will discuss it in more detail in Sec. 3.3.3.3.

We already encountered the U parameter in slightly different from when we discussed the transverse propagation constant β_{t} [cf. Eq. (3.15)]. The U parameter is therefore the dimensionless form of β_{t}. The W parameter is the analog of the U parameter in the cladding, i. e. for $\rho > 1$.

Equations for the magnetic field H_z analog to Eqs. (3.22a) and (3.22b) are obtained by replacing E_z with H_z and n_{co}^z with $n_{\mathrm{co}}^{\mathrm{t}}$, setting $\kappa_{\mathrm{co}} = 1$ in Eq. (3.23).

3.3.2.2. Solution of the wave equation

The Eqs. (3.22) can be solved by separating the ρ- and ϕ-depending terms [73]. The solutions will then be of the form

$$E_z \propto f_\nu(\rho) g_\nu(\phi), \tag{3.26}$$

where f_ν and g_ν are the solutions to the separated ordinary differential equations (ODEs). The ρ-dependent ODE is solved by

$$f(\rho) = \begin{cases} J_\nu(U\rho) & \text{for } \rho \leq 1 \\ K_\nu(W\rho) & \text{for } \rho > 1 \end{cases} \tag{3.27}$$

where ν is the radial mode order and J_ν and K_ν are the Bessel functions of first kind and the modified Bessel functions of second kind [72, p. 249].

The angular dependence is easily solved by

$$g_\nu(\rho) = \begin{cases} \cos(\nu\phi) & \text{for even modes,} \\ \sin(\nu\phi) & \text{for odd modes.} \end{cases} \tag{3.28}$$

This means that for each $\nu \neq 0$ there exist two different solutions which either have a cosine or a sine dependence on ϕ. Equation (3.28) forces ν to be an integer. In the case of $\nu = 0$, $g_0 = 1$ holds.

The full equations for the z-component of the electric and magnetic fields then read

$$E_z = AJ_\nu(U\rho)g_\nu(\phi), \qquad H_z = CJ_\nu(U\rho)h_\nu(\phi), \qquad \text{for } \rho \leq 1, \tag{3.29a}$$

$$E_z = BK_\nu(W\rho)g_\nu(\phi), \qquad H_z = DK_\nu(W\rho)h_\nu(\phi), \qquad \text{for } \rho > 1, \tag{3.29b}$$

with

$$h_\nu(\rho) = \begin{cases} -\sin(\nu\phi) & \text{for even modes,} \\ +\cos(\nu\phi) & \text{for odd modes} \end{cases} \tag{3.30}$$

and A, B as the electric field amplitudes and C, D as the magnetic field amplitudes. Here, again $h_\nu = 1$ for $\nu = 0$. From Eq. (3.1) we know that tangential fields are equal at both sides of the boundary, i. e.

$$\begin{aligned} AJ_\nu(U\rho)\big|_{\rho=1} &= BK_\nu(W\rho)\big|_{\rho=1}\,, \\ CJ_\nu(U\rho)\big|_{\rho=1} &= DK_\nu(W\rho)\big|_{\rho=1}\,. \end{aligned}$$

To solve for the four unknowns A, B, C and D, two more equations are required. Those are obtained from the tangential components E_ϕ and H_ϕ, which are also continuous across the boundary. From Eqs. (3.22) we known that these equations will contain the four desired coefficients. All four equations can be assembled into a linear system of equations which is solvable if the condition [73]

$$\left(\frac{J'_\nu(U)}{UJ_\nu(U)} + \frac{K'_\nu(W)}{WK_\nu(W)}\right)\left(\kappa_{\text{co}}\frac{J'_v(U)}{UJ_v(U)} + \left(\frac{n^{\text{t}}_{\text{cl}}}{n^{\text{t}}_{\text{co}}}\right)^2\frac{K'_\nu(W)}{WK_\nu(W)}\right) = \nu^2\left(\frac{\beta}{kn^{\text{t}}_{\text{co}}}\right)^2\left(\frac{V}{UW}\right)^4 \tag{3.31}$$

is fulfilled. In this equation, $J'_\nu(U)$ and $W'_\nu(K)$ denote the derivatives of $J_\nu(U)$ and $W_\nu(W)$ with respect to the arguments U and W. This equation is called the characteristic or eigenvalue equation. The equation has to be solved numerically as it is an implicit equation. By solving it we obtain the propagation constant β because U and W solely depend on β, other quantities are determined through the materials [cf. Eqs. (3.23) and (3.24)].

The eigenvalue equation (3.31) in general has multiple solutions, which then correspond to different optical modes with different propagation constants. These modes can be classified in four different types. Each of these types can again have multiple solutions. The number of possible solutions increases with the V parameter [Eq. (3.25)]. In the following sections we will therefore discuss the different modes, which can appear in optical fibers and their relation to the V parameter.

3.3.3. Fiber modes

The eigenvalue equation (3.31) is complicated and can be difficult to solve. For the sake of capturing the essence of the mode classification we will assume that the fiber is isotropic. Along the discussion we will mention where the anisotropy would lead to different results.

Assuming that the fiber is isotropic helps to classify the modes into the four categories: transverse magnetic (TM) modes, transverse electric (TE) modes and to sets of hybrid modes, HE and EH. We will discuss the properties of these types in the following.

3.3.3.1. Transverse electric (TE) and transverse magnetic (TM) modes

The simplest solutions to the eigenvalue equation (3.31) can be found by setting $\nu = 0$, which means that the resulting modes are indepent of ϕ. This then leads to the simplified eigenvalue equations

$$\frac{J_1(U)}{UJ_0(U)} + \frac{n_{\mathrm{cl}}^2}{n_{\mathrm{co}}^2}\frac{K_1(W)}{WK_0(W)} = 0 \qquad (\mathrm{TM}_{0m}\text{ modes}) \tag{3.32}$$

$$\frac{J_1(U)}{UJ_0(U)} + \frac{K_1(W)}{WK_0(W)} = 0 \qquad (\mathrm{TE}_{0m}\text{ modes}). \tag{3.33}$$

Here, the identities $J_0' = -J_1$ and $K_0' = -K_1$ have been used [74].

We can solve Eqs. (3.33) and (3.32) graphically by separately plotting curves for $\frac{J_1(U)}{UJ_0(U)}$, $\frac{K_1(W)}{WK_0(W)}$ (TE modes) and $\frac{n_{\mathrm{cl}}^2}{n_{\mathrm{co}}^2}\frac{K_1(W)}{WK_0(W)}$ (TM modes) as functions of U. The desired value for U can then be obtained by evaluating the intersections of the curves. This procedure is illustrated in Fig. 3.2 for a fixed V-parameter of $V = 7$). We find two solutions for the TE and TM modes. As there are multiple solutions, the notation $\mathrm{TE}_{\nu,m}$ is employed. ν is in general zero for TE and TM modes. The order of the solution is the indicated by m. Thus the solutions we found are called TE_{01}, TE_{02}, TM_{01} and TM_{02}.

The difference between TE and TM modes in U solely appear to the factor $\frac{n_{\mathrm{cl}}}{n_{\mathrm{co}}}$. In Fig. 3.2 we used $\frac{n_{\mathrm{cl}}}{n_{\mathrm{co}}} = 0.75$ [†] to make the difference between TE and TM modes clearly visible. In reality the difference is much smaller. Often the approximation $n_{\mathrm{co}} \to n_{\mathrm{cl}}$ is made, which leads to the degeneracy of TE and TM modes. This approximation is called the weakly guiding approximation [4].

In Fig. 3.3 we plot the absolute electric field of the first two TE and TM modes. They both exhibit the expected radial symmetry. The direction of the electric field is indicated by the white arrows. This makes clear that for the TE modes [Fig. 3.3 (a,b)] the electric field only exhibits an azimuthal component while the remaining components are zero ($E_r, E_z = 0$). The vanishing E_z component coined

[†] A ratio for $\frac{n_{\mathrm{cl}}}{n_{\mathrm{co}}}$ of 0.75 would mean that for a silica cladding with refractive index of $n_{\mathrm{cl}} = 1.46$ the core index would be around $n_{\mathrm{co}} = 1.95$ which is far away from core indices used in applications. A realistic value would be $n_{\mathrm{co}} = 1.47$, i. e. $\frac{n_{\mathrm{cl}}}{n_{\mathrm{co}}} = 0.99$.

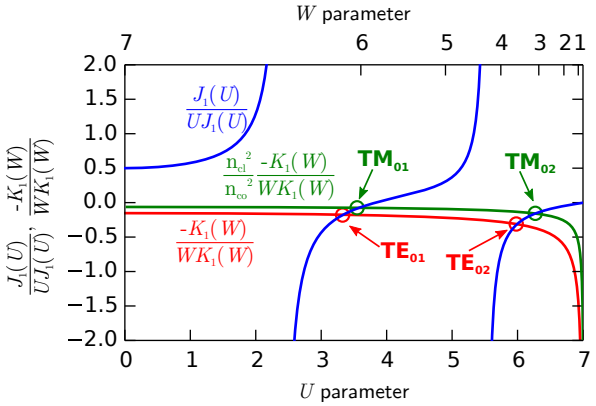

Figure 3.2. Graphical evaluation of the TE and TM eigenvalue equations for $V = 7$. V-dependent term in blue, W-dependent terms in red (TE) and green (TM). The circles mark the solutions of the eigenvalue equation. For $n_{\mathrm{cl}}/n_{\mathrm{co}}$ a value of 0.75 is assumed.

the name transverse electric. In analogous fashion, the TM modes have no magnetic field in r- and z-direction.

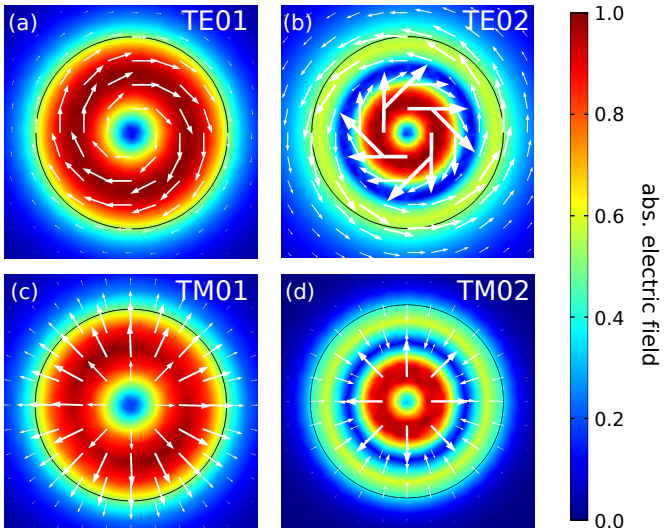

Figure 3.3. Absolute electric field (surface plot) of the transverse electric (TE_{0m}) eigenmodes and transverse magnetic (TM_{0m}) of a step index fiber: (a) TE_{01}, (b) TE_{02}, (c) TM_{01} and (d) TM_{02}. White arrows indicate the direction and magnitude of the transverse electric field.

The TE_{02} distinguishes itself from the TE_{01} mode by an additional node in the radial distribution of the electric field. This is a general observation which will continue: for each higher modal number, an additional node is added. A second observation is that the field distribution spreads out further into the cladding with higher order modes. Both of these observations are also valid for the TM modes and also the HE and EH modes, which we will discuss next.

3.3.3.2. Hybrid modes

All solutions of Eq. (3.31) which do not have $\nu = 0$ are called hybrid modes. Hybrid modes exhibit non-zero electric *and* magnetic fields in the z-direction which distinguishes them from TE or TM modes, for which either E_z or H_z vanishes. Hybrid modes are classified into EH and HE modes [75].

To understand the essence of this classification, we apply the weak guiding approximation ($n_{\mathrm{co}} \to n_{\mathrm{cl}}$), which we briefly discussed above, to the eigenvalue equation (3.31). After taking the square root [73], the equation then reads

$$\left(\frac{J'_\nu(U)}{UJ_\nu(U)} + \frac{K'_\nu(W)}{WK_\nu(W)}\right) = \pm\nu\left(\frac{\beta}{kn_{\mathrm{co}}^{\mathrm{t}}}\right)\left(\frac{V}{UW}\right)^2. \tag{3.34}$$

For $\nu > 1$, the EH and HE categorization then applies to the right hand side being either positive (EH) or negative (HE). With this in mind, Eq. (3.34) can be rearranged to distinguish the eigenvalue equations for EH and HE modes [73, p. 82f.]

$$U\frac{J_\nu(U)}{J_{\nu+1}(U)} = -W\frac{K_\nu(W)}{W_{\nu+1}(W)} \qquad \text{for} \quad \nu \geq 1 \quad \text{(EH modes)}, \tag{3.35}$$

$$U\frac{J_\nu(U)}{J_{\nu-1}(U)} = W\frac{K_\nu(W)}{W_{\nu-1}(W)} \qquad \text{for} \quad \nu \geq 1 \quad \text{(HE modes)}. \tag{3.36}$$

These two equations have a very similar structure and due to the properties of the Bessel functions EH and HE modes are often degenerate but with different orders ν. For example the lowest order EH_{11} is degenerate with the HE_{31} mode and also the HE_{21} and EH_{41} modes are degenerate [73, p. 66].

In Fig. 3.4 we plotted the modal field distributions of the HE_{11}, HE_{21} and HE_{21} modes. We already have established that these modes are each two-fold degenerate due to the angular dependence. The lowest order mode is HE_{11} [Fig. 3.4 (a,b)], which is almost linearly polarized in x- or y-direction. The degree of linear polarization depends on the index difference between core and cladding. In the case of the weak guidance approximation, these modes are purely linear polarized.

This is different for the next higher mode HE_{21} [Fig. 3.4 (c, d)], which exhibits an angular dependence for the x and y components of the electric field. In Sec. 3.3.3.1, we already discussed higher order solutions ($m > 1$) for a given ν. The same observation are made for the HE_{12} modes [Fig. 3.4 (e, f)]. The higher mode order adds an additional node to the radial distribution. And the electric field distribution is spread out further into the cladding.

We discussed the hybrid modes in context of the weak guidance approximation. For the TE and TM modes we observed, that if we do not make this approximation the degeneracy between TE and TM modes is lifted. Analogous, this will also be true for the hybrid modes: EH and HE modes will no longer be degenerate. However, the differences typically will be small.

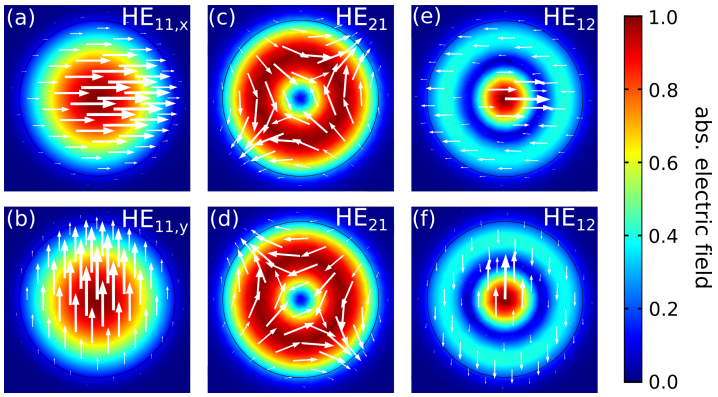

Figure 3.4. Absolute electric field of the hybrid eigenmodes of a step index fiber: (a) $HE_{11,x}$, (b) $HE_{11,y}$, (a) $HE_{21,x}$, (b) $HE_{21,y}$, (a) $HE_{12,x}$ and (b) $HE_{12,y}$. In the limit of identical core and cladding index ($n_{co} \to n_{cl}$), the HE_{11} become linearly polarized.

Besides the weak guidance approximation, we considered only isotropic materials. From the exact eigenvalue eqauation (3.31) it is clear, that introducing uniaxialty into the waveguide core will also lift the degeneracy of EH and HE modes.

3.3.3.3. V-Parameter, number of modes and modal cutoff

We have seen that there can be multiple solutions to the eigenvalue equation (3.31), which correspond to the different modes. So a natural question is how many modes there actually exist. From the example of the TE and TM modes we have seen that higher order solutions will have a larger U-parameter. Thus the possible values for U determine the number of modes. The upper bound for U is given by the V parameter [cf. Eqs. (3.23) through (3.25)].

We defined V previously to be

$$V = R\left[k^2(n_{co}^t)^2 - k^2 n_{cl}^2\right]^{\frac{1}{2}} = \left[U^2 + W^2\right]^{\frac{1}{2}}. \tag{3.25}$$

Thus, V depends on the refractive index of core n_{co} and cladding n_{cl}, the core radius R and the wavelength λ through $k = 2\pi/\lambda$. So for a given waveguide, the V number changes with the wavelength.

In Fig. 3.5 we solved the eigenvalue equation Eq. (3.31) for different V numbers and plot the corresponding U value we find. We see that the first mode, which appears is the HE_{11} mode. Even in the case that $V \to 0$ (or $n_{co} \to n_{cl}$ this mode remains. The HE_{11} mode is called the fundamental mode, which is always present. All other modes appear at higher V. A critical V value for optical fibers is 2.405, which is the value where the next higher mode will appear. Below this value, the fiber is called a single mode fiber (not counting the degeneracy of the HE_{11} mode).

Each of the modes we discussed above has a critical V value. It is called the cutoff value because below this value the mode is no longer guided. The cutoff value can

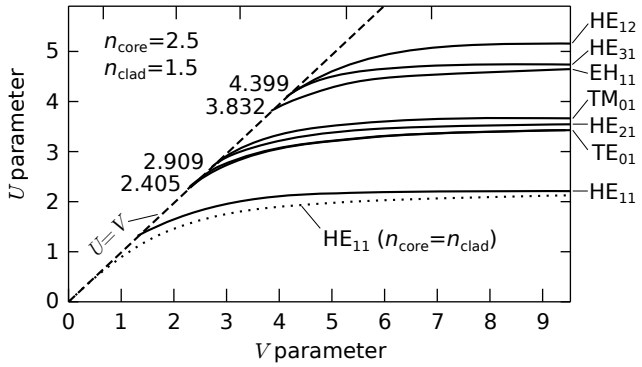

Figure 3.5. U-parameter as a function of the dimensionless frequency V. With increasing V more modes are supported by the waveguide structure. Again, we assume $n_{cl}/n_{co} = 0.75$ except for the dotted line of the HE_{11}, which shows the limiting case $n_{co} \to n_{cl}$.

be found from the eigenvalue equation by setting $U = V$ and consequently $W = 0$. This condition is represented by the dashed diagonal in Fig. 3.5. In the previous sections we derived simplified versions of the eigenvalue equation for the different mode types, in Tab. 3.1 we display the corresponding cutoff conditions.

Table 3.1. Cutoff conditions for the different mode types, where $\Delta = (n_{co}^2 - n_{cl}^2)/(2n_{co}^2)$.

mode	cutoff condition
TE_{0m}, TM_{0m}	$J_0(U) = 0$
HE_{1m}	$J_1(U) = 0$
EH_{ν}	$J_\nu(U) = 0$
$HE_{\nu m}(\nu > 1)$	$\frac{V}{\nu-1}\frac{J_{\nu-2}(V)}{J_{\nu-1}(V)} + \frac{2\Delta}{1-2\Delta} = 0$

Figure 3.5 clearly shows the the number of modes increases with increasing V. An approximate formula of the number of modes N, which exist for a given mode, is given by [76]

$$N \approx \frac{1}{2}V^2. \tag{3.37}$$

We briefly want to mention what happens with the modes below the cutoff frequency. Even though the mode is no longer perfectly guided along the waveguide, the modal structure still persists. This is because the cutoff mode still fulfills each property of the guided mode except one. When we introduced the ray picture in Sec. 3.3.1, we pointed out that the basic guiding mechanism is total internal reflection. This is not fulfilled anymore by cutoff modes. This means that every time the ray hits the wall it loses some of its power and thus decays over the propagation length. This coined the name *leaky modes*.

We still can describe leaky modes as an optical mode of the waveguide, but its effective refractive n_{eff} is smaller than the refractive index of the cladding n_{cl}, i. e. $n_{eff} < n_{cl}$. This is opposed to the case of a guided mode, where we had $n_{co} > n_{eff} >$

n_{cl}. The concept of leaky modes will become important when we will describe the anti-resonant reflecting optical waveguide (ARROW) model for photonic band gap fibers in Sec. 3.5.2.1.

3.3.3.4. Mode field diamater

In the discussion of the transverse modes we saw that higher order modes reach further into the cladding. Therefore, an important quantity, which has been introduced, is the mode field diameter (MFD). It gives a measure for the diameter exhibited by a certain mode. This value increases with decreasing V-paramter. The MFD is defined as outer radial position where the intensity drops down to $1/\mathrm{e}^2$. The value can be found by

$$\mathrm{MFD} = 2\sqrt{2}\left[\frac{\int_0^\infty E^2(r) r^3 \,\mathrm{d}r}{\int_0^\infty E^2(r) r \,\mathrm{d}r}\right]^{1/2}, \tag{3.38}$$

where E is the absolute electric field. An approximate expression has been derived by Hussey et al. [77] which solely depends on the V-parameter:

$$\mathrm{MFD} \approx R\left(0.634 + 1.619V^{-3/2} + 2.879V^{-6} - 1.561V^{-7}\right). \tag{3.39}$$

As an example, we consider the radial symmetric HE_{11} mode in Fig. 3.6 (a). The result of Eq. (3.39) for different V values is plotted in Fig. 3.6. It shows that with increasing wavelength (decreasing V) the MFD increases, which means that it penetrates further into the cladding. The field reaching into the cladding is called the evanescent field. It decays approximately exponentially, which is a property of the modified Bessel function K we used to describe the fields extending into the cladding. The evanescent field will be an important factor when we discuss the interaction of coupled waveguides in Sec. 3.4.

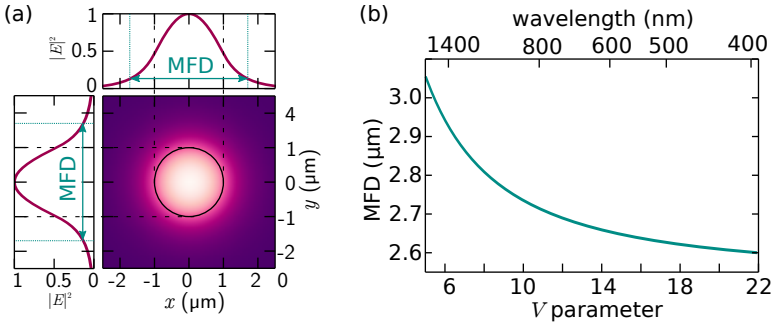

Figure 3.6. (a) The surface plot shows the absolute square electric field distribution of a HE_{11} mode. The line plots show cuts along the $x(y = 0)$ and $y(x = 0)$ axis. The mode field diameter (MFD) is marked. (b) Change of the MFD with the V-parameter (or wavelength).

3.4. Coupled mode theory

3.4.1. Basic principle

Our aim is to describe an optical fiber which has two non-intersecting core regions [Fig. 3.7 (a)] running parallel within a shared cladding. In the upcoming experiments, one core will be made of solid glass (Germanium doped silica). The other core consists of a liquid crystal with the molecules aligned along the fiber axis. The second core is therefore uniaxial. In general the refractive indices and the radii of the two cores are different [cf. Fig. 3.7 (b)].

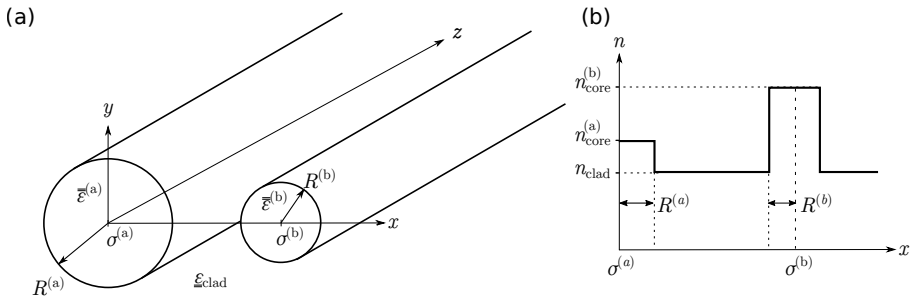

Figure 3.7. (a) Schematic of two dissimilar waveguides in close vicinity with the permittivity tensor $\bar{\bar{\epsilon}}^{(\psi)}$, the center position $\sigma_{(\psi)}$ and core radius $R^{(\psi)}$ with $\psi = a, b$ for the corresponding waveguide. Both waveguides share the same cladding with the perimittivity $\bar{\bar{\epsilon}}_{\mathrm{cl}}$.

From Sec. 3.3, we already know the modes of the isolated waveguides. If the two waveguides are very far apart from each other, those solutions will be the solutions of the (extreme weakly) coupled system. However, when the separation is reduced, they will start to interact with each other by their evanescent fields. Then, the solutions for the coupled waveguide will somehow differ from the solutions of the isolated waveguides.

The coupled mode theory has first been developed for metal waveguides in the microwave region [78–80]. The application of the idea to parallel dielectric waveguides started with Marcuse in 1971 [81]. Since then the theory has been developed further and is still under developement [82].

Within the coupled mode theory (CMT), the electromagnetic modes of the composite waveguide are approximated by linear superposition of the isolated waveguide modes [83–86]. The electric and magnetic fields, $\boldsymbol{E}$ and $\boldsymbol{H}$, of the waveguides (a) and (b) in isolation can be separated into transversal and longitudinal components (as we have seen before)

$$\boldsymbol{E}^{(a)} = \boldsymbol{E}_{\mathrm{t}}^{(a)} + \boldsymbol{E}_{z}^{(a)} \tag{3.40a}$$

$$\boldsymbol{H}^{(a)} = \boldsymbol{H}_{\mathrm{t}}^{(a)} + \boldsymbol{E}_{z}^{(a)}, \tag{3.40b}$$

where (a) denotes the first waveguide, t the transverse components and z the longitudinal components. An analogous set of equations exists for the second waveguide (b).

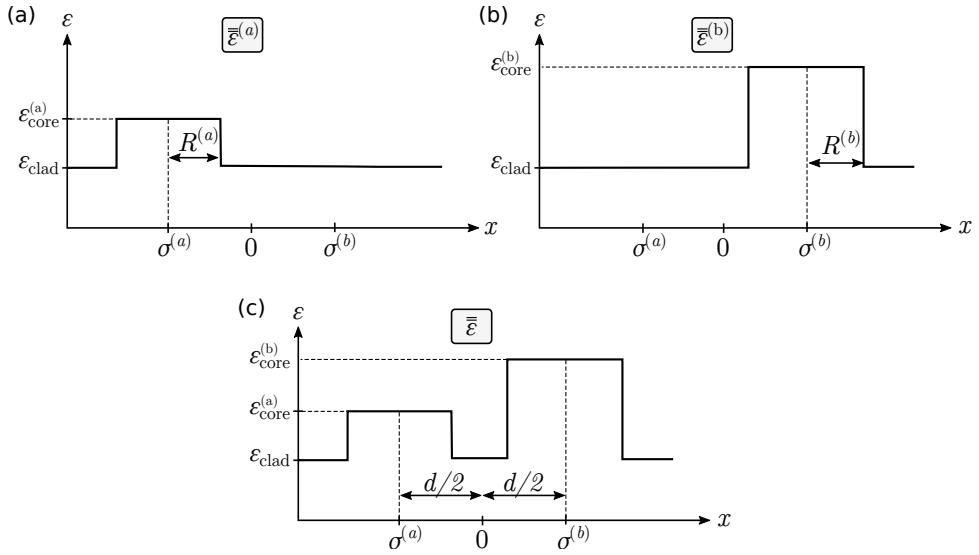

Figure 3.8. Dielectric profiles of (a) waveguide (a) in isolation ($\bar{\bar{\epsilon}}^{(a)}$), (b) waveguide ($b$) in isolation ($\bar{\bar{\epsilon}}^{(b)}$) and (c) the waveguide system ($\bar{\bar{\epsilon}}$).

Using the fields of the single waveguides, the propagating field of the composite waveguide is approximated by

$$\boldsymbol{E}_{\text{t}} \simeq u^{(a)}(z)\boldsymbol{E}_{\text{t}}^{(a)} + u^{(b)}(z)\boldsymbol{E}_{\text{t}}^{(b)} \tag{3.41a}$$

$$\boldsymbol{H}_{\text{t}} \simeq u^{(a)}(z)\boldsymbol{H}_{\text{t}}^{(a)} + u^{(b)}(z)\boldsymbol{H}_{\text{t}}^{(b)} \tag{3.41b}$$

for the transversal fields and

$$\boldsymbol{E}_z \simeq u^{(a)}(z)\frac{\epsilon_z^{(a)}}{\epsilon_z}\boldsymbol{E}_z + u^{(b)}(z)\frac{\epsilon_z^{(b)}}{\epsilon_z}\boldsymbol{E}_z^{(b)} \tag{3.42a}$$

$$\boldsymbol{H}_z \simeq u^{(a)}(z)\boldsymbol{H}_z + u^{(b)}(z)\boldsymbol{H}_z^{(b)} \tag{3.42b}$$

for the longitudinal fields. The coefficients $u^{(a)}$, $u^{(b)}$ are z-dependent and describe – apart from the periodic variation $\exp\left(-\imath\beta^{(a,b)}z\right)$ due to the propagation constant $\beta^{(a,b)}$ – the change that occurs due to interactions of core and inclusion. The longitudinal electric field contains the dielectric profiles of the single waveguides $\epsilon^{(a)}$, $\epsilon^{(b)}$ and of the composite waveguide ϵ [cf. Fig. 3.8]. This is a necessity which follows directly from Maxwell's equations [84].

3.4.2. Coupled mode equations

As mentioned before, the coefficients $u^{(a)}$ and $u^{(b)}$ describe the evolution of the electromagnetic field along the propagation direction. The formulation of the corre-

sponding equations is purely mathematical and can be found in [87]. Therefore, we will here only give the result and then try to explain the important parameters.

The general idea is that it is possible to express the transverse components of the waveguide modes of waveguide (a) by a superposition of the modes in waveguide (b) (this includes radiation modes, cf. [72, p. 514]) and vice versa for the modes in waveguide (b). The corresponding equations then read

$$\begin{aligned} \boldsymbol{E}_{\mathrm{t},p}^{(a)} &= \sum_q A_{pq} \boldsymbol{E}_{\mathrm{t},p}^{(b)} \\ \boldsymbol{E}_{\mathrm{t},p}^{(b)} &= \sum_q B_{pq} \boldsymbol{E}_{\mathrm{t},p}^{(a)}, \end{aligned}$$

where A_{pq} and B_{pq} are the overlap integrals given by

$$A_{pq} = \frac{1}{2} \iint_{-\infty}^{\infty} \boldsymbol{E}_{\mathrm{t}}^{(p)} \times \boldsymbol{H}_{\mathrm{t}}^{(q)} \, \mathrm{d}x \, \mathrm{d}y, \tag{3.43}$$

and an analog version for B. From this relation, a matrix $\mathbf{C}$ is determined by $\mathbf{C} = \frac{1}{2}\left(\mathbf{A} + \mathbf{B}^{\mathrm{T}}\right)$, where T indicates the transposed matrix.

A graphical representation of the overlap integrals is shown in Fig. 3.9. This indicates that for increasing separation or decreasing mode field diameter the overlap integral will decrease.

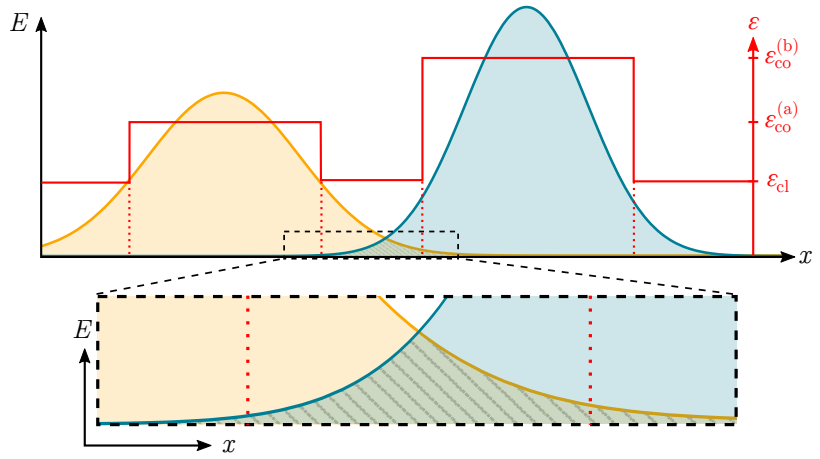

Figure 3.9. Waveguide modes of the isolated waveguides: orange for waveguide (a) and blue for waveguide (b). The refractive index profile ϵ (isotropic case) is indicated in red. The patterned region in the enlargement indicates the region of the modal overlap.

Equation (3.43) also gives a normalization condition for $p = q$, i. e.

$$\tilde{C}_{pp} = C_{pp} = \frac{1}{2} \iint_{-\infty}^{\infty} \boldsymbol{E}_{\mathrm{t}}^{(p)} \times \boldsymbol{H}_{\mathrm{t}}^{(p)} \, \mathrm{d}x \, \mathrm{d}y = 1. \tag{3.44}$$

Besides the overlap integrals, there exists a second matrix which describes the coupling due to the variations in the permittivities. The isolated waveguides have a different dielectric tensor distribution in comparison to the waveguide system Fig. 3.8 , which has to be taken into account. We previously defined the dielectric permittivities $\bar{\bar{\epsilon}}^{(a)}$ and $\bar{\bar{\epsilon}}^{(b)}$ for the waveguides (a) and (b) in isolation. The composite waveguide is described by $\bar{\bar{\epsilon}}$. The differences in dielectric tensor are then given by

$$\Delta\bar{\bar{\epsilon}}^{(\chi)} = \bar{\bar{\epsilon}} - \bar{\bar{\epsilon}}^{(\chi)}, \tag{3.45}$$

where $\chi = \{a, b\}$. These profiles are shown in Fig. 3.10 .

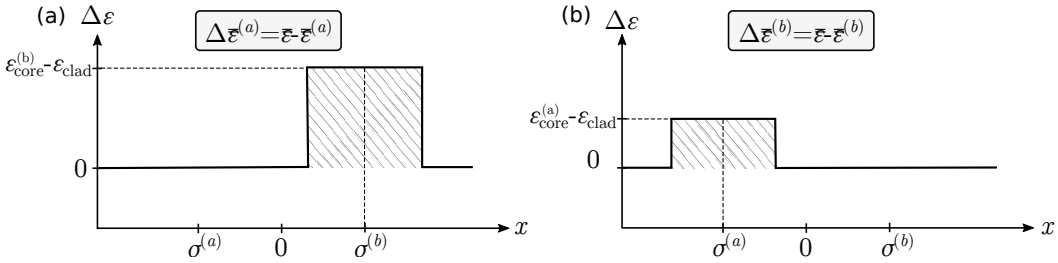

Figure 3.10. Differences between the dielectric profiles of the waveguide system and the waveguides in isolation (simplified to the isotropic case): (a) $\Delta\bar{\bar{\epsilon}}^{(a)} = \Delta\bar{\bar{\epsilon}} - \Delta\bar{\bar{\epsilon}}^{(a)}$ and (b) $\Delta\bar{\bar{\epsilon}}^{(b)} = \Delta\bar{\bar{\epsilon}} - \Delta\bar{\bar{\epsilon}}^{(b)}$.

The components of coupling matrix $\mathbf{K}$ can then be calculated by [87]

$$K_{pq} = \omega \iint_{-\infty}^{\infty} \Delta\epsilon^{(p)} \boldsymbol{E}_{\mathrm{t}}^{(p)} \boldsymbol{E}_{\mathrm{t}}^{(q)} - \frac{\epsilon^{(q)}\Delta\epsilon^{(p)}}{\epsilon} \boldsymbol{E}_{z}^{(p)} \boldsymbol{E}_{z}^{(q)} \,\mathrm{d}x\,\mathrm{d}y. \tag{3.46}$$

Here, p, q label any mode in the waveguides, where $\bar{\bar{\epsilon}}^{(p)}$ denotes the dielectric profile of the modes waveguide. Consquently, these coupling constants can couple a mode p of waveguide (a) with a mode q of waveguide (b). But it can also couple two modes q and p, which are both confined to same the waveguide (a) [or (b)]. The case that $p = q$ is called self-coupling. It describes the effect of the changed dielectric profile (by $\Delta\bar{\bar{\epsilon}}^{(p)}$) on the p-th mode. It should be noted, that the integrand in Eq. (3.46) only contributes in regions where $\Delta\bar{\bar{\epsilon}} \neq 0$. †

Now, with the overlap integrals $\mathbf{C}$ and the coupling coefficients $\mathbf{K}$, we can derive a coupled system of ordinary differential equations, which describe the evolution of the z-dependent coefficients $u^{(a)}$ and $u^{(b)}$. To this end, the coefficients are put into a column vector $\boldsymbol{U} = \left(u^{(a)}, u^{(b)}\right)^{\mathrm{T}}$ and the equation

$$\mathbf{C}\frac{\mathrm{d}\boldsymbol{U}}{\mathrm{d}z} = \imath\left(\mathbf{B}\mathbf{C} + \mathbf{K}\right)\boldsymbol{U}, \tag{3.47}$$

†Consequently, there is no coupling between the modes of an isolated waveguide (i. e.$\Delta\bar{\bar{\epsilon}} = 0$. This is to be expected as the solutions to the wave equation Eq. (3.19) are orthogonal.

has to be solved [87, 88], where $\mathbf{B} = \mathrm{diag}(\beta^{(a)}, \beta^{(b)})$ is a diagonal matrix containing the propagation constants, $\mathbf{K}$ a matrix containing the coupling coefficients. Here we assume, that there is only a single mode present in each of the waveguides (a) and (b). These equations can also be used for the coupling of multiple modes [87] and also for systems with more than two waveguides [83, 89].

Equation (3.47) can be recast into a simpler form by multiplying $\mathbf{C}^{-1}$ from the left and using $\mathbf{M} = \mathbf{C}^{-1}\mathbf{B}\mathbf{C} + \mathbf{C}^{-1}\mathbf{K}$:

$$\frac{\mathrm{d}\boldsymbol{U}}{\mathrm{d}z} = \imath\mathbf{M}\boldsymbol{U}. \tag{3.48}$$

Since $\mathbf{M}$ is independent of the propagation distance, equation Eq. (3.48) is solved by [83, 90]

$$\boldsymbol{U} = \exp(\imath\mathbf{M}z)\,\boldsymbol{U}_0, \tag{3.49}$$

where $\boldsymbol{U}_0$ is the initial excitation in terms of modes of the single waveguides.

From this equation, the procedure to find the evolution of light coupled into the waveguide systems in terms of isolated waveguide modes is as follows:

1. Determine modes of waveguides (a) and (b).
2. Express inital excitation of the waveguide system by superposition of the isolated wavguide modes.
3. Calculate overlap integral $\mathbf{C}$ and coupling constant $\mathbf{K}$ of the involved modes.
4. Calculate matrix $\mathbf{M}$ and use Eq. (3.49) to obtain evolution of the inital field.

Calculating the $\mathbf{C}$ and $\mathbf{K}$ has to be performed numerically. There exist some analytical approximations [91], though.

We started out by stating that the modes of the coupled waveguide system can be well approximated by a superposition of the guided modes of the isolated waveguides with the z-varying prefactors $u^{(a)}$ and $u^{(b)}$. [†] If we consider again Eq. (3.48) and assume that $\boldsymbol{U} = \left(u^{(a)}, u^{(b)}\right)^{\mathrm{T}}$ is an eigenvector of $\mathbf{M}$, then

$$\imath\mathbf{M}\boldsymbol{U} = \imath\gamma_k\boldsymbol{U},$$

where γ_k with $k = \{\mathrm{s}, \mathrm{a}\}$ are the z-independent eigenvalues. This means there are excitations in terms of the single waveguides which do not change in amplitude during propagation (apart from $\exp(\imath\gamma_k z)$). These solutions are called normal modes or super modes and their propagation constants are different from the propagation constants of the isolated waveguides. In the case of two waveguides with to interacting modes, there exist two orthogonal eigenvectors U_s and U_a. The subscripts s and a stand for symmetric and antisymmetric, respectively. The origin of this will become clear when we discuss the examples.

[†] Allowing only a single mode per waveguide.

As the eigenvectors span a 2D vector space, all other $\boldsymbol{U}$ can be expressed by the superposition of these eigenvectors. The z-dependence, which an arbitrary excitation $\boldsymbol{U}$ exhibits, originates from the different propagation constants γ_k.

3.4.3. Examples

We use now the coupled mode equations to calculate the coupling of two waveguides. Here, we present two cases: a pair of identical waveguides and a pair of dissimilar waveguides. We use the former case to establish a principle understanding of how the coupling affects the wave propagation. The latter case will be of more practical use for the description of the experiments. As we already mentioned, we want to describe a system of waveguides consisting of a glass core with a liquid crystal core running parallel to it. So the waveguides are clearly different.

3.4.3.1. Identical fibers

In the case of identical fibers as shown in Fig. 3.11 , the propagation constants of the fundamental mode (and all other modes) are identical for both waveguides in isolation. Bringing both waveguides close to each other, induces a coupling of the modes which leads to a symmetric [upper left in Fig. 3.12 (a)] and an antisymmetric [upper left in Fig. 3.12 (a)] supermode. The coupling here is shown for the x-polarized HE_{11} mode, but it occurs for the y-polarized mode in the exact same fashion.

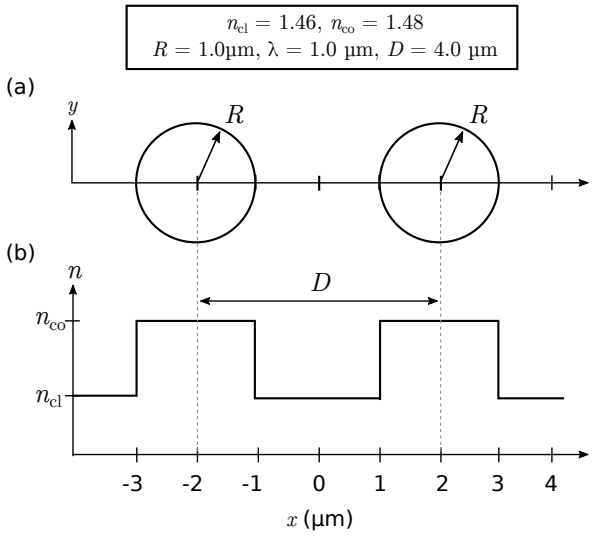

Figure 3.11. (a) Arrangement of two identical cores with radius R and center-center distance D. (b) Refractive index profile of the waveguide system with core refractive index n_{co} and cladding index n_{cl}. The physical parameters are summarized in the top box, where λ is the wavelength.

The coupling of the waveguides has an impact on the effective refractive index of the modes. While for symmetric mode the mode index n_{eff} increases, for the antisymmetric mode it decreases. This has practical implications which are shown in Fig. 3.12 (b). If we couple light only in the left waveguide at position $z = 0$

[Fig. 3.12 (c)], the optical power is confined to the left core as should be expected. But, after some propagation length $L_c = (\gamma_s - \gamma_a)^{-1}/2$, the power is transferred from the left to the right waveguide.

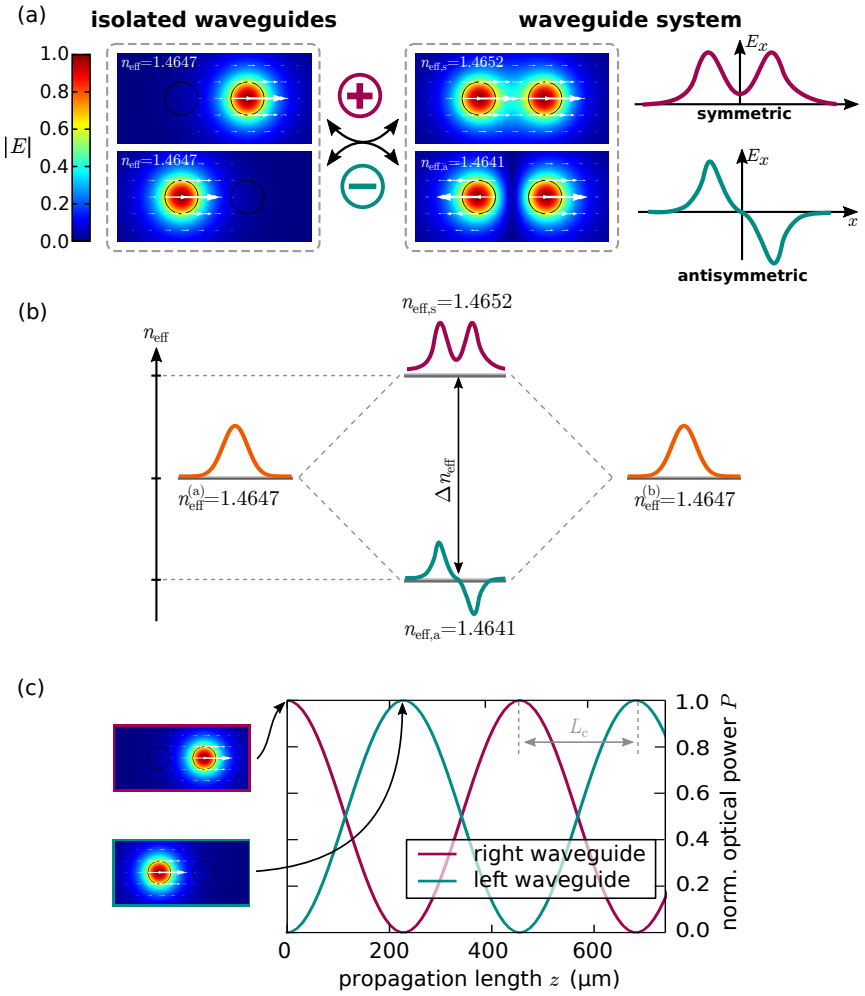

Figure 3.12. Example for the coupling between identical waveguides. (a) For the given values (cf. block), the coupled waveguide modes can be found by symmetric (top) and antisymmetric (bottom) combination of the modes of the single waveguide. (b) Splitting of the effective refractive indices n_{eff} due to the mode coupling: the even super mode has a higher n_{eff} compared to the odd mode. (c) Power transfer from one core to another if only one waveguide is excited. After the coupling length L_c, the power is transferred from one waveguide to the other.

The reason for this is that if light is coupled only to the right part of the structure, it does not have the form of the supermode of the waveguide system [cf. Fig. 3.12 (a)] thus it will change shape over the propagation length. But if we add the symmetric and the antisymmetric super modes together we arrive at the modal distribution shown in the upper left of Fig. 3.12 (c). This means we excite two supermodes in this way. Now, these two supermodes have different propagation constants γ_s and γ_a [Fig. 3.12 (b)], which means that after travelling to $z = L_c$ the two modes are out of phase by π. This leads to the beating of the optical power P from one waveguide

to another and is the basic principle of fiber couplers.

The beating length depends on the difference of the propagation constants. This difference, however, depends on the interaction between the two waveguides. If they get closer to each other the coupling increases. Also with longer wavelength, the coupling becomes stronger because the mode field diameters and therefore the interaction increase [cf. Sec. 3.3.3].

3.4.3.2. Dissimilar fibers

For dissimilar fibers [Fig. 3.13 (a)], the situation is very different. In Fig. 3.13 (b), we plot the effective refractive indices n_{eff} of a HE_{11} mode (red) in the left core and a HE_{21} (green) in the right core for different wavelengths. The modal pictures show the super modes of the combined waveguide structure at different wavelengths. We observe that for large differences in the effective refractive indices [points (I) and (III)], the coupling between the modes is week. The interaction is strongest, when the effective indices match at around 661 nm. We also observe at this point that the effective indices of the super modes do not cross. This is sometimes referred to as anti-crossing.

Figure 3.13 (c) shows the evolution of optical power for the different wavelengths marked in Fig. 3.13 (b). We observe that for the positions where the coupling is weak [i. e. (I) and (III)], the power transfer is rather low. Only when the coupling is strong [point (II)], a significant amount of power is transferred from the excited core (left) to the right core. We also observe that the coupling length for points (I) and (III) is small while it takes its maximum for the case (II).

When we introduced the hybrid modes in Sec. 3.3.3.2, we saw that there are always two degenerate versions of each HE or EH mode. Here, the degenerate modes of the HE_{11} and HE_{21} mode can be found by rotating the electric field by 90°. All possible permutations of the isolated guided modes are shown in Fig. 3.14 . All of the permutations will not couple efficiently. In Fig. 3.14 (a) the HE_{11} mode is x-polarized but the HE_{21} is almost completely y-polarized. But even the part of the HE_{21} which is x-polarized does not couple as the symmetry of the modes are incompatible. Also for the modes in Fig. 3.14 (b, c) the coupling vanishes due to the symmetry.

The discussion of these two exampes of coupled waveguides pointed out some key features of mode coupling: Modes only couple if their effective refractive indices match and their modal structure is compatible. If there is sufficient coupling and only one fiber is excited, power is transfered from one core to another periodically. The coupling strength influences the amount of power which is transferred.

The periodic power transfer, which we observed here, only appears if there are two modes interacting. If more modes are involved the exchange is in general not periodic [83].

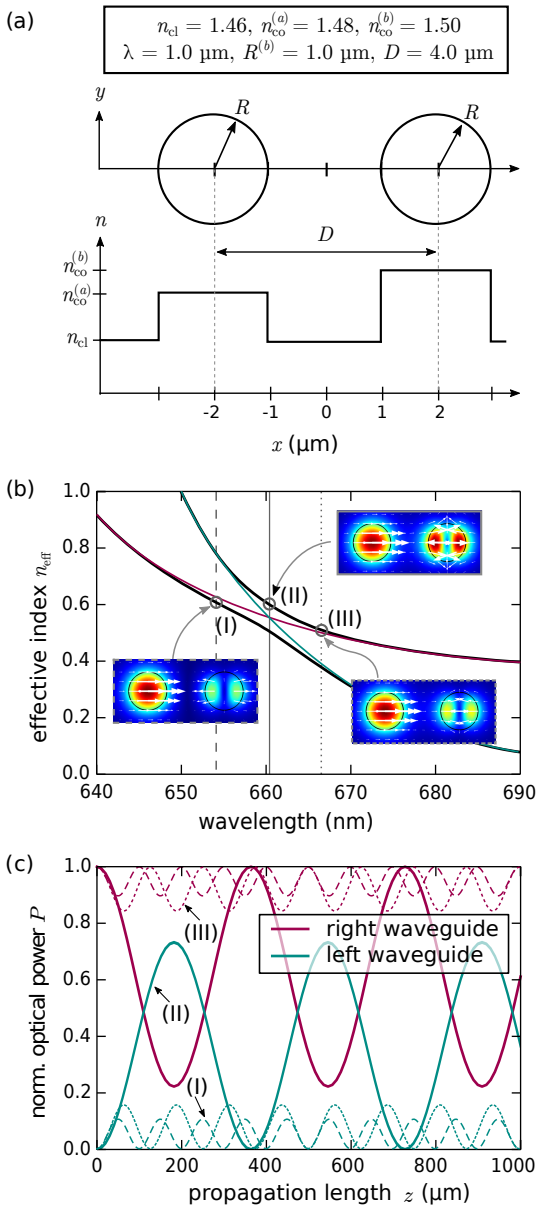

Figure 3.13. (a) Refractive index distribution of a structure consisting of dissimilar waveguides. Here only the core index $n_{\text{eff}}^{(a)}$ and $n_{\text{eff}}^{(b)}$ are different. The values are chosen to be $n_{\text{eff}}^{(a)} = 1.48$, $n_{\text{eff}}^{(b)} = 1.5$ and $n_{\text{cl}} = 1.46$. The core sizes are $R = 1\,\mu\text{m}$ for both, distance between the centers of the waveguides is $4\,\mu\text{m}$. (b) Effective refractive index vs. the wavelength. The cyan curve shows the n_{eff} HE_{11} of the isolated wave (b). The red curve gives the n_{eff} of the HE_{21} mode of the isolated waveguide (a). The black curves mark the n_{eff} of symmetric and antisymmetric supermodes. The insets show the simulated intensity distributions of the supermodes at the marked points (I) through (III). (c) Simulated power transfer between the waveguides when only the right waveguide is initially excited. The different curves correspond to the different positions marked in (b).

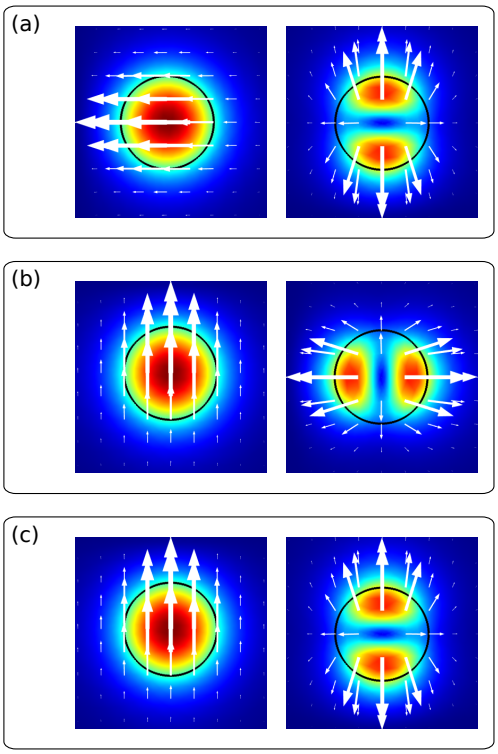

Figure 3.14. Remaining permutations of the HE_{11} and HE_{21} guided modes.

3.5. Photonic crystal fibers & photonic band gap fibers

With the advent of 2D and 3D photonic crystals [†] and their physical description in the late 1980's [15, 16] it was shown that periodically structured materials with a periodicity in the range of the wavelength could act as perfect reflectors of light. It took about ten years to produce the first optical fibers based on the idea of photonic crystals [94], which are consequently called photonic crystal fibers (PCFs).

Since then multiple designs of PCFs have been successfully developed, some of them are shown in Fig. 3.15. The fiber designs themselves can be very different, their common denominator is the periodic structure of the cladding. The prototype of a PCF is shown in Fig. 3.15 (a). It is made of silica, the cladding is formed by an periodic array of air holes. The light guiding core can be seen as a missing inclusion in this otherwise periodic cladding [95]. We will describe this type of fiber in a little more detail in the next section.

Based on the idea of photonic band gaps, PCFs with high index inclusions [37, 99] have been designed [Fig. 3.15 (b)]. These fibers are capable of confining light inside the low index core, which is not possible for step index fibers. Due to their guiding mechanism, these fibers are called photonic band gap fibers (PBGFs). If we compare the structures of the PCFs [Fig. 3.15 (a)] and PBGFs [Fig. 3.15 (b)], they look very similar. Actually a PCF can be turned into PBGF by filling the air inclusions with

[†] 1D photonic crystals (or Bragg stacks) have actually been known for a long time and also waveguides [92] and even optical fibers have been designed on this idea [93].

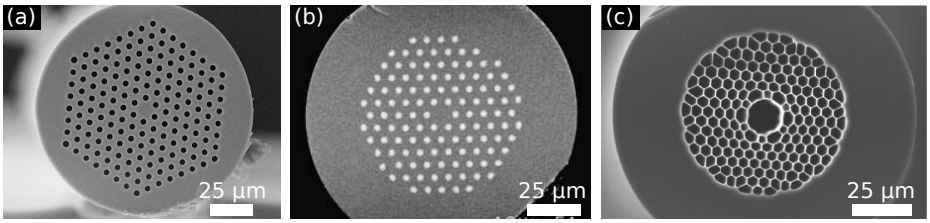

Figure 3.15. Scanning electron images of different types photonic crystal fibers (PCF): (a) Solid core PCF [96], (b) all-solid photonic crystal fiber (also referred to as all-solid photonic band gap fiber) [97] and (c) hollow core PCF [98].

a high index liquid [30, 100, 101]. In the upcoming experiments, we will use this method and fill liquid crystal as the filling material into a PCF. This procedure leaves us with a photonic band gap fiber. We will give a more detailed description of PBGFs in Sec. 3.5.2.

A third type of PCF are hollow core fibers [Fig. 3.15 (c)]. These fibers are capable of guiding light within air [102] or other gasses [103–105]. They are the structure of choice for non-linear optics within gasses as they combine high optical intensities due to their small diameters with a long interaction length. In general these fibers can also be filled with liquid crystals, but the high scattering losses (cf. Sec. 2.1.3) by using the LC as a core material make this application undesirable. Therefore, hollow core fibers will not be discussed any further.

3.5.1. Photonic crystal fibers

As mentioned above, the photonic crystal cladding is the key feature of photonic crystal fibers (Fig. 3.16). It confines the light inside the core. Photonic crystals are usually designed to have a lattice constant Λ [Fig. 3.16 (b)], which is comparable to the wavelength of light λ. This means that for optical applications Λ should be in the range of 0.4 µm to 1.0 µm for normal light incidence. However, in typical fibers the angle of incidence is rather high (measured with respect to the surface normal). In that case the transverse component of the wave vector (cf. Sec. 3.3.1) describes how the optical field varies and not the free space wavelength.

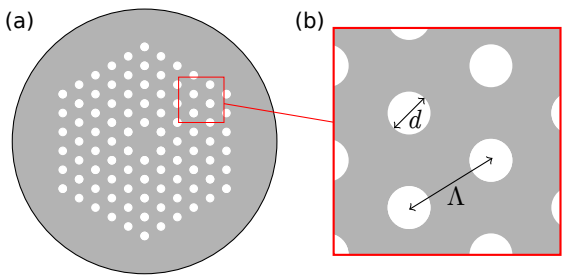

Figure 3.16. (a) Schematic of the cross section of a photonic crystal fiber consisting of a background material (grey) and air inclusions (white). (b) Enlargement of the photonic cladding with inclusion diameter d and lattice spacing Λ.

The transverse component, which we called β_t previously, is much smaller than the propagation constant β. By the relation $\lambda_t^{-1} \propto \beta_t$, the transverse wavelength λ_t is much larger than the vacuum wavelength λ. Thus, PCFs typically have lattice constants of a few microns. For example a LMA10 fiber (NKT Photonics [106]) has a lattice constant of $\Lambda = 6.525\,\mu m$ and an inclusion diameter of $d = 2.908\,\mu m$. This fact leads to one of the most interesting and most desired features of PCFs: the endlessly single mode behavior [94, 95].

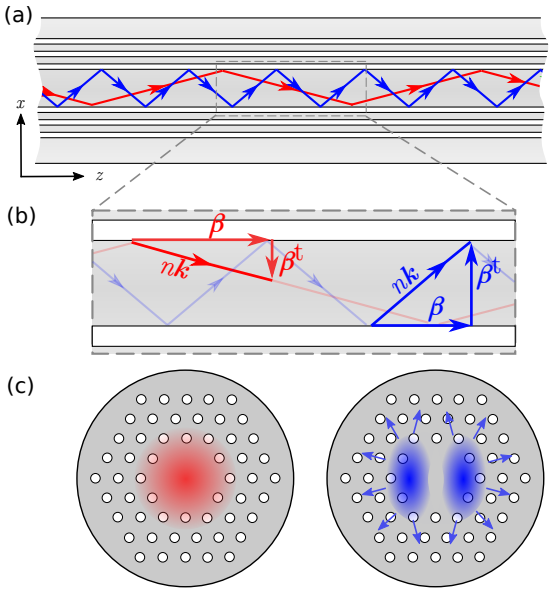

Figure 3.17. (a) Ray picture of the propagation of waveguide modes in a photonic crystal fiber: fundamental mode (red), higher order mode (blue). (b) Enlargement showing the propagation vector $\boldsymbol{\beta}$, the transverse propagation vector $\boldsymbol{\beta}_t$ and the wavevector $n\boldsymbol{k}$. (c) Fundamental mode (red) is confined to the core while a higher order mode (blue) escapes through the cladding.

When we discussed the step index fibers (Sec. 3.3), we remarked that step index fibers often support multiple modes and that the number of mode increases with the V-number Eq. (3.37). For a given fiber this usually means that the fiber becomes multimode if we go to shorter wavelengths. We also known that higher order modes have a larger β_t meaning a shorter transverse wavelength λ_t [Fig. 3.17 (a,b)]. This shorter transverse wavelength is not commensurate to the lattice parameter Λ. Hence, the mode is not confined by the periodic cladding and, consequently, is not guided [Fig. 3.17 (c)]. So, PCFs can be designed to support only a single mode, the HE_{11} mode [95].

If we compare the HE_{11} in a PCF [Fig. 3.18 (a)] and in a step index fiber (SIF) [Fig. 3.18 (b)], we observe a very similar pattern. At first, this seems as a surprising result, but, effectively, we only changed the type of reflector at the core-cladding interface. This is also the reason for calling the guiding mechanism in PCFs modified total internal reflection (mTIR) [107]. In fact, the PCF can be modeled as a step index fiber [95, 108, 109], which often gives accurate results. The similarities between

SIFs and PCFs also includes a broad band transmission, which is basically only limited due to the material absorption. As we will see, this is very different from photonic band gap fibers.

Besides the similarities in the modal profiles, there is a fundamental difference in the effective refractive indices n_{eff} of step index fibers (SIFs) and PCFs [Fig. 3.18 (c)]. As the PCF is made of a single background material (not including the air) with refractive index n_{B}, the light is guided in pure glass. This means that the guided mode has a effective refractive index $n_{\text{eff}}^{\text{PCF}} < n_{\text{B}}$. In a step index fiber, however, the background material is the cladding material and we had the relation $n_{\text{co}}^{\text{SIF}} > n_{\text{eff}}^{\text{SIF}} > n_{\text{cl}}^{\text{SIF}} = n_{\text{B}}$. So the lower bound for effective refractive index $n_{\text{eff}}^{\text{SIF}}$ in the step index fiber is the upper bound for the guided mode in a PCF. Or, to put it all together:

$$n_{\text{co}}^{\text{SIF}} > n_{\text{eff}}^{\text{SIF}} > n_{\text{cl}}^{\text{SIF}} = n_{\text{B}} > n_{\text{eff}}^{\text{PCF}} \tag{3.50}$$

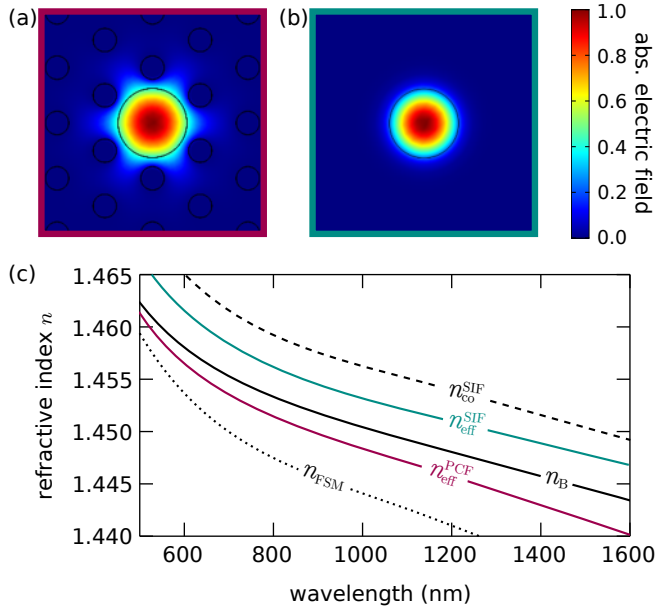

Figure 3.18. (a, b) Mode profiles of the fundamental modes in (a) a photonic crystal fiber (PCF) and (b) a step index fiber (SIF). (c) Effective refractive indices of the guided modes in PCF ($n_{\text{eff}}^{\text{PCF}}$) and SIF ($n_{\text{eff}}^{\text{SIF}}$). In the case of the SIF, the effective index $n_{\text{eff}}^{\text{SIF}}$ is bounded from above by the core material index $n_{\text{co}}^{\text{SIF}}$ (in our case Ge-doped silica) and from below by the index of the background material n_{B} (here silica). For the PCF, the core material is silica, which therefore forms the upper bound for $n_{\text{eff}}^{\text{PCF}}$. The lower bound is given by the index of the fundamental space filling mode n_{FSM}.

The lower bound in the SIF was set by the guiding mechanism (total internal reflection). So it makes sense, that the lower bound in a PCF is somehow set by the periodic cladding. It was determined to be the refractive index n_{FSM} of the fundamental space filling mode (FSM) [cf. Fig. 3.18 (c)]. We will not discuss the FSM further as it is not relevant for the remainder. Details can be found in [110–112].

The fact that the guided mode has a lower effective index than the background material ($n_{\text{eff}} < n_{\text{B}}$) is true for all the solid core photonic crystal fibers. This fact plays a major role in the discussion of the photonic band gap fibers, which follows next.

3.5.2. Photonic band gap fibers

Photonic band gap fibers (PBGFs) are photonic crystal fibers (PCFs) with high index inclusions. In this context 'high' means, that the refractive index of the inclusions, n_{incl}, is higher than the refractive index n_{B} of the background material. Even though PBGFs are a subcategory of PCFs, here we adopt the terminology that PCFs denote fibers with $n_{\text{incl}} < n_{\text{B}}$, and PBGFs fibers with $n_{\text{incl}} > n_{\text{B}}$.

The guidance in PBGFs is facilitated via photonic band gaps of the cladding structure, which gave these fibers their name. The easiest way to obtain such fibers is by filling high index material (liquids) in solid core PCF [Fig. 3.15], which we discussed above. Other methods are to draw all-solid photonic band gap fibers where the preform already contains all the wanted components. Here, the processing of cladding and background materials have to be compatible [37].

The guiding characteristics of a PBGF are different from a solid core PCF. While the PCF shows a broad band transmission very similar to a step index fiber (SIF), in which we always find the guided fundamental HE_{11} mode, the PBGF shows spectral transmission windows. In Fig. 3.19 (a) the refractive indices of the background material (here silica) and the filling material of a PBGF are shown [113]. Figure 3.19 (b) shows the corresponding experimental optical spectrum transmitted through this fiber. The transmission dips in the spectrum are labeled by orders of m. We will discuss the reason for this notation in Sec. 3.5.2.1.

In the following, we want to present an analytical and a numerical approach to understand the guiding in these fibers. The analytic approach is the so-called anti-resonant reflecting optical waveguide (ARROW) model. The ARROW model is concerned with locating the dips in transmission, which we observe in Fig. 3.19 (b). This is a very simple but (often) accurate approach. The numerical approach is based on the photonic cladding. Here, the cladding is considered as an infinite photonic crystal, for which the band gaps are determined. Then, only in the regions where band gaps exists, guidance is possible. We will also present results from the numerical eigenmode analysis, which give accurate results but not deeper physical understanding.

3.5.2.1. The Anti-Resonant Reflecting Optical Waveguide (ARROW) model

The ARROW model [114–116] offers a simple and accurate description of the positions of the regions of low transmission. Those are marked in Fig. 3.19 (b) by the dashed lines. The basic idea of the model is to assume that the fiber is in general an

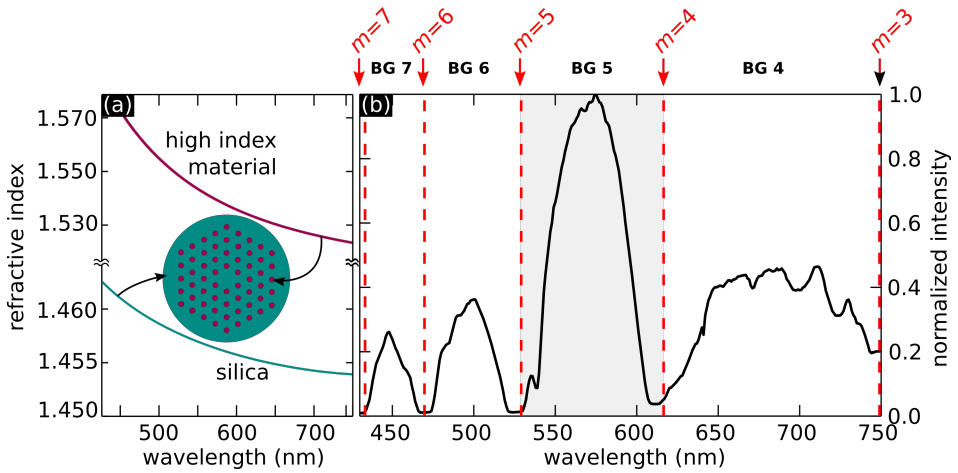

Figure 3.19. (a) Dispersion curve of the refractive indices of the silica background material (green) and the high index inclusion material (red) in a photonic band gap fiber (PBGF). (b) Transmission spectrum of the PBGF (black line) [113]. The ARROW wavelengths are marked by dashed red lines and are labeld with the corresponding resonance order m. The shaded region will be investigated further below.

optical waveguide and therefore able to guide light. Then, the cladding structure of the PBGF [cf. Fig. 3.19 (a)] is considered as an array of coupled identical waveguides. The inclusions are treated as the core of the corresponding waveguides, which is sensible as the refractive index of the inclusions is higher than the background (or cladding) material. Then the situation is very similar to the case of the coupled identical waveguides (Sec. 3.4.3.2), which we described with the coupled mode theory.

From Sec. 3.4 we know, that there is a power transfer from one waveguide to another if propagation constants of the modes are close to each other. As the core mode of the PBGF is guided in the background material with refractive index n_B, the propagation constant is $\beta_\mathrm{co} < n_\mathrm{B}k$, where k is the vacuum wave vector. As a consequence, the core mode cannot couple with guided modes of the inclusion waveguides because for all guided modes $n_\mathrm{B}k < \beta^i_\mathrm{incl} < n_\mathrm{incl}k$ holds. Here, n_incl denotes the refractive index of material inside the inclusions and β^i_incl is the propagation constant of the i-th inclusion mode.

The interaction of the core mode and the cladding consequently takes place by coupling of the guide core mode with cutoff modes or leaky modes of the cladding. We already described some properties of the leaky modes in Sec. 3.3.3.3. For example that for these modes the effective index is below the index of the background materials, which is exactly what we need. Now, for exactly locating where the effective index of the inclusion modes coincides with the effective index of the core mode, we would have to solve an eigenvalue equation similar to Eq. (3.31) for the inclusion and somehow guess the effective index of the core mode. This would be a very tedious work.

Fortunately, below the cutoff, the effective index of the inclusion modes falls off very steeply [117–119]. Thus, when we determine the wavelength of the cutoff we approximately know the position, where core and cladding couple. Due to the coupling, the light inside the core is transported through the cladding out of the structure. From this point of view, we can conclude that light is guided in wavelength regions where core and inclusion modes are in anti-resonance. Hence, the name anti-resonant reflecting optical waveguide (ARROW) model.

The cut-off conditions for fiber modes we already gave in Tab. 3.1. These cutoffs can be simplified by assuming isotropic materials, using the weak guidance approximation and applying the cosine approximation [115]. These approximations group together multiple cutoff modes which in the exact form are close to each other or degenerate. Therefore, it is more convenient to describe them by an resonance order m instead of the mode classifications we had in Sec. 3.3.3. The cut-off or resonance wavelengths are then given by

$$\lambda_m = \frac{4d}{2m+1}\left(n_{\mathrm{incl}}^2 - n_{\mathrm{B}}^2\right)^{1/2}. \tag{3.51}$$

In Fig. 3.19 (b) the resonance wavelengths are represented by vertical dashed red lines. They coincide almost perfectly with the regions of low transmissions. The reciprocal dependence on the resonance order m leads increased occurrences towards lower wavelengths [120, 121].

3.5.2.2. Computational approaches: Band gap and modal analysis

In this section we want to briefly describe the numerical methods used to determine the waveguiding properties of the photonic band gap fibers. The straight forward method is to apply finite element (FE) based eigenmode analysis to the PBGF. This will directly lead to the electromagnetic field distributions and the effective refractive indices of the waveguide modes. This approach can be applied to any kind of waveguide thus also to step index fibers and to coupled waveguides, which we discussed in Sec. 3.4. All finite element simulations in this work were carried out with Comsol 4.2 [122]. The eigenmode analysis is applied to the structure shown in Fig. 3.20 (a), which is only one fourth of the actual PBGF. But with the correct boundary conditions, this is sufficient as the structure itself as well as the fundamental mode have two two-fold symmetries [29, 123].

However, this numerical eigenmode analysis does only provide limited physical insight. To establish a clear physical picture, we perform a band gap analysis of the photonic crystal cladding [124]. As the cladding is assumed to be infinite in this analysis, only a unit cell has to be considered for the simulations. If all materials are isotropic, it is sufficient to simulate only one twelfth of the unit cell in k-space [Fig. 3.20 (b)] [113, 123]. There also exist analytic approximations for this problem [125], but we will only use the numerical approach.

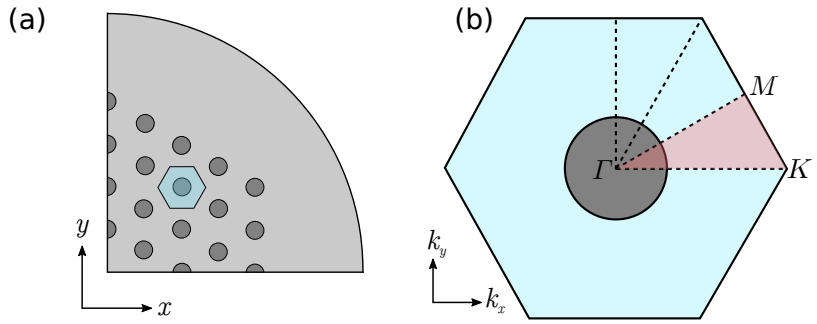

Figure 3.20. (a) One quarter of the cross section of a photonic band gap fiber. Blue hexagon marks the real space unit cell of the cladding structure. (b) Unit cell in reciprocal space of the hexagonal photonic cladding. One twelfth of the unit cell is shaded red with the symmetric points Γ, K and M.

For a qualitative picture, it is sufficient to focus only on a single transmission window or, equivalently, a single band gap. In Fig. 3.21 (a), we plot the results of the eigenmode analysis of the structure presented in Fig. 3.19 (a). We only consider the single band gap around 575 nm, it is marked red in Fig. 3.19 (b). We plot the simulated optical power confined to the core[†] (solid blue line) of the PBGF and as a reference the measured intensity (solid black line). Both curves are in very good agreement.

Figure 3.21 (b) shows the mode profiles at three different wavelengths marked in the spectrum Fig. 3.21 (a). At the edges of the transmission spectrum [points (i) and (iii)], there are strong interactions of the core and the inclusion modes. This will ultimately lead to loss of confinement of the core mode as predicted by the ARROW model. At point (ii), there is almost no interaction between core and cladding and the portion of optical power guided in the core reaches its maximum.

If we perform now a band gap analysis of the cladding structure to investigate where cladding modes do or do not exist, we arrive at diagram shown in Fig. 3.21 (c). Here the shaded regions indicate that there are solutions for Maxwell's equations that can propagate through the cladding. The darker the color the more cladding modes exist. In the white regions, no cladding modes could be found.

If we look now at the effective refractive index n_{eff} of the guided core mode [Fig. 3.21 (b), green solid line], which we obtained from the eigenmode analysis of the PBGF, we observe that it runs below the refractive index of silica, n_{silica}, as expected. The effective index is stopped at the short and the long wavelength edge by the cladding modes, which cross the silica line at about 535 nm and 615 nm, respectively. The cladding modes match the edges of the experimental and theoretical spectral transmission edges in Fig. 3.21 (a). At around 545 nm and 585 nm we also find two thin doublets, which cross the n_{eff} and the n_{silica}. They interact only weakly with the core mode as these bands originate from higher order cladding modes. These higher order modes exhibit multiple nodal planes in the electromagnetic

[†]The core radius in PBGFs (and PCFs) is typically defined as $\Lambda/\sqrt{3}$ [126].

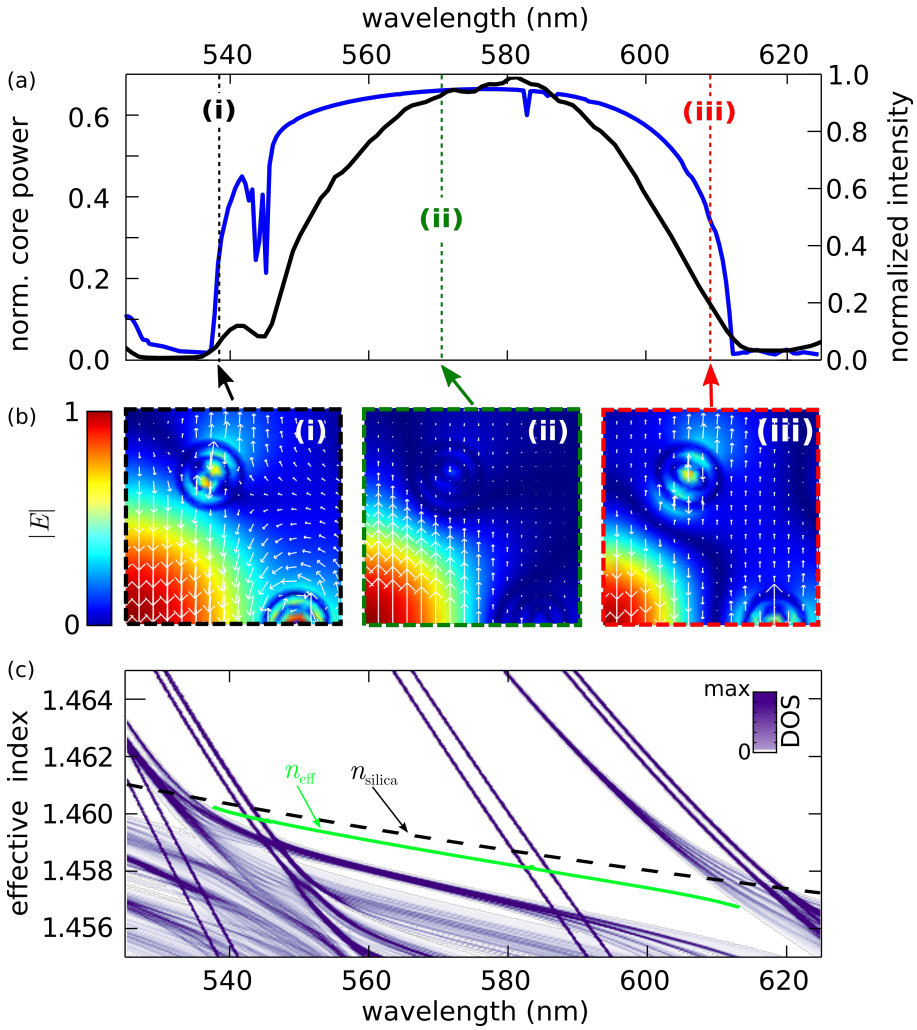

Figure 3.21. (a) Simulated absolute electric field within the core region (solid blue line) for the band gap in the shaded region in Fig. 3.19 (b), the experimentally measured intensity (black line) is plotted as a reference. The inset shows the absolute electric field of the fiber mode for the three marked wavelengths (i), (ii) and (iii). (d) Density of states (DOS, purple regions) for the same band gap as in (a). The effective refractive index n_{eff} (green) of the fundamental was obtained by the FEM simulations. The refractive index of silica (dashed black line) is plotted as a reference.

field distribution thus the overlap integral with the core mode, which has no nodes [Fig. 3.18 (a)], is rather small.

Beyond the edges of the transmission windows, the core mode is no longer confined and will leak out through the cladding. Or to put in coupled mode terms: The effective refractive index of the guided mode below 535 nm and above 615 nm couples to (a continuum of) cladding modes which have a matching effective index.

We also have seen previously in Sec. 3.4.3.2 that the coupling has influence on the effective refractive index of the guided mode (due to the formation of super modes). This is what we also observe here. At the edges, the of the transmission windows, the effective index is bend due to the interaction of the core mode with the cladding

modes. This bend will play a major role for the propagation of optical pulses, which we will discuss in the upcoming sections.

3.6. Dispersion properties of optical fibers

So far we discussed light guidance or light transmission in terms of continuous waves (CWs). For optical communications and other linear and non-linear optical processes optical pulses play a major role. In contrast to CW, an optical pulse consists of a multitude of optical frequencies. The shape of the optical pulse and the corresponding frequency components are Fourier transforms (FT) of each other. The result is a kind of uncertainty relation of the pulse width in time $\Delta\tau$ and the bandwidth $\Delta\omega$

$$\Delta\tau \times \Delta\omega \geq \text{const.} \tag{3.52}$$

The shorter the pulse duration $\Delta\tau$, the broader the frequency spectrum $\Delta\omega$. Figure 3.22 (a,b) shows the FT of a broad pulse in time domain, which has a narrow frequency spectrum (b). In contrast, the short pulse in time domain with only a few optical cycles [Fig. 3.22 (c)] has a relatively broad frequency spectrum [Fig. 3.22 (d)].

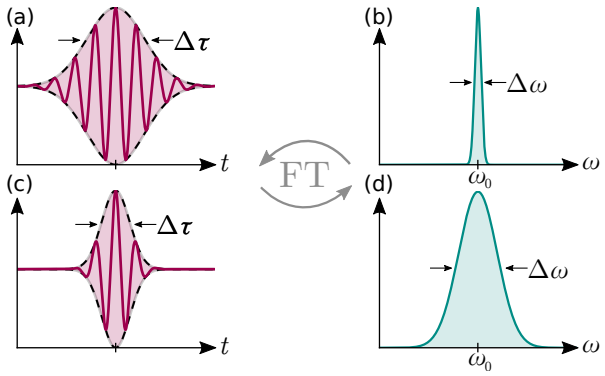

Figure 3.22. Schematics of optical pulses in the time domain (a, c) and their corresponding Fourier Transforms (FT) in frequency domain (b, d).

The bandwidth of optical pulses plays a major role in optical communication because the different components have different phase velocities

$$v_{\text{ph}}(\omega) = \frac{c_0}{n(\omega)}, \tag{3.53}$$

as the refractive index n is frequency dependent (c_0: speed of light in vacuum). This has two implications: First, the pulse envelope with a center wavelength of $\lambda_0 = \frac{2\pi}{\omega_0} c_0$ will not move with the phase velocity, but with a group velocity [71, p. 325]

$$v_{\text{g}} = c_0 \left(n - \lambda \frac{\partial n}{\partial \lambda} \right)^{-1}, \tag{3.54}$$

which is in fact different from the phase velocity for dispersive media. Closely connected to this property is the group delay τ

$$\tau = \frac{L}{v_\mathrm{g}}, \tag{3.55}$$

which describes the time τ it takes for a pulse to pass through a medium of length L at a group velocity of v_g. This represents a straight forward quantity to measure v_g for a given medium.

Secondly, the pulse will broaden while propagating in a medium because the different frequency components travel with different phase velocities. The amount of broadening is determined by the dispersion parameter D which is given by

$$D = -\frac{\lambda}{c_0}\frac{\partial^2 n}{\partial \lambda^2} = \frac{1}{L}\frac{\partial \tau}{\partial \lambda}. \tag{3.56}$$

Thus, measuring the group delay also provides a method to determine the dispersion by looking at the derivative of τ with respect to the wavelength.

The dispersion is usually given in units of $[D] = \mathrm{ps\,km^{-1}\,nm^{-1}}$, which describes the temporal pulse spreading in ps per propagation through a medium of length in km at a given wavelength in nm. The sign of the dispersion has a fundamental effect on the pulse spreading [cf. Fig. 3.23]. If the dispersion is negative ($D < 0$) the

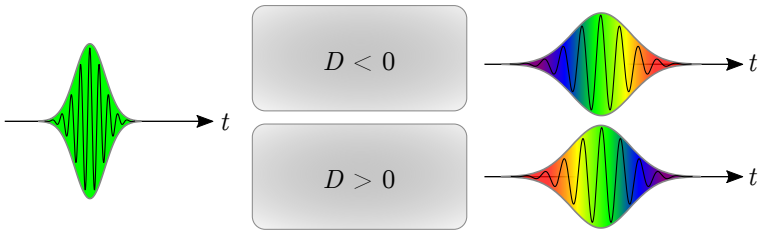

Figure 3.23. Scheme of pulse stretching in dispersive media. A negative dispersion ($D < 0$, normal dispersion regime) leads to the advancing longer wavelengths (shaded red within the pulse). This is reversed for positive dispersion ($D > 0$, anomalous dispersion regime). Here the shorter wavelengths (shaded blue) are advancing.

medium is said to be in the normal dispersion regime. In this regime the components of the optical pulse with longer wavelengths travel faster than the short wavelength components. The long wavelength components then travel in front of the pulse while the short wavelengths fall behind (top in Fig. 3.23). If the medium lies in the anomalous dispersion regime (i. e. $D > 0$), the effect is reversed and short wavelength components travel faster than the long wavelengths.

In any case, a dispersion with $D \neq 0$ leads to a (symmetric) pulse broadening. Wavelengths at which no broadening due to the dispersion is present, i. e. $D = 0$, are called zero dispersion wavelengths (ZDWs). In this case, higher order effects usually have to be taken into account, which may lead to asymmetric broadening. The dispersion we discussed so far is just the second order derivative in a Taylor series

around λ_0, thus the next order would involve derivates $(\partial^3 n/\partial\lambda^3)_{\lambda_0}$, $(\partial^4 n/\partial\lambda^4)_{\lambda_0}$, etc.

A standard material of which many optical fibers and photonic crystal fibers are made of is silica, which may us serve as an example. In Fig. 3.24, we plot the refractive index n (see Appendix A.1 for the refractive index formula), the group velocity v_g [Eq. (3.54)] and the dispersion D of this material [Eq. (3.56)].

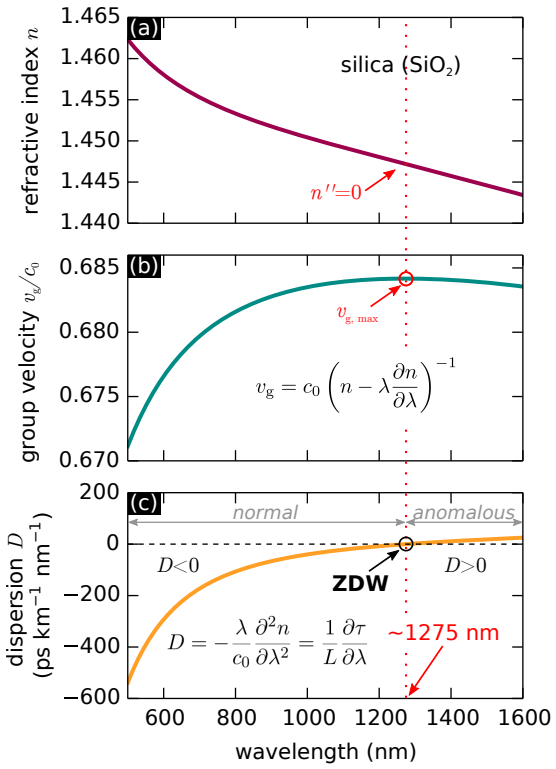

Figure 3.24. (a) Refractive index curve of silica. The inflection point with $\partial^2 n/\partial\lambda^2 = 0$ is marked. (b) Group velocity relative v_g to the speed of light c_0. (c) Dispersion in silica with the normal regime ($\lambda < 1275\,\text{nm}$) and the anomalous regime ($\lambda > 1275\,\text{nm}$).

The refractive index of silica shows a typical trend for materials in their transparent wavelength range: The refractive index n decreases continuously with increasing wavelength [Fig. 3.24 (a)], which means that the phase velocity v_{ph} [Eq. (3.53)] increases continuously.

If we look now at the group velocity [Fig. 3.24 (b)], at small wavelengths v_g is increases with increasing wavelength similar to the phase velocity. But at around $\sim 1275\,\text{nm}$, v_g reaches a maximum and then starts to decrease. Here, the effect of the derivative becomes apparent and pulses with larger wavelengths will move slower.

In the dispersion spectrum [Fig. 3.24 (c)], the point of maximum group velocity marks the zero dispersion wavelength ($D = 0$), which we discussed above in the context of pulse broadening. Below this point ($\lambda <$ ZDW) the material is in the normal dispersion regime with $D < 0$. Above this point $\lambda >$ ZDW, we enter the

anomalous dispersion regime, where $D > 0$.

In some applications, the ZDW of silica plays an important role. Optical communication systems operating at this point enable lowest pulse spreading and hence higher data rates. The wavelength range around the ZDW was the first one to be used for infra-red communication. It is therefore called the O-band, where 'O' stands for original [76]. A drawback of the O-band is that for silica the wavelength of lowest absorption is located at 1550 nm. The latter wavelength is therefore often favored and known as the C-band ('C' for conventional) [76].

In the following section, we will discuss non-linear optical effects, especially four wave mixing. We will see that for this process the dispersion properties of the wave guiding medium plays a significant role.

3.7. Four wave mixing

When we derived the wave equation from Maxwell's equations we assumed them to be linear in electric field. So the structure of the solutions do not change if we change the amplitude of the electric field. This case is typically referred to as the linear optical regime. This approximation relies on the model that the deflection of the electrons of the medium follows a harmonic potential. The linear dependence of the material becomes clear in the formulation of the electric displacement field:

$$\boldsymbol{D} = \epsilon_0 \epsilon_r \boldsymbol{E}$$

But this expression is only valid for small electric fields. At higher electric fields higher harmonics play a role which can lead to intensity dependent optical phenomena. This is the regime of non-linear optics. The displacement field has then to be expanded in a series of power of E

$$\boldsymbol{D} = \epsilon_0 \left[\left(1 + \chi^{(1)}\right) \cdot \boldsymbol{E} + \chi^{(2)} : \boldsymbol{EE} + \chi^{(3)} \vdots \boldsymbol{EEE} + \ldots \right] \tag{3.57}$$

where $\chi^{(\cdot)}$ are the (non-)linear susceptibilities. The terms with $\chi^{(2)}$ and higher are the non-linear contribution to the dielectric displacement. Most media are centrosymmetric, therefore $\chi^{(2)}$ vanishes. This is also true for silica, thus we will only consider nonlinear effects which involve the $\chi^{(3)}$ non-linearity.

Four wave mixing (FWM) is such a non-linear effect, which describes the interactions of four optical waves. The FWM process is of particular importance for optical waveguides because there the optical power is confined to a small area which leads to particularly high electric fields.

In optical fiber communication this poses a problem as due to this effect, different signals at different wavelengths can interact to generate optical signals at new wavelengths at the expense of optical power of the original signals. This is a parasitic

effect, which can limit the band width of optical data transmission systems.

Besides this negative example there are multiple useful applications of FWM. For example, it can be used to consciously convert optical signals from one wavelength to another [127, 128].

More recently, FWM has been used to create entangled photons [129–131]. Within that process, two pump photons are annihilated and two new photons are created. Reliable single photon sources are the building block of many quantum optical applications like quantum cryptography [132] and quantum communication [133].

When we discussed the propagation of optical pulses, we saw that the pulses travel with a group velocity v_g and that they can broaden due to the dispersion D. Both effects can be traced back to the wavelength dependence of the refractive index. The FWM process is also influenced by v_g and D as it always involves optical signals at different wavelengths. In the discussion of photonic band gap fibers [cf. Fig. 3.21 (c)], we already saw that the effective refractive index can exhibit a strong bending at the edges of the spectral transmission window. This will effect v_g and D in these fibers. We will show theoretically in Sec. 5.3.4 that the FWM process is possible in PBGFs and that it can even be electrically tuned by using liquid crystal infiltrated photonic crystal fibers.

In the following we discuss the basic concept of the FWM process and establish the connection to the waveguide dispersion in the case of continuous wave.

3.7.1. Phase matching condition

The four wave mixing (FWM) process is a third-order nonlinear effect which describes the interaction of four optical waves. For example two photons with frequency ω_p1 and ω_p2 can be annihilated within this process by simultaneous creation of two new photons: the signal with frequency ω_s and the idler with frequency ω_i [Fig. 3.25 (a)]. During the FWM process energy conservation,

$$\omega_\mathrm{p1} + \omega_\mathrm{p2} = \omega_\mathrm{s} + \omega_\mathrm{i}, \tag{3.58}$$

has to be fulfilled [Fig. 3.25 (b)].

Additional to the energy also momentum has to be conserved, i. e.

$$\boldsymbol{k}_\mathrm{p1} + \boldsymbol{k}_\mathrm{p2} - \boldsymbol{k}_\mathrm{s} - \boldsymbol{k}_\mathrm{i} = 0. \tag{3.59}$$

This condition is also known as phase matching. While the condition for the conservation of energy is obvious the momentum conservation is not.

As a matter of fact, we already investigated a situation where a similar condition has to be fulfilled. In Sec. 3.4 we discussed the interaction of modes in two adjacent waveguides. We arrived at the conclusion that the interaction between two specific fiber modes (at a fixed distance) is strongest if the propagation constants match,

which is also a phase matching condition. The same idea holds in the case of four wave mixing with the difference that four modes are involved and the interaction is mediated through the non-linearity [134] †. Similarly to the coupled mode equations, the FWM process can be described by a system of coupled differential equations [134, p. 371].

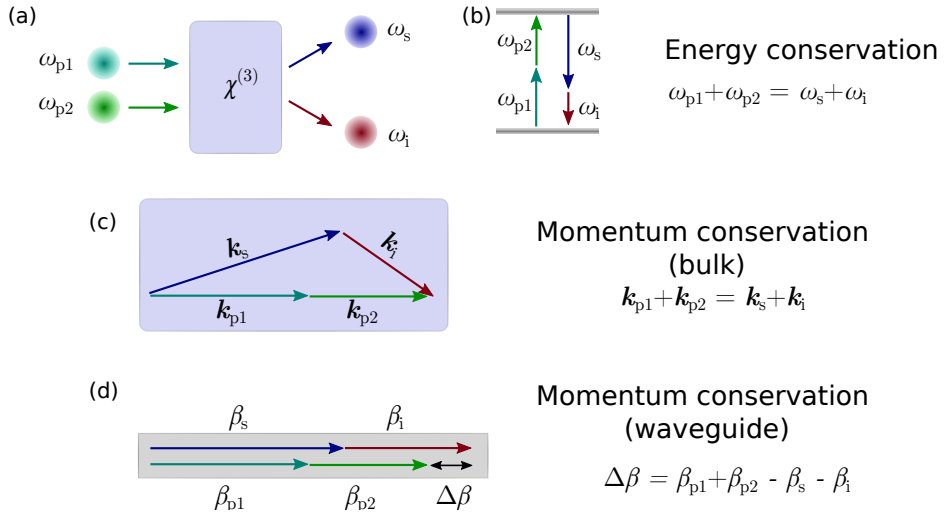

Figure 3.25. (a) Schematic of a four wave mixing (FWM) process in a non-linear $\chi^{(3)}$ bulk material: two parallel propagating photons ω_{p1} and ω_{p2} are annihilated while two photons ω_s and ω_i are created under an oblique angle. (b) Energy conservation and (c) momentum conservation which have to be fulfilled for the FWM process. (d) Phase matching in a waveguide with phase mismatch of $\Delta\beta$. Instead of the wavevectors k we use here the propagation constants β.

While the phase matching condition can be fulfilled in bulk materials by the emission of photons with a certain angle [Fig. 3.25 (a, c)], in an optical waveguide this is not possible because the direction of propagation is fixed along the waveguide axis. This limits the FWM process to certain wavelengths where the phase mismatch $\Delta\beta$ is close to zero. The phase mismatch is given by

$$\Delta\beta = \beta_{p1} + \beta_{p2} - \beta_s - \beta_i, \tag{3.60}$$

which closely resembles Eq. (3.59) and the propagation constants are labeled accordingly.

Figure 3.26 schematically displays the influence of the phase mismatch $\Delta\beta$. If $\Delta\beta \to 0$ we observe a strong increase in the generated signal/idler optical power with propagation distance. If, however, the phase mismatch is finite $|\beta| > 0$, we see an oscillating behavior with only a small amplitude. The oscillations are caused by constructive and destructive interference of the generated signal (or idler) as along the waveguide length, the phases for the generated signal vary due to the phase mismatch. The beat length is therefore inverse proportional to $\Delta\beta$.

†Similar to waveguide coupling, the four wave mixing process also involves overlap integrals.

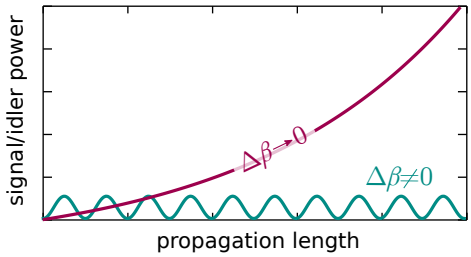

Figure 3.26. Schematic of generated signal/idler power due to a four wave mixing process for different phase mismatches $\Delta\beta \to 0$ and $\Delta\beta \neq 0$.

Again, we have seen a similar behavior for power coupling of dissimilar waveguides in Fig. 3.13 (c). There, the highest power transfer occurs if both modes are phase matched (or are in resonance). Away from the resonance we saw oscillations with small amplitudes. The coupling length L_c is inverse proportional to the difference in propagation constants $\Delta\beta$. For the signal generation in the (almost) phase matched case ($\Delta\beta \to 0$) the oscillations only become important at long propagation lengths.

3.7.2. Phase matching & waveguide dispersion

We have established so far that in order for the FWM process to proceed efficiently in optical waveguides the phase matching condition $\Delta\beta \to 0$ has to be fulfilled. To find wavelengths where this is true, one would need to know the effective refractive index of each of the involved modes to calculate the respective propagation constants. Unfortunately, this is not an easily measurable quantity.

A typical approach to circumvent this problem is the Taylor expansion of $\Delta\beta$ around the pump frequency. For simplicity we assume that both pump photons have the same frequencies, $\omega_{\mathrm{p1}} = \omega_{\mathrm{p2}} = \omega_{\mathrm{p}}$.[†] Then the expansion of Eq. (3.60) around ω_{p} yields

$$\Delta\beta = \frac{2}{2!}\frac{\partial^2\beta}{\partial\omega^2}(\Delta\omega)^2 + \frac{2}{4!}\frac{\partial^4\beta}{\partial\omega^4}(\Delta\omega)^4 + \frac{2}{6!}\frac{\partial^6\beta}{\partial\omega^6}(\Delta\omega)^6 + \ldots, \tag{3.61}$$

where $\Delta\omega = \frac{1}{2}(\omega_{\mathrm{s}} - \omega_{\mathrm{i}})$. The odd terms in this expansion cancel because the generated signal and idler are equally spaced (in frequency) from the pump. Equation (3.61) shows that phase matching is fulfilled to second order if $\frac{\partial^2\beta}{\partial\omega^2}$ is zero. It turns out that the first derivative of β is the group velocity that we already know [cf. Eq. (3.54)]:

$$\frac{\partial\beta}{\partial\omega} = \frac{1}{v_{\mathrm{g}}}. \tag{3.62}$$

The second derivative is therefore called the group velocity dispersion

$$\mathrm{GVD} = \frac{\partial^2\beta}{\partial\omega^2} = \frac{\partial}{\partial\omega}\frac{1}{v_{\mathrm{g}}}, \tag{3.63}$$

[†]This is called a degenerate pump configuration.

which is related to the dispersion D we introduced previously [cf. Eq. (3.56)] by

$$D = -\frac{2\pi c}{\lambda^2}\mathrm{GVD}. \tag{3.64}$$

Equation (3.64) explains why the dispersion of a waveguide plays a huge role for the four wave mixing process. Because at the zero dispersion wavelengths (ZDW) also the GVD is zero. Thus ZDWs are usually chosen for the FWM process. But this also poses a limit to this process as most materials and the waveguides made from them have only a single ZDW. We already presented silica as an example with a ZDW at around 1275 nm.

We will see later in Sec. 5.3.3 that in liquid crystal filled photonic crystal fibers (and in photonic band gap fibers) multiple ZDWs are present. We will finally use this fact in Sec. 5.3.4 to show that this enables phase matching in the visible wavelength range which is tunable by electrically addressing the liquid crystal.

Part II.

Experimental results

Chapter 4

Microstructured optical fibers

4.1. Liquid crystal filled microstructured optical fibers

In this chapter, we will study the interaction of light guided in an optical fiber with a glass core and, running parallel to it, a hollow inclusion which is filled with liquid crystal (Fig. 4.1). This then forms a coupled waveguide system, which resembles the coupled waveguides we discussed in Sec. 3.4.3.2.

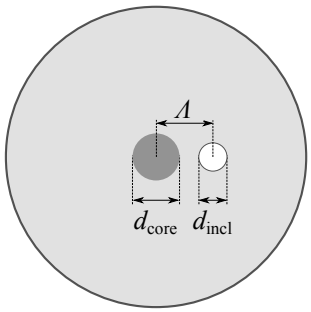

Figure 4.1. Schematic cross-section of a micro-structured optical fiber with a glass core (diameter d_{co}) and a hollow inclusion (diameter d_{incl}). The glass core and the cladding are concentric. The inclusion is displaced by Λ measured from center to center.

Structures similar to the one shown in Fig. 4.1 have already been used to determine the refractive index of liquids infiltrated into the inclusions [21] or to study surface plasmon resonances spiraling around gold infiltrated inclusions [22]. In both cases, the coupling between core and inclusion leads to losses due to scattering or absorption.

The infiltration of the inclusions with liquid crystals (LCs) has the benefit of being able to electrically address the LC. This can then be used to control the coupling of the waveguides.

The physical description of this type of waveguides involves two mechanisms. First, the interaction of the waveguides described by the coupled mode theory

Sec. 3.4. And secondly, the scattering of light inside the LC inclusion due to the thermal fluctuations of the liquid crystal Sec. 2.1.3.

4.2. Experimental details

4.2.1. Types of microstructured optical fibers

Figure 4.2 (a) shows schematically a microstructured optical fiber and Fig. 4.2 (b) displays an optical micrograph of the real structure in reflection. The fibers employed in this work were fabricated by Markus Schmidt in the group of Philip Russell at the Max Planck Institute for the Science of Light in Erlangen. The core of the structure is made from silica doped with 16 % germanium (see Appendix A.1 for Sellmeier coefficients). The doping leads to a higher refractive index of the core compared to cladding, which is made from pure silica [Fig. 4.2 (c)]. This facilitates the guidance via total internal reflection.

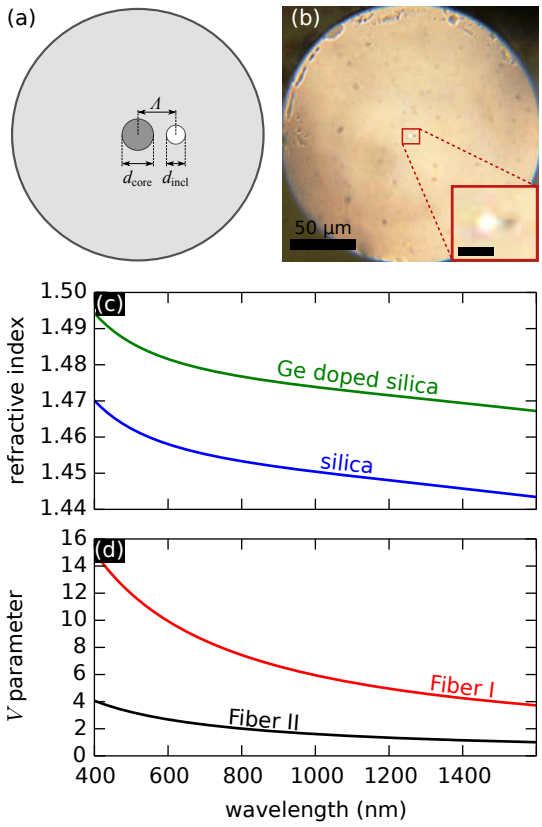

Figure 4.2. (a) Schematic cross-section of a micro-structured optical fiber with a glass core and a hollow inclusion. (b) Optical micrograph in reflection of a microstructured optical fiber. The inset shows the core (bright) and the empty inclusion (dark), the scalebar is 5 µm. The cladding has an outer diameter of 200 µm. (c) Refractive indices of silica and silica doped with 16 % germanium. (d) V-parameter of the core waveguide (in isolation) of fibers I and II.

We investigate two different types of optical fibers. Their geometrical specifications are listed in Tab. 4.1. Fiber I has a small core (1.3 µm) and is used for the

transmission of visible light. The small core is only theoretically capable of guiding in the infrared (>800 nm) because of the low level of confinement which will lead to high losses. For infrared (IR) radiation, fibers of type II are more suitable. In comparison with fiber I the core is more than three-times larger in fiber II thereby providing good confinement in the IR. The diameters of the inclusions and the center-center-distances are comparable.

Table 4.1. Parameters of the fibers of type I and II: core diameter d_{core}, inclusion diamater d_{incl} and center-center-distance Λ of core and inclusion.

fiber	d_{core} (µm)	d_{incl}(µm)	Λ (µm)
I	1.0	1.3	3.2
II	3.7	1.7	4.3

According to their V parameters ($V \approx 3$ for fiber I at 500 nm, $V \approx 6$ for fiber II at 1000 nm) both fibers support a few modes [Fig. 4.2 (d)]. For the experiments, we neglect higher order modes and assume the glass waveguide only to transmit the fundamental mode.

4.2.2. Liquid crystals

In the experiments, we use three different liquid crystals. For fiber I in the visible regime, we employ liquid crystal mixtures MLC2103 and BL036. MLC2103 has a low refractive index and a low birefringence compared to E7 and BL036. The latter two are rather similar, BL036 has a slightly larger birefringence. Figure 4.3 shows the oridnary and extraordinary refractive indices of the three LC mixtures. All liquid crystals mixtures used in this chapters have positive dielectric anisotropy, i. e. $\Delta\epsilon > 0$. Consequently they align parallel to an external electric field. For the different LCs, the dielectric anisotropy at 20 °C is as follow: $\Delta\epsilon(\text{E7}) = 13.8$ [135], and $\Delta\epsilon(\text{BL036}) = 16.4$ [135]. For MLC2103 no values are available.

4.2.3. Inclusion surface treatment & filling procedure

In order to minimize defects in the liquid crystal we induce degenerate planar anchoring on the inner surface of the inclusions. This is done by infiltrating the inclusion with a solution of the compound (3-glycidyloxypropyl)trimethoxysilane (Glymo [136],1 wt% in a 50/50 mixture of water and isopropanol). For this purpose, a few centimeter long section of the microstructured fiber is put through a septum into the solution [Fig. 4.4 (a)]. Capillary forces then draw the liquid into the inclusion. The process is assisted by evacuating the chamber, which holds the vessel with the liquid.

The solution is extracted from the inclusion by applying a nitrogen stream of approximately 3 bar [Fig. 4.4 (b)]. This pushes the liquid out of the inclusion and

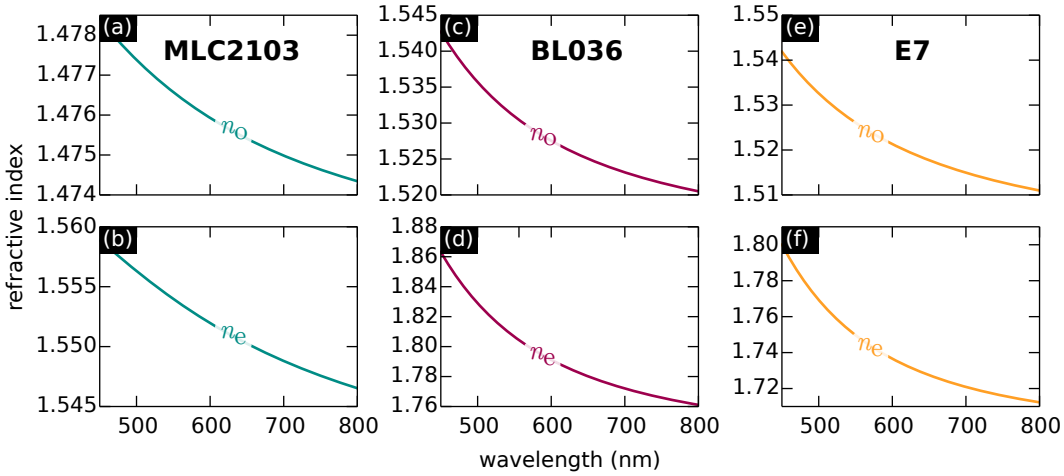

Figure 4.3. Ordinary and extraordinary refractive indices of the liquid crystals MLC2103 (a, b), BL036 (c, d) and E7 (e, f). Details on the measurements of the refractive indices can be found in Appendix A.2.

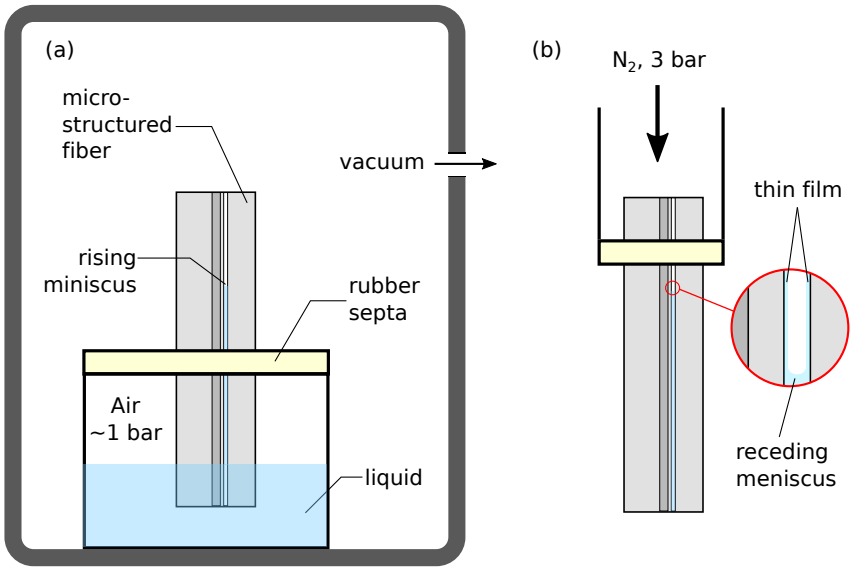

Figure 4.4. Schematic representation of the coating process of the inclusions walls by solution deposition. (a) One end of the fiber is dipped into the liquid, which contains the functionalizing agent. The liquid enters the capillary via capillary forces. The process is assisted by vacuum on the other fiber end. (b) The liquid is extracted from the capillary by applying a high pressure nitrogen stream (up to 3 bar). This leaves behind a thin film of the liquid on the capillary wall.

leaves behind a thin film on the inclusion walls. The treated fibers are dried at 110 °C for 24 h.

The coated fibres are filled with the respective liquid crystal by heating the LC into the isotropic state and using again a pressure gradient of 1 bar. The samples are then cooled down slowly to room temperature over a period of several hours. The alignment is checked by means of polarizing microscopy: If the fiber axis is parallel to the polarizer [Fig. 4.5 (a)], there is no change in the state of polarization

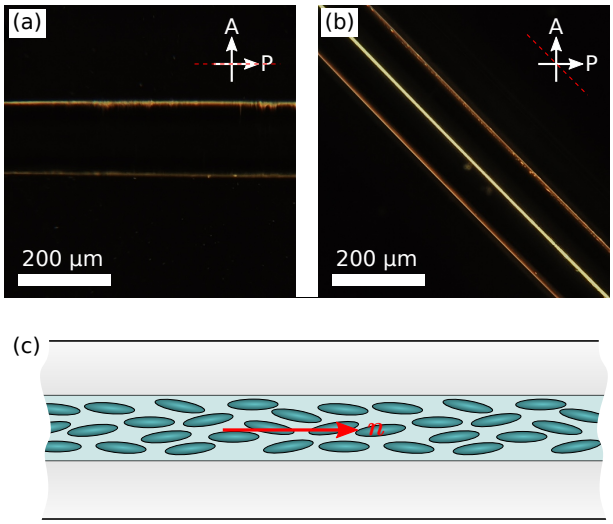

Figure 4.5. Polarizing optical microscope images of a fiber with degenerate planar anchoring filled with a liquid crystal. (a) The fiber axis is parallel to the polarizer. (b) The fiber is in an 45° angle with respect to the polarizer and analyzer. (c) Schematic of the uniform axial alignment of the liquid crystal (indicated by the director $\boldsymbol{n}$) inside the inclusion.

and no light is transmitted after the polarizer. If the fiber axis assumes an angle of 45 degree with respect to polarizer, the polarization state changes and light passes through the analyzer [Fig. 4.5 (b)]. Consquently, the degenerate planar alignment introduced with glymo is sufficient for a homogeneous axial alignment of the liquid crystal [cf. Fig. 4.5 (c)].

4.2.4. Measurement & Characterization

4.2.4.1. Transmission measurements

The setup for measuring the transmission through the prepared fibers is shown in Fig. 4.6 . A broad band light source (Xe-arc lamp) in combination with a grating monochromator (LOT Oriel λ-3009) is used to couple light into a single mode fiber (SMF) which is butt-coupled to the sample. The light emitted from the sample is collimated, send through a polarizer and detected by a photomultiplier tube (PMT) in the case of visible light or with a InGaAs photo diode (FEMTO FWPR-20-IN) in the case of IR radiation. To reduce the noise, an optical chopper and a lock-in amplifier (Stanford Research Systems S830) are used.

4.2.4.2. Attenuation measurements

An important value in the characterization of optical waveguides is the attenuation. The attenuation in general describes the loss in transmitted optical power per unit length. The loss contains multiple loss mechanisms like confinement loss in optical waveguides, material loss or scattering. In our case, scattering is the main source of

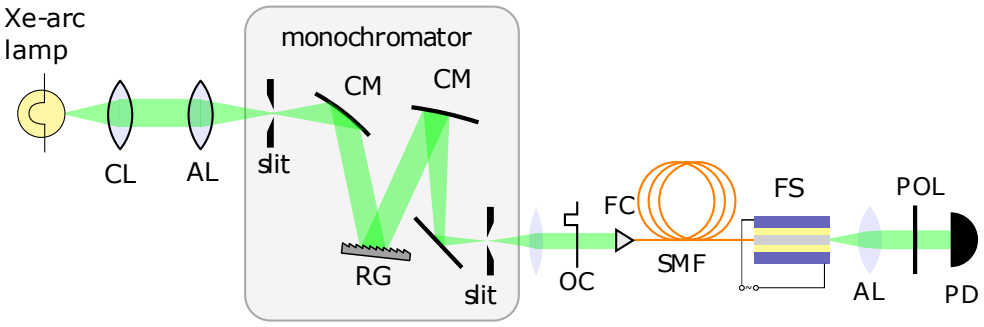

Figure 4.6. Schematic of the setup used to measure attenuation and the electrooptics. Light from a Xe-arc lamp is collimated by a lens (CL) then focused on the slit of a monochromator by an aspheric lense (AL). The light is collimated by a concave mirror (CM) and directed on a reflective grating (RG). The filtered light is then coupled into a single mode fiber (SMF) by a fiber coupler (FC). The signal is chopped by an optical chopper (OC), which is connected to a lock-in amplifier, to filter the noise. The SMF is spliced to the fiber sample (FS). The transmitted light is collimated and the detected by a photo diode (PD).

loss in the prepared fiber samples. In general, the optical power decays exponentially, thus it is described by

$$\log\left(\frac{P(z)}{P_0}\right) = -az, \tag{4.1}$$

where P_0 is the optical power at $z = 0$ (coupling losses are neglected), P_z is the optical power of the light after traveling a distance z and a is the attenuation. Typically a is given in units of $[\mathrm{dB\,cm^{-1}}]$.

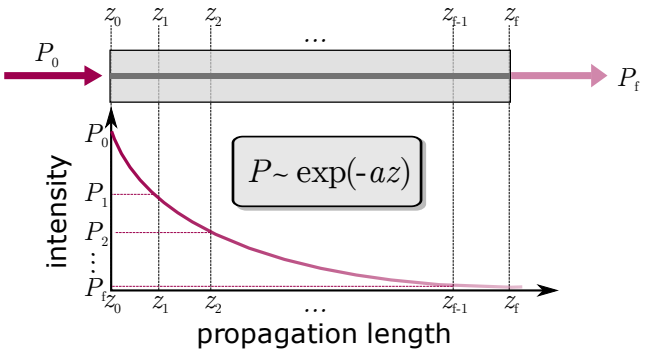

Figure 4.7. Principle of the cutback technique: light with optical power P_0 at position z_0 is coupled into the fiber. The optical power is attenuated exponentially over the propagation length. By cutting back the fiber, the optical power at different points can be evaluated.

Multiple techniques have been developed to measure the attenuation of optical waveguides. For our purposes, the cut-back technique is the most reliable and works for very short fibers of only a few centimeters. A schematic representation of this method is shown in Fig. 4.7 . Light is coupled into a waveguide and the optical power P_f is measured at a propagation distance $z = z_\mathrm{f} = L$, where L is the initial length of the waveguide. Then, by cutting the waveguide, the optical power $P_{\mathrm{f}-1}$ at an earlier position $z_{\mathrm{f}-1}$ can be detected. This procedure is repeated to gather enough

data points. It should be avoided to investigate a sample with less than 1 cm length, as there might be stray light from coupling losses. The attenuation can then be obtained by fitting Eq. (4.1) to the data points.

4.2.4.3. Electrooptics

To be able to apply a voltage and electrically induce changes in the liquid crystal, the prepared microstructured fiber is sandwiched between conducting Indium-Tin-Oxide (ITO) covered glass plates (Fig. 4.8). The components are fixed with an UV-curable optical adhesive (Norland NOA 65). Due to the geometry, the electric field is only pointing in the y direction, i. e. $\boldsymbol{E} = E\boldsymbol{e}_y$.

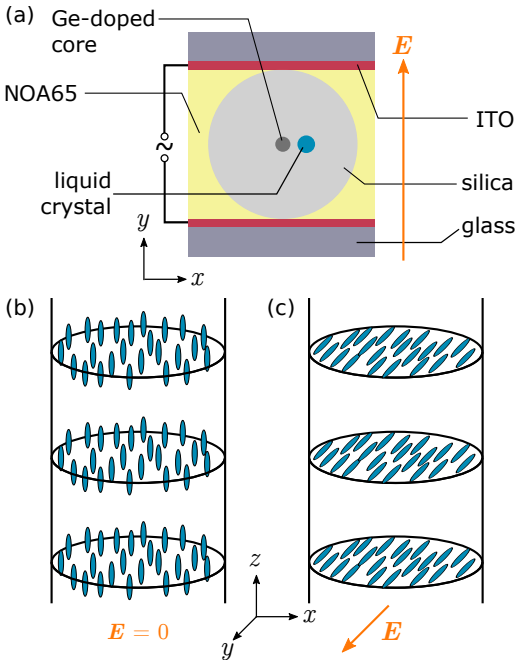

Figure 4.8. (a) Schematic of the fiber sample sandwiched between two conducting Indium-Tin-Oxide (ITO) electrodes. (b, c) Director configuration inside the inclusion for (b) $\boldsymbol{E} = 0$ and for (c) $|\boldsymbol{E}| \gg 0$.

We quantify the change in optical power under an electric field by the relative power RP, which is defined by

$$\text{relative power} = \log\left(\frac{P_0}{P_V}\right)\frac{1}{L}. \tag{4.2}$$

Here, P_0 and P_V denote the optical power measured at 0 V and at a voltage V, respectively; the quantity is divided by the sample length L. Similar to the attenuation, values of the relative power are given in units of $[\mathrm{dB\,cm^{-1}}]$.

The application of the electric field will reorient the LC molecules along the direction of the field. This reorientation will have a strong effect on the polarizing properties of the fiber as the refractive index distribution will be different for x- and

y-direction [Fig. 4.8 (b,c)]. Then, the ratio of the intensities in x- and y-direction become interesting and can be quantified by the extinction

$$\text{extinction} = \log\left(\frac{P_x}{P_y}\right)\frac{1}{L}, \tag{4.3}$$

where P_x and P_y are the optical powers measured for x- and y-polarized light.

4.3. Results & Discussion

In the following, we will discuss three examples for the transmission through these fibers and will discuss their parameters according to the properties introduced above. All measurements we describe here consider only light launched into the solid glass core. We do not couple light into the liquid crystal inclusion.

4.3.1. Fiber I filled with MLC2103

4.3.1.1. Attenuation spectrum

First, we focus on the visible regime, for which we use fiber I filled with MLC2103. The results for the attenuation measured via the cut-back technique are shown in Fig. 4.9 (a) (red line). We can identify three different regions which are located around the green marked wavelengths [①, ② and ③]. Around wavelength ① ($\sim 450\,\text{nm}$) we detect low attenuation close to zero, indicating that there is little or no interaction of the core and the inclusion mode.

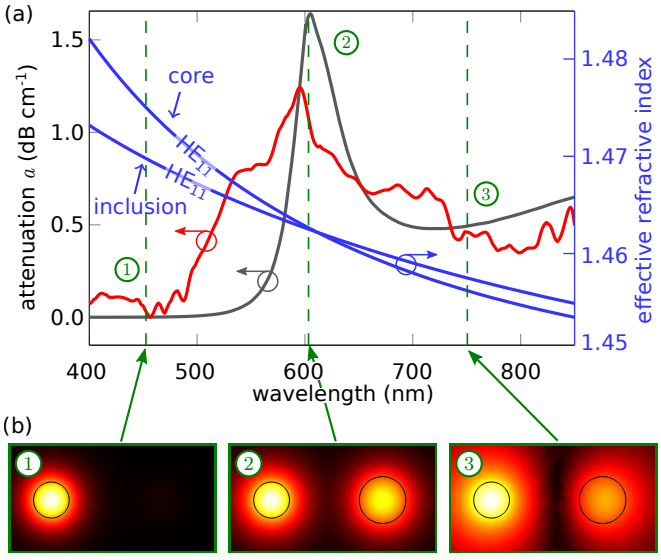

Figure 4.9. (a) Measured attenuation in a fiber of type I filled with MLC2103 (red line) and the calculated attenuation (gray line) from coupled mode theory. Calculated effective refractive indices of the core and inclusion HE_{11} mode (blue line). (b) Norms of the electric field distributions of supermodes calculated at three wavelengths ① through ③ marked in (a).

The maximum of attenuation can be found around the wavelength ② [$\sim 600\,\mathrm{nm}$] with $1.3\,\mathrm{dB\,cm^{-1}}$. Here, a strong coupling occurs between core and inclusion modes, which leads to a power transfer from core to the inclusion. The light in the inclusion is scattered away, which ultimately leads to the high loss in this region. At longer wavelengths [③, $\sim 750\,\mathrm{nm}$], the losses are reduced again but do not go to zero. This indicates that there is still some residual coupling. The measured attenuation does not depend on the polarization, from which we can conclude that the involved modes possess a rotational symmetry.

By calculating the properties of the core and the inclusion waveguides in isolation [cf. Sec. 3.3], we achieve some insight, which modes are involved. For the core, we a priori excluded all modes except the fundamental mode. The effective refractive index of this mode (blue line) is plotted in Fig. 4.9 (a). The low refractive index of MLC2103 in general only permits the appearance of a few modes. The coupled mode calculations show, that the interacting inclusion mode is also the HE_{11} mode. This explains the observation that the attenuation is polarization independent. The effective index is plotted in Fig. 4.9 (a).

At short wavelengths (400 nm to 500 nm), the effective refractive indices of the interacting modes start out far away from each other. They gradually become closer with increasing wavelength. They cross just above 600 nm and then separate again. The separation above 600 nm is small compared to lower wavelengths.

With the coupled mode theory [cf. Sec. 3.4] we are able to calculate the attenuation [grey solid line in Fig. 4.9 (a)]. The results closely resemble the experiment. The peak is located at the crossing of the effective indices. Beyond the maximum attenuation, the attenuation still is high because the indices are still close to each other. The calculated attenuation even increases with higher wavelengths which is a result of the increase mode field diamater (cf. Sec. 3.3.3.4) and therefore furthers the interaction. The supermodes of the coupled waveguide structure [Fig. 4.9 (b)] obtained from the FEM simulation further confirm the different coupling regime ① through ③.

4.3.1.2. Electrooptics

The application of an external voltage leads to an electric field pointing in y-direction (cf. Fig. 4.8). If the field exceeds a threshold value ($\approx 1\,\mathrm{V\,\mu m^{-1}}$) the LC molecules will be forced to reorient along the electric field (similar to what we have seen for the Fréedericksz Transition in Sec. 2.3). This fundamentally changes the refractive index distribution inside the inclusion and thus the waveguide modes. Consequently, the coupling between core and inclusion is a affected and the transmission changes. All voltages discussed here are sine voltages at 1 kHz and the voltage values are the root mean square. The distance between the capacitor plates [cf. Fig. 4.8 a] is given by the fiber diameter, which is 200 µm.

In Fig. 4.10 , the relative power is plotted for x- and y-polarized light for a voltage

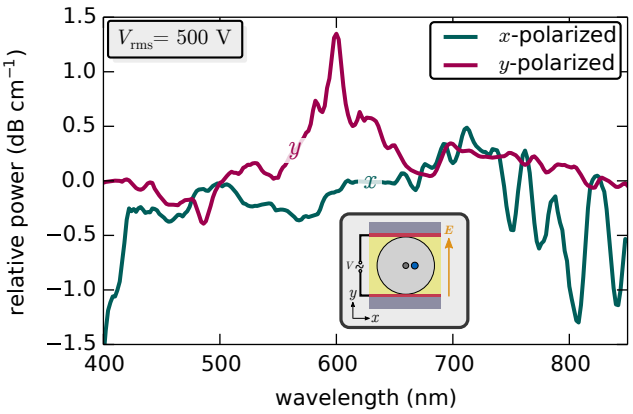

Figure 4.10. Relative power of fiber type I filled with MLC2103 for x- and y-polarized light at 500 V. The inset shows the geometry of the sample. The electric field is parallel to the y-direction.

of 500 V. We observe a significant difference under an applied voltage. The x-polarized optical electric field, which is perpendicular to the quasi-static external electric field, mainly exhibits a decrease in optical power, especially in the regions above 700 nm. In contrast, the y-polarized light gains optical power, mainly around 600 nm. This coincides with the wavelength of maximum attenuation in the field off state [cf. Fig. 4.9 (a)].

These strong differences in polarization can be explained by the reorientation of the liquid crystal. In the field-off state, the molecules are oriented parallel to the fiber axis [Fig. 4.8 (b)], the liquid crystal resembles a uniaxial waveguide with an optical axis parallel to the fiber axis. The transverse refractive indices are identical, i. e. $n_x = n_y = n_o$. Due to the electric field, the LC molecules reorient along the external field, which changes the refractive index distribution.

For very large field strength ($E_y \gg 1\,\mathrm{V\,\mu m^{-1}}$), all molecules are oriented along the electric field [Fig. 4.8 (c)] and the refractive indices would be $n_x = n_z = n_\mathrm{o}$ and $n_y = n_\mathrm{e}$. In this limit, the electric switching has a dominant effect on y-polarized light. The coupling of the core mode with the inclusion changes significantly. The y-polarized fundamental inclusion mode shifts due to the increased refractive index in that direction. Consequently, the coupling between core and inclusion will diminish and consequently the transmitted power will increase.

In this limit, the x-polarized light should only be marginally affected. However, the field strength is not infinite and together with the boundary conditions this will lead to a reorientation of the director, which is not confined to the yz-plane. Therefore, effects on the x-polarized inclusion modes are to be expected, which lead to a coupling than in the field-off state. A final important fact is that higher order modes are not purely x- or y-polarized (e. g. TE, TM modes). Those are then strongly influenced by the change in n_y as well, and may, at the same time, couple with the x-polarized core mode due to the mixed polarization.

A more quantitative modeling of the problem would involve a numerical modeling

of the exact director field under an electric field. These kind of simulations are rather involved and the parameter space is large (elastic constants K_{11}, K_{22}, K_{33} and K_{24} of the LC, anchoring strengths W_θ and W_ϕ on the surface, ...). Further, the system is very sensitive to deviations of the refractive index, it is therefore doubtful that the modeling without exact knowledge of all parameters yields more than a qualitative picture. For following combinations of fiber types and liquid crystals, we will therefore focus on a qualitative explanation of the effects which occur by applying an electric field.

4.3.2. Fiber I filled with BL036

We now change the system slightly by using the liquid crystal BL036, which has larger refractive indices ($n_o = 1.528$, $n_e = 1.794$ at 20 °C and 589 nm wavelength). The increased index is expected to lead to the appearance of a multitude of higher order modes, which we did not encounter in the previous example.

4.3.2.1. Attenuation spectrum

In Fig. 4.11 (a) we plot the measured attenuation for x-polarized (top) and y-polarized light (middle). In contrast to MLC2103, BL036 shows a significant polarization dependence. For x-polarized light, two distinct peaks are measured at 510 nm and 575 nm. The latter is almost absent for the attenuation of y-polarized light.

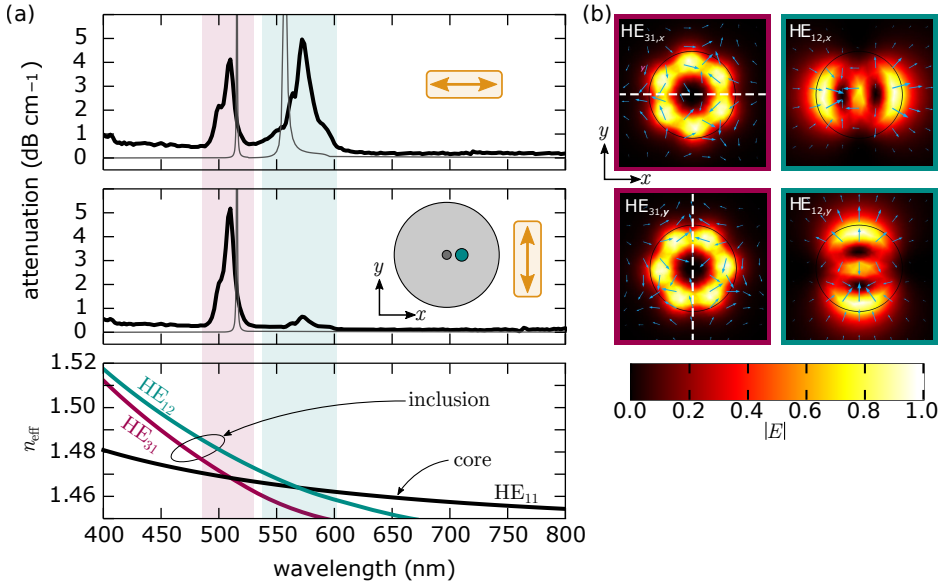

Figure 4.11. (a) Attenuation spectra for (top) x- and (middle) y-polarized light in fiber I filled with BL036. The bottom plot show the effective refractive indices of the involved core and inclusion modes. The inset shows that the inclusion and the core are located on the x-axis. (b) Distributions of the norm of the electric field for the inclusion modes interacting with different polarizations.

By calculating the effective refractive indices of the core and inclusion modes [Fig. 4.11 (a), bottom], we find that the core HE_{11} mode is interacting with two

inclusion modes: HE_{12} and HE_{31}. To explain the different attenuation spectra of x- and y-polarized light, we have to investigate the modal structure of the inclusion modes.

In Fig. 4.11 (b) the two inclusion modes of importance are plotted. Both are two-fold degenerate because of their hybrid nature. At 510 nm, light of both polarizations couple with the HE_{31} inclusion mode. But the x-polarization couples only with one of the two degenerate modes, while y-polarized light couples to the other.

We can understand this behavior by looking at the symmetries of the involved modes. For the $HE_{31,x}$ there exists a mirror plane parallel to the x-axis [dashed white line in Fig. 4.11 (b)]. The $HE_{11,x}$ mode fulfills this symmetry, but not the $HE_{11,y}$ mode. Same applies for the $HE_{31,y}$ mode but with a mirror plane along the y-axis.

The same discussion is valid for the interaction with the HE_{31} mode. But here, the two degenerate modes are strongly anisometric [Fig. 4.11 (b)]. This influences the coupling for the different polarizations of light. Here, the geometry decides, which polarization will be extinct more severely. In our case, the inclusion and the core are located on an axis that is parallel to the x-axis. From the modal distribution of the $HE_{31,y}$ mode, it is immediately clear that the interaction with the core is significantly reduced compared to the $HE_{31,x}$ mode.

If we compare the experimental values for the attenuation [solid black lines in Fig. 4.11 (a) bottom] with the results from coupled mode theory (thin gray lines), we observe good agreement, the positions are slightly shifted, though.

A strong difference is in the peak widths, which are much broader in the experiments. This is probably mainly due to the fluctuations of the director, which lead to broadening of the refractive index distribution. This is not taken into account in CMT. Connected to this fact is that the experimental peak attenuations are lower than the theoretical predictions. Nevertheless, it is captured correctly that the attenuation peak caused by the HE_{12} inclusion for x-polarized light is broader than the attenuation due to the HE_{31} mode.

4.3.2.2. Electrooptics

In Fig. 4.12 the relative power under a voltage of 500 V and 1 kHz is plotted for both polarizations of light. Similar to the case of MLC2103 (cf. Sec. 4.3.1), the reorientation of the LC molecules changes the modes and thus the coupling. A difference is here, that the involved inclusion modes are not linearly polarized but have mixed contributions. Thus, all modes react to the external field. This leads to the increase in optical power at 510 nm for x- and for y-polarized light. At 580 nm, only for the x-polarization the relative optical power is increased: Only for this component the high attenuation was detected in the field-off state which is now reduced. At higher wavelengths (>600 nm), both components show a decrease in

optical power but the y-polarized light is effected more severely.

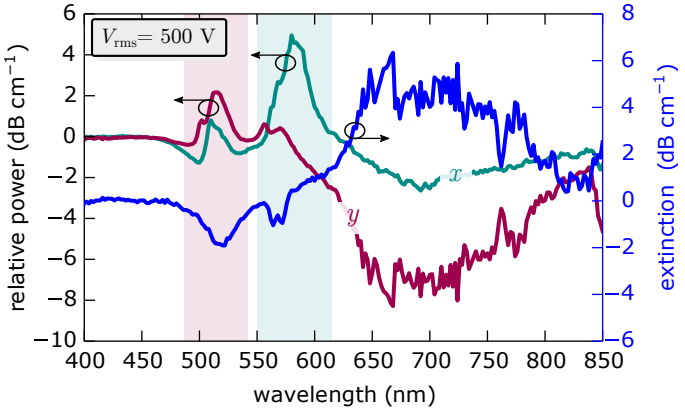

Figure 4.12. Electrooptic effects in fiber I filled with BL036. The relative power for x- and y-polarized core modes is plotted for an applied voltage of 500 V at 1 kHz. From the relative power, the polarization extinction is calculated (blue line).

This affects the polarization extinction [cf. Eq. (4.3)], which is strong in the region from 600 nm to 750 nm. A possible explanation for this strongly anisotropic behavior is that in y direction, due to the increased refractive index in the inclusion in this direction, a multitude of additional modes occur, which couple mainly to the y-polarized core mode. These new inclusion modes also affect the x-polarization as can be seen from the decrease in optical power. But the interaction is not as strong as in the case of y-polarized light.

Now, we discuss the switching dynamics under different voltage amplitudes. We will limit ourselves to one particular wavelength and a single polarization direction. We use the x-polarization at 590 nm, which has a dark state in the field off state and exhibits increasing intensity with increasing voltage. The switching behavior for different voltages is shown in Fig. 4.13 .

The most obvious finding is that with increasing voltage the intensity increases. This follows from the increasing change of the refractive index which seems to gradually impair the coupling between core and inclusion. Below 200 V, we observe no change in intensity. With a fiber diamater of 200 µm, the electric field is about 1 V µm^{-1}, which is the value needed to achieve switching in planar aligned liquid crystal cells.

The switching-on process becomes faster with increasing voltage. The 10-90-time at 800 V is $t_{\mathrm{on}} = 1.9$ ms. For lower voltages, the switching-on process is slower as is expected from a Freedericksz-type of transition. The decay times in general take longer, for 800 V we find $t_{\mathrm{off}} = 3.5$ ms.

If we calculate the switching times for the Fréedericksz transition in a planar [Eqs. (2.21) and (2.22)] we arrive at $\tau_{\mathrm{off}} = 3.2$ ms and $\tau_{\mathrm{on}} = 0.20$ ms. Here we assumed $\gamma_1 = 0.28$ Pa s and $K_{11} = 15.1$ pN (cf. Appendix A.3.2). We set $\frac{E}{E_c} = 4$ for a voltage of 800 V under the assumption that the critical voltage is reached at

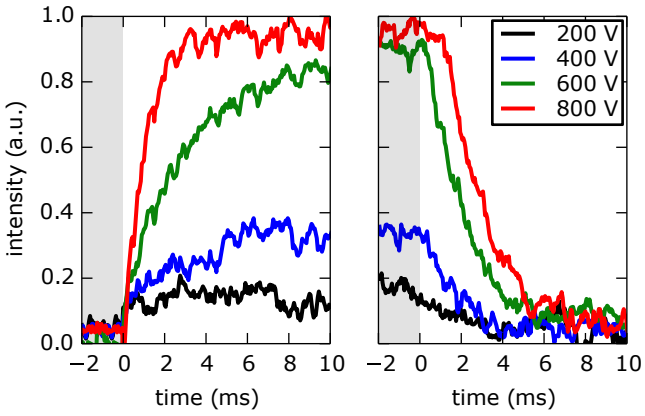

Figure 4.13. Dynmics of the switching in fiber I filled with BL036 under different voltages from 200 V to 800 V at 1 kHz. Intensity changes during the switching on process (left) and switching off (right). The switching process occurs at $t = 0$ in each case.

200 V. We see that the switching off time fits rather well with the experiments in the capillaries. However, the switching on time is off by an order of magnitude. Thus it seems that for the switching on times Eq. (2.22) is not applicable to circular geometries.

4.3.3. Fiber II filled with BL036/E7

As mentioned above, the fibers of type I are not suitable for infrared transmission due to their small core. Therefore, we use fibers of type II with a core diameter of 3.8 µm and a inclusion diameter of 1.7 µm. For these fiber we use the liquid crystals E7 and BL036. The mixture MLC2103 did not show any significant effects, neither for attenuation nor for electrooptics. For the LCs E7 and BL036, we only present the electrooptic measurements because the transmission through these fibers is not attenuated by the LCs in the field off state. Therefore there was no measurable attenuation.

In Fig. 4.14 the relative power (a, b) and the extinction (c, d) are plotted for a voltage of 500 V. Under an applied voltage, both liquid crystals lead to an decrease in optical power which is consistent with the observation that the attenuation in the field-off state is negligible. Both show a strong voltage-induced drop of relative power peaking at about $-8\,\mathrm{dB\,cm^{-1}}$ for y-polarzied light. The loss in relative power occurs over a broader spectrum for BL036 (1000 nm to 1400 nm) compared to E7 (1050 nm to 1350 nm). This might be related to the higher extraordinary refractive index of BL036 ($n_\mathrm{e} = 1.792$ at 589 nm) compared to E7 ($n_\mathrm{e} = 1.737$ at 589 nm). The larger index of BL036 leads to more modes and, consequently, to more possibilities for the mode coupling.

For both liquid crystals, x-polarized light is much less attenuated compared the y-polarized component. This leads to a strong extinction [Fig. 4.14 (c, d)] over a

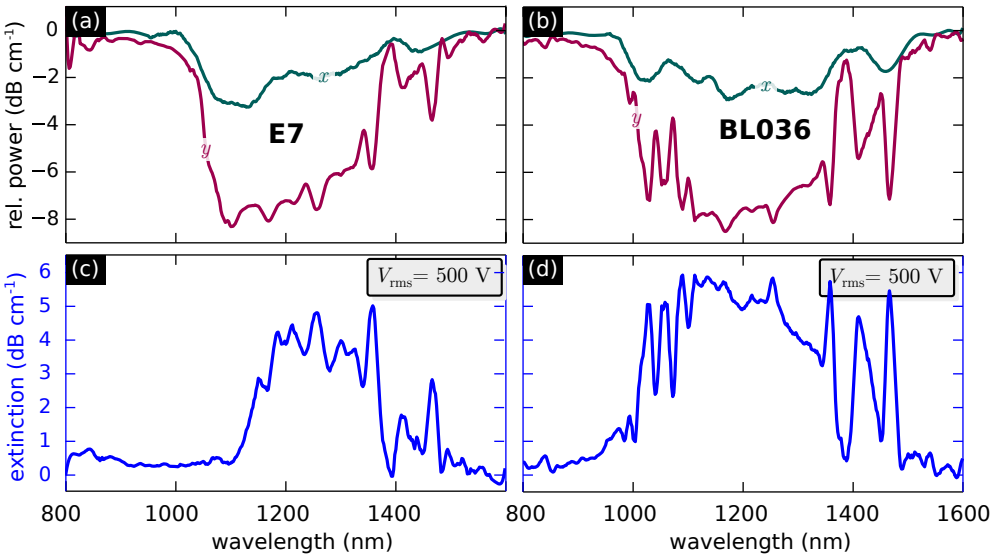

Figure 4.14. Electrooptic effects in fibers of type II filled with E7 (a, c) and BL036 (b, d). The measurements are performed at 500 V and 1 kHz. The relative power (a, b) is recorded for the two orthogonal polarizations x and y.

broad range of 300 nm for E7 and 400 nm for BL036.

Figure 4.15 shows the switching speeds of the fiber F2 filled with BL036 measured at the telecommunication wavelength of 1310 nm. The increase of intensity within the first 10 ms seems to contradict the absence of attenuation measured in the field-off state. But it lies in the margin of error of the attenuation measurements. Again, we do not observe a significant change in intensity at voltages lower than 200 V. Compared to the fibers of type I, the switching times are increased [$t_{on} = (5.0 \pm 1.0)$ ms, $t_{off} = (6.8 \pm 0.5)$ ms) at 800 V]. This is due to the increased inclusion diameter and resembles the influence of the sample thickness in flat liquid crystal cells [137].

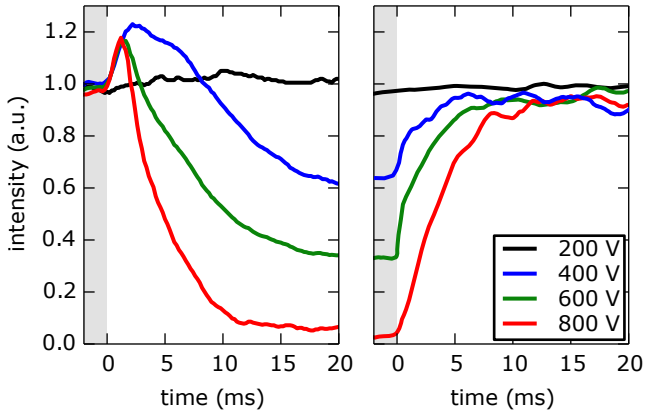

Figure 4.15. Dynamics of the switching in fiber II filled with BL036 under different voltages from 200 V to 800 V at 1 kHz at 1310 nm. Intensity changes during the switching on process (left) and switching off (right). The switching process occurs at $t = 0$ in each case.

If we again compare the switching times to the planar geometry we arrive at $t_{\text{off}} = 5.4\,\text{ms}$, which is close to the value for the circular geometry. As we already observed for the fiber of type I, the switching on time ($\tau_{\text{on}} = 0.4\,\text{ms}$) is far away from the experimental value.

Chapter 5

Liquid crystal photonic crystal fibers

In this chapter, we will mainly discuss the experimental results of the group delay measurements in liquid crystal photonic crystal fibers (LCPCFs). We briefly talked about how to turn photonic crystal fibers (PCFs) into photonic band gap fibers in Sec. 3.5.2 by infiltration of a high index liquid into the inclusions. For the experiments, we will follow this procedure and use liquid crystals (LCs) as an infiltrating material.

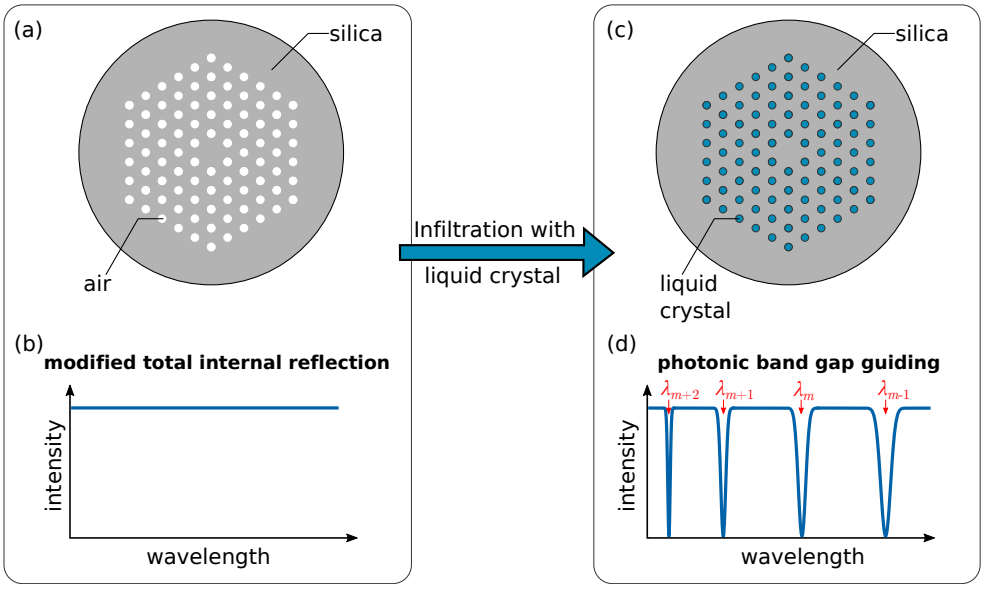

Figure 5.1. (a) Schematic of an air-filled photonic crystal fiber (PCF) with silica cladding. (b) The broad band transmission through a PCF due to the modified internal reflection guiding mechanism. (c) PCF filled with liquid crystal (blue). (d) Transmission through a liquid crystal filled PCF. The transmission shows dips with the spectral positions λ_m, which are caused by the photonic band gap guiding mechanism.

A sketch of the basic idea is shown in Fig. 5.1. We start out with a PCF [Fig. 5.1 (a)], which has air filled inclusions and guides light via modified total internal reflection (mTIR). From the latter it follows that this fiber has a broad band

transmission [Fig. 5.1 (b)] very similar to step index fibers. The infiltration with a liquid crystal [Fig. 5.1 (c)] will lead to a change in guiding mechanism from mTIR to photonic band gap guidance (PBG).

We studied the behavior of photonic band gap fibers (PBGFs) in Sec. 3.5.2 and observed dips in the transmission spectrum [Fig. 5.1 (d)], which we traced back to coupling between the core mode and the cladding. An equivalent way of investigation involved the calculation of the band gaps of the cladding. In either case, the PBG mechanism leads to spectral transmission windows opposed to the broad band transmission in the case of mTIR.

A large part of this chapter is focused on the group delay and dispersion properties of LCPCFs, which are very interesting due to the photonic band gap guiding (as we will see in Sec. 5.1.2). The benefit of liquid crystals are their tuning capabilities with external electric fields. We have seen in the previous chapter that the transmission through liquid crystal filled fiber can be greatly altered by applying electric fields. Therefore, we will briefly discuss the transmission properties of LCFPCFs under voltage, which have been extensively studied over last years. Subsequently, we will briefly review the role of PBGF for the non-linear four wave mixing process.

With this context, we will describe the experimental details like fiber preparation, electrical addressing and the group delay measurements. Especially, the fiber preparation is of interest because we will use two types of alignment: homogeneous planar and homeotropic. These will play a major role in the experiments to follow. We conclude this chapter by showing theoretically the electrically tunable FWM capabilities of the LCPCFs.

5.1. Properties of photonic crystal fibers & photonic band gap fibers

In this chapter we will discuss the waveguiding properties of liquid crystal filled photonic crystal fibers (LCPCF). We will focus on the group delay and the dispersion of such fibers.

In the case of microstructured optical fibers, we have already seen that the coupling of core and inclusion modes influences the effective refractive indices of the involved modes. The refractive indices are strongly bent close to the regions where the effective indices of core and inclusion modes match, which means that they are in resonance. In Sec. 3.6 we saw that the group velocity [Eq. (3.54)] and the fiber dispersion [Eq. (3.56)] depend on derivatives of the effective refractive index. Consequently, these properties undergo strong changes close to the resonances.

In Sec. 3.5.2 we discussed that filling an photonic crystal fiber (PCF) with a high index material leads to a fiber which confines light via photonic band gaps. But within the transmission spectrum, dips in the transmission can be found. The dips

originate from coupling of the fundamental core mode with modes (or photonic bands) of the cladding. In Fig. 3.20, we already saw that close to the transmission dips, the effective refractive index of the core mode is bent due to the coupling. Now, by changing the director configuration of the liquid crystal, we are able to influence the group velocity and the dispersion.

5.1.1. Polarizing capabilities of liquid crystal photonic crystal fibers

The tuning capabilites of liquid crystal photonic band gap fibers (LCPCFs) have been studied intensively over the past decade [27, 29, 123]. Especially, the strong polarizing properties of LCPCFs are of interest. A strong anisotropy can be induced in these fibers by applying electric fields perpendicular to the fiber axis. This effect is somehow similar to what we discussed for the liquid crystal filled microstructured optical fibers in the previous chapter.

The first results on the polarizing properties were published in 2004 by Du et al. [138] for a single wavelength in the visible range. Very soon, investigations followed which focused on the infrared [27, 139] and, in 2008, first broad band experiments in the visible were reported by Lorenz et al [28]. Intensive theoretical work has been carried out [27, 29, 123, 140–144] to describe the effect of electrically induced anisotropy on the polarization.

We can understand the polarization properties of LCPCFs qualitatively under some approximations. In Fig. 5.2 (a) a single LC filled inclusion of a PCF is shown which is filled with an axially aligned liquid crystal. The director faces along the z-direction, which is also the fiber axis. If we apply an electric field along the y-direction, the molecules align parallel to the y-axis. For very strong fields ($|\boldsymbol{E}| \gg 1\,\mathrm{V\,\mu m^{-1}}$), all molecules align perfectly along the y-axis [Fig. 5.2 (b)]. Then the dielectric tensor becomes $\bar{\bar{\epsilon}} = \mathrm{diag}\,(n_\mathrm{o}, n_\mathrm{e}, n_\mathrm{o})$. If we assume now that the core mode interacts only with cladding modes of the same polarization and that the cladding modes are linearly polarized, we can roughly treat the LC inclusion as being isotropic for a specific polarization (x or y). Then, we can predict the dips in the spectrum with Eq. (3.51)

$$\lambda_m = \frac{4d}{2m+1}\left(n_\mathrm{incl}^2 - n_\mathrm{B}^2\right)^{1/2}, \tag{3.51}$$

which originated from the ARROW model (cf. Sec. 3.5.2.1). In Eq. (3.51), λ_m is the m-th resonance, d the inclusion diameter and n_incl and n_B are the refractive indices of the inclusion and the background material, respectively.

For the inclusion index we choose $n_\mathrm{incl} = n_\mathrm{o}$ for x-polarized light and $n_\mathrm{incl} = n_\mathrm{e}$ for y-polarized light. As $n_\mathrm{o} < n_\mathrm{e}$, the resonance wavelengths will be wider spaced in the case of x-polarized light [Fig. 5.2 (c)] compared to y-polarized light [Fig. 5.2 (d)] . Then it is possible to find a wavelength λ_0 [red in Fig. 5.2 (c)], where there is maximum transmission for x-polarized light but maximum attenuation for

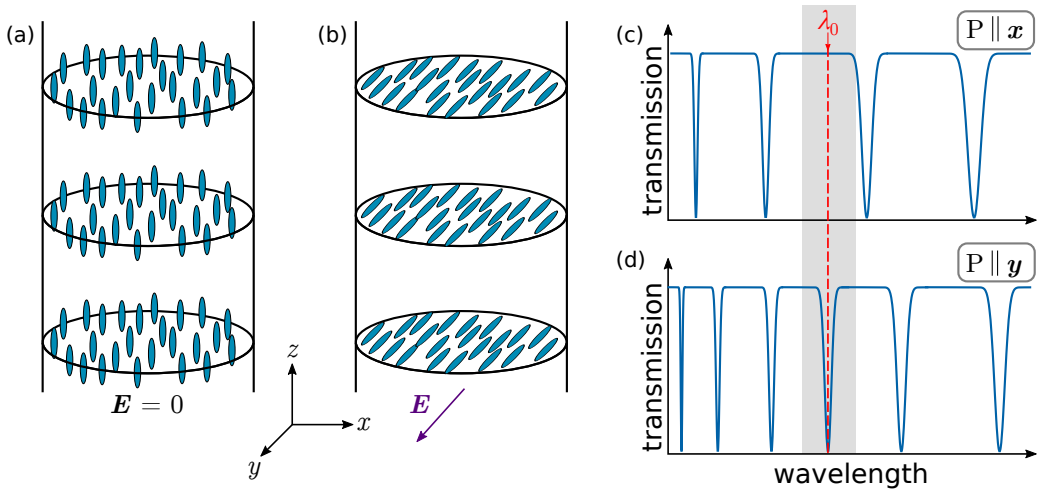

Figure 5.2. (a) Schematic of axial director field configuration in the field-off state. (b) Director field configuration under application of an electric field perpendicular to the fiber axis. (c) Polarization dependent transmission through a PCF under voltage with polarization perpendicular (top) and parallel (bottom) to the electric field.

y-polarized light. Hence, the fiber will show strong polarizing capabilities at this wavelength.

5.1.2. Effective indices, group velocity & dispersion in liquid crystal photonic crystal fibers

In Sec. 3.6 we introduced the group delay (or group velocity) and the dispersion of optical materials like silica. We elaborated how these quantities influence the propagation of pulses in dispersive media. And, in Sec. 3.7 we discovered that the same properties play an important role in achieving four wave mixing.

Here, we want to briefly describe how these quantities (effective refractive index n_{eff}, group velocity v_{g} and dispersion D) will behave in photonic crystal fibers (PCFs) and liquid crystal filled PCFs. To this end, we performed an eigenmode analysis of a LMA10 (NKT Photonic [106]) PCF with COMSOL Multiphysics [122] in two ways: with hollow inclusion (or air filled) and filled with liquid crystal mixture E7 (cf. Appendix A.3.1). For the LCPCF, the liquid crystal is assumed to be aligned axially [cf. Fig. 5.2 (a)]. This lets us directly compare the effect of changing the guiding mechanism from mTIR to PBG.

In Fig. 5.3 (a) we see the effective refractive indices n_{eff} for both structures and for comparison the refractive index of bulk silica. Additionally, we plot the normalized electric field confined to the core in the case of the LCPCF. This helps us to identify the regions of high transmission. We observe, that for PCF and LCPCF the refractive indices move below the refractive index of silica. This is to be expected from a waveguide, that guides in its background material (here silica).

A very important fact is, that the effect refractive index n_{eff} of the LCPCF tends

to cross the n_{eff} of the PCF close to the center of the respective transmission window. We will use this fact later in the discussion of the four wave mixing process. At the edges of the transmission windows, the index of the LCPCFs deviate from the PCF due to the coupling to inclusion modes in the case of the LCPCFs.

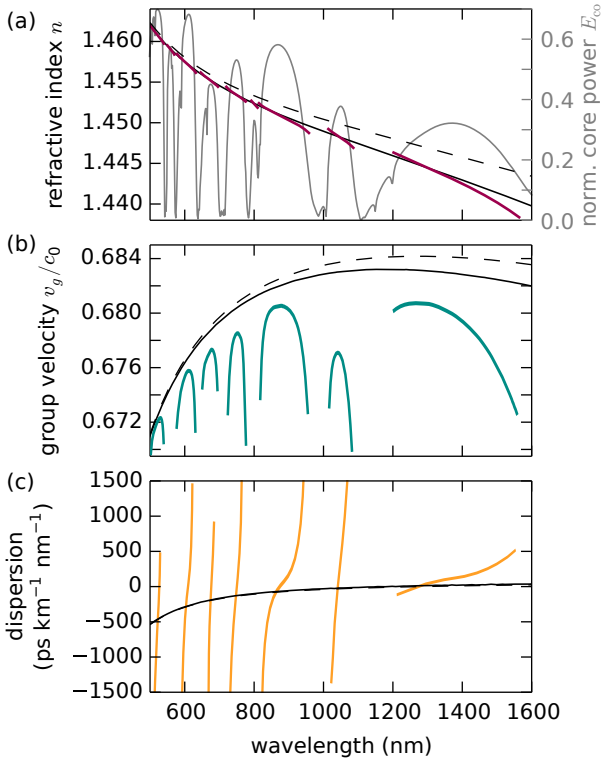

Figure 5.3. Simulated properties of a liquid crystal filled photonic crystal fiber (LCPCF, solid colored lines), a photonic crystal fiber (PCF, solid black line) and bulk silica (dashed black line): (a) Effective refractive indices and normalized electric field (gray) confined to the core region of the LCPCF. (b) Group velocity normalized by the speed of light c_0 and (c) dispersion.

These deviations involve a strong first derivative of the effective refractive index n_{eff} with respect to the wavelength, which we can directly observe by looking at the group velocity v_{g} [Fig. 5.3 (b)]. The PCF and the silica only exhibit a single maximum in v_{g} at approximately 1180 nm and 1285 nm, respectively.[†] This is strikingly different for the LCPCF, where we have a maximum for each of the transmission windows.

We already established that the dispersion of a waveguide is proportional to the derivative of the reciprocal group velocity [$D \propto \left(\frac{\partial v_{\text{g}}^{-1}}{\partial \lambda}\right)$, cf. Eq. (3.56) in Sec. 3.6]. Consequently, we observe a zero disperison wavelength (ZDW) for each transmission window in the LCPCF [Fig. 5.3 (c)]. Bulk silica (as we already have discussed in Sec. 3.6) and the PCF only have one ZDW in the entire wavelength range. The

[†]The difference between the PCF and silica is due to the influence of the waveguiding structure. In fact, the maximum of v_{g} can be pushed further towards the visible range by smaller inclusion diameters.

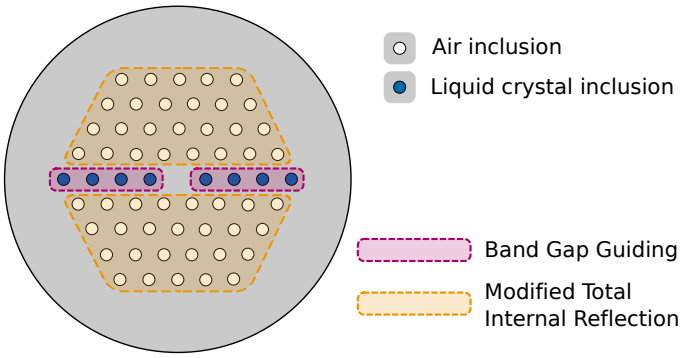

Figure 5.4. Schematic of the cross section of a photonic crystal fiber of which the horizontally aligned inclusions are filled with a liquid crystal. The red shade marks the region where light is confined by photonic band gaps, the yellow shade indicates regions of modified total internal reflection.

importance of ZDWs for the FWM process was shown in Sec. 3.7.2. And we will discuss FWM in electrically addressed LCPCFs in Sec. 5.3.4.

5.1.3. Four wave mixing in PBGFs & hybrid guiding fibers

As discussed in Sec. 3.7, four wave mixing (FWM) is difficult to achieve in standard optical fibers as well as PCFs in the visible wavelength range due to the absence of zero dispersion wavelengths. In 2008, Rasmussen et al. [145] considered theoretically using all-solid PBGFs[†] as FWM source. The first experiments based on the full PBGF structure were carried out in 2011 [146]. In 2013, hybrid guiding fibers were used for the four wave mixing process [38, 147].

Hybrid guiding fibers make use of both guiding mechanisms: modified total internal reflection (mTIR) and photonic band gaps (PBGs). Figure 5.4 shows a hybrid guiding structure in which the inclusions located on the x-axis are made from high index material; the remaining inclusions are left empty. Consequently, light along the x-axis is confined by photonic band gaps while in the other directions modified total internal reflection keeps the light inside the core. A structure as shown in Fig. 5.4 induces a birefringence due to its reduced symmetry, which can be beneficial for fulfilling the phase matching condition.

Beside these benefits for the FWM process, this type of structure has a positive effect on LCPCFs as well. LCPCFs usually suffer from the scattering due to the liquid crystal which lead to high attenuation ($\gtrsim 1\,\mathrm{dB\,cm^{-1}}$). These losses can be reduced significantly in hybrid guiding fiber while maintaining the unique dispersion properties and the electrical tuning capabilities.

[†]Fibers which are made completely from glass. For the inclusions, a glass with higher refractive index is chosen than for the background material.

5.2. Experiments

5.2.1. Fiber specifications

For the experiments, we use two different kinds of commercially available large mode area fibers, LMA8 and LMA10 from NKT Photonics [106]. Both fibers are solid core fibers made from silica. The geometric specifications are $d = 2.58\,\mu m$ and $\Lambda = 5.61\,\mu m$ for LMA8 and $d = 2.91\,\mu m$ and $\Lambda = 6.53\,\mu m$ for LMA10. Here, d is the inclusion diameter and Λ is the lattice constant (Fig. 5.5). Both fibers have a cladding diameter of $125\,\mu m$ and are surrounded by an acrylate coating leading to an outer diameter of $250\,\mu m$ in total.

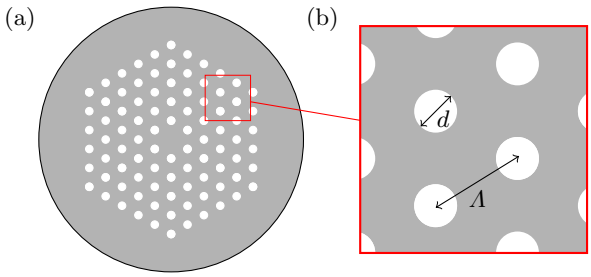

Figure 5.5. (a) Sketch of the cross section of a photonic crystal fiber with hexagonal arrangement of air inclusions. (b) Close-up of the cladding structure with inclusion diameter d and lattice constant (or pitch) Λ.

5.2.2. Sample preparation

We explained in Sec. 2.4 how to change the anchoring conditions on the surface for liquid crystals by chemically treating the inclusion surfaces. We make use of these techniques here to achieve axial (planar) and homeotropic (perpendicular) alignment. We already used axial anchoring in the case of microstructured optical fibers, where we treated the surface with glymo for degenerate planar anchoring. The axial configuration is obtained because it is the only configurations which has no distortions and has therefore the lowest free energy.

This works well for single capillaries, for which we can check the alignment and cut off poorly aligned pieces. But for PCFs, which have ∼50 inclusions, this is not an effective method. Instead, we use the photoalignment technique to achieve the desired axial alignment. We introduced the basic principle by describing the alignment of poly-vinylcinnamate in Sec. 2.4.2.

5.2.2.1. Axial anchoring

The basic procedure to apply this technique to PCFs is show in Fig. 5.6 (a). First, the poly-vinylcinnamate (PVCi) solution (2 % in cyclopentanone) is filled into the PCF by capillary forces and a mild pressure gradient of 1 bar. To speed up the process for filling longer pieces of fibers, vacuum can be applied on the other end of

the PCF. Secondly, after the PCF is fully filled with the PVCi solution, the liquid is extracted from the PCF by applying nitrogen from one end under a pressure of about 3 bar. This leaves behind a thin film of PVCi solution on the surface. At last, the samples are dried for 24 h at 135 °C. Exposure to ambient light during this procedure should be avoided to prevent the cycloaddition.

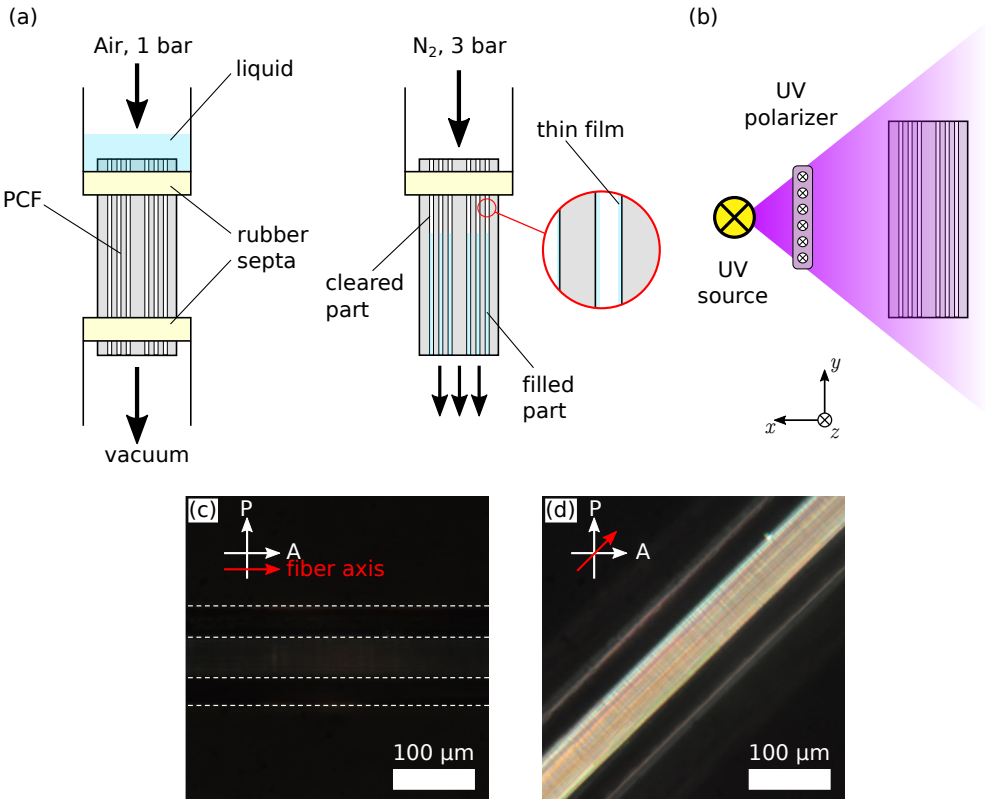

Figure 5.6. (a) Schematic representation of the filling (left) and extraction (right) procedure of a photonic crystal fiber (PCF). (b) Schematic of a linear polarized UV polymerization of a poly-vinyl cinnamate inside the PCF inclusions. (c, d) Polarization optical microscope images of an aligned liquid crystal filled PCF with the fiber axis parallel (c) and in an 45° angle (d).

The PVCi film is then oriented by using polarized UV light from a UV source (Hönle Blue Point 4). The polarization direction is perpendicular to the fiber axis to achieve an axial anchoring (cf. Fig. 2.19). The intensity in UV-A spectral range (315 nm to 400 nm) is ∼1 mW cm^{-2} (measured with a Hönle UV-meter). The typical UV-dose to achieve full crosslinking of the PVCi is about 5 J cm^{-2}.

Figure 5.6 (c, d) shows polarizing microscope images of a PCF prepared as described above and then filled with the liquid crystal mixture E7. In Fig. 5.6 (c), the fiber axis is parallel to the polarizer. Thus, there is no apparent birefringence and the filled inclusions remain dark. This is a clear indication that the LC is homogeneously axially aligned. By rotating the fiber sample by 45°, the birefringent inclusions become visible [Fig. 5.6 (d)].

5.2.2.2. Homeotropic anchoring

A type of anchoring we have not encountered in practice so far is the homeotropic anchoring, where the LC molecules are aligned perpendicular on the surface. To achieve this anchoring, we fill the PCFs with a lecithin solution (2 % in hexane) with the same technique used for the PVCi solution [cf. Fig. 5.6 (a)]. After extraction, we dry the samples at 70 °C for 1 h.

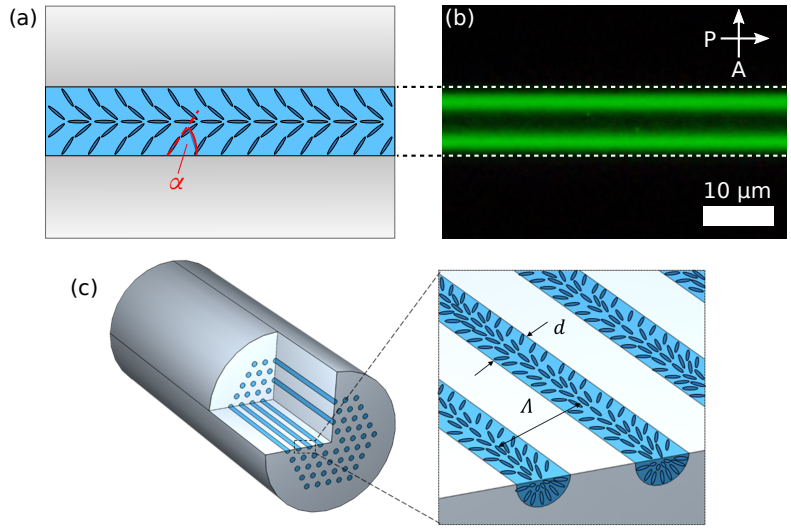

Figure 5.7. (a) Schematic of radial escaped liquid crystal orientation in a capillary with homeotropic anchoring with finite anchoring energy. Directly on the surface, the LC molecules take an angle α with respect to the surface. The director becomes parallel to the capillary axis in the center. (b) Polarizing optical image of a capillary with aligned liquid crystal. (c) Schematic of a photonic crystal fiber with homeotropic anchoring.

In Fig. 5.7 (a) we show a sketch of a single capillary with homeotropic anchoring. The molecules anchor on the surface with an angle $0 < \alpha < \pi/2$. The anchoring is not perpendicular to the surface because the anchoring energy has to compete with the distortion energies of the director field in the bulk [cf. Sec. 2.4.3].

To check the alignment provided by the lecithin treatment, we filled a 10 µm capillary with the dual-frequency adressable liquid crystal MLC2048. The polarizing microscope image is shown in Fig. 5.7 (b) (cf. Appendix A.3.4 for the physical properties). On the capillary walls, the LC is anchored at an angle which leads to the bright stripe close to the capillary walls. In the center of the capillary, the director is parallel to the polarizer, thus there is no transmittance there. Hence, we can assume that fibers capillaries and inclusions treated in the prescribed way exhibit a radial escaped director field.

Finally, Fig. 5.7 (c) shows a sketch of a PCF with homeotropic anchoring. The inclusion diameters in the PCF are much smaller than the capillary discussed above. Therefore, we also checked the alignment for capillaries with 2 µm diameter. They show the same kind director field, but due to the small diameter the POM images are not as informative.

5.2.2.3. Hybrid guiding fibers

We briefly discussed hybrid guiding fibers (HGFs) in Sec. 5.1.3. Here, we present an easy technique to produce HGFs with a simple geometry similar to the one shown in Fig. 5.4 . The basic idea is to seal some inclusions which then during the liquid crystal filling process remain free.

We use a tapered capillary to deposit glue (Norland Optical Adhesive NOA61) on the end facet of a PCF [Fig. 5.8 (a)]. For this purpose we employ a microscope and observe the fiber end in reflection. The capillary is controlled manually via a (x, y, z)-translation stage. We use the capillary to selectively fill the inclusions with glue that are supposed to remain free of the LC.

The glue is then cured with a UV LED (365 nm) with an intensity of $\sim$1 mW cm^{-2}. Structures we produced are shown in Fig. 5.8 (b, c). The selectively sealed PCF can then be filled with liquid crystals (or other liquids). We chose to apply the alignment layers in these fibers before the sealing procedure to avoid the exposure of the glue to solvents (hexane or cylcopentanone).

With the presented technique it is possible to create simple hybrid guiding fibers. For more complex geometries other techniques have to be used. For example two photon absorption has been employed to be able to close single inclusion with a focused laser beam [148, 149]. This is a very versatile approach but requires an expensive setup.

5.2.3. Liquid crystal materials

In this chapter we will employ two different liquid crystal mixtures: E7 and MLC2048. E7 ($n_o = 1.522$, $n_e = 1.739$ at 589 nm, cf. Appendix A.3.1) we already used in the previous chapter on microstructured optical fibers. However, the dual frequency mixture liquid crystal (DFLC) MLC2048 ($n_o = 1.498$, $n_e = 1.716$ at 589 nm, cf. Appendix A.3.4) will play the greater role in this chapter. We already discussed some properties of DFLCs in Sec. 2.2.1.

For us, the most important property of MLC2048 is that the dielectric anisotropy is $\Delta\epsilon(1\,\text{kHz}) = +3.3$ and $\Delta\epsilon(50\,\text{kHz}) = -3.3$. The dual frequency behavior together with the homeotropic anchoring of the liquid crystal inside microcapillaries enable continuous electrical tuning of the photonic band gaps [27].

5.2.4. Group delay measurements

When we introduced the group velocity and the dispersion in Sec. 3.6, we already have mentioned that the measurement of these quantities is relatively simple. In general we have to measure how much time an optical pulse needs to travel through our fiber sample. For long fibers this can be done by time of flight measurements where an optical pulse is sent through several hundred meters or kilometers of fiber

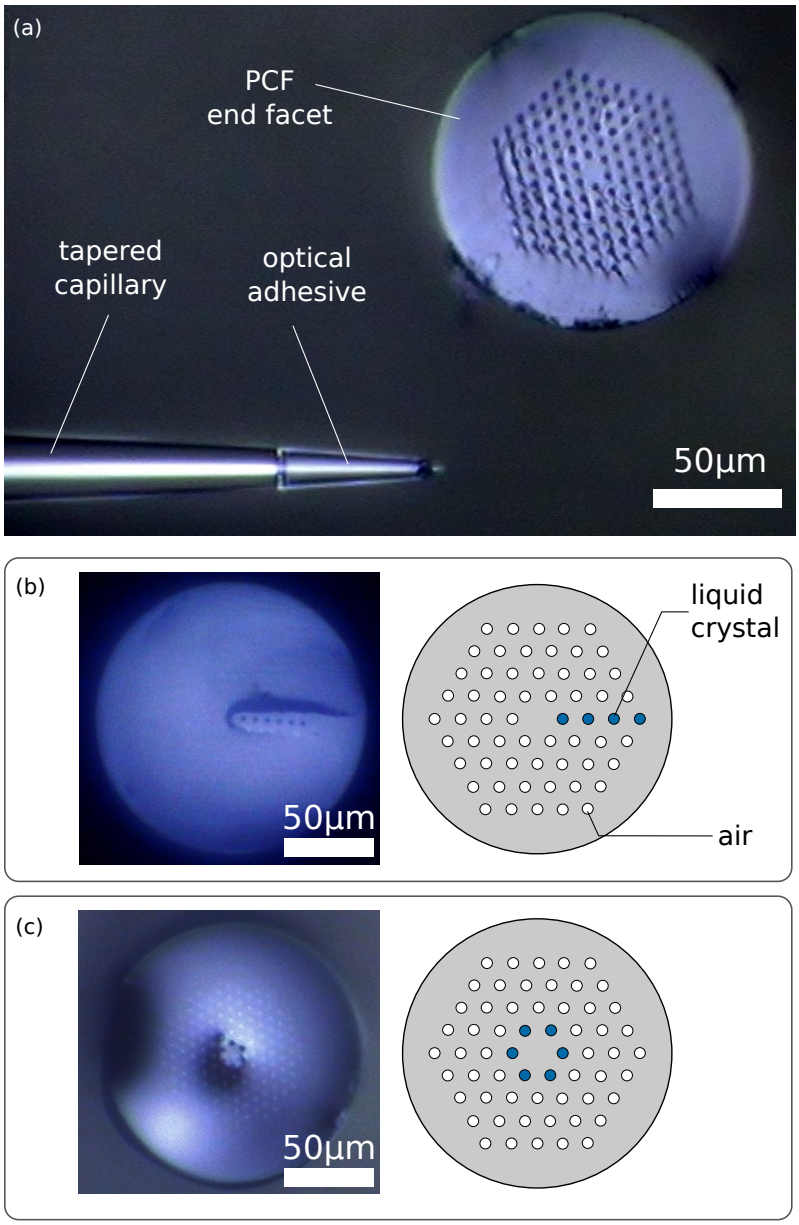

Figure 5.8. (a) Optical microscope images in reflection of manual the gluing technique: End facet of a LMA8 photonic crystal fiber before selective sealing and an adhesive covered capillary. (b, c) Microscope images of the created patterns on the end facet of the fiber and sketches of the resulting liquid crystal filled fibers.

and the time is measured. However, the samples we use are only a few centimeters in length. Thus, time of flight is not an option.

For such short fiber pieces interferometry is a suitable method, which we employ by using a Mach-Zehnder interferometer [Fig. 5.9 (a)]. The general idea for this setup is to generate small band optical pulses and split them into two. One portion of the split pulse is coupled into the fiber under test. The other part travels over a delay path, which can be adjusted in length. The two pulses are then recombined and the combined result is measured at the detector. The delay path is varied for this

measurement in order to overlap the pulses and create an interference pattern on the detector. Then, by changing the center wavelength of the incoupled pulse, the length of the delay path will vary due to the chromatic dispersion. The change in delay path is recorded and together with the change in wavelength the group delay, group velocity and finally the dispersion can be determined.

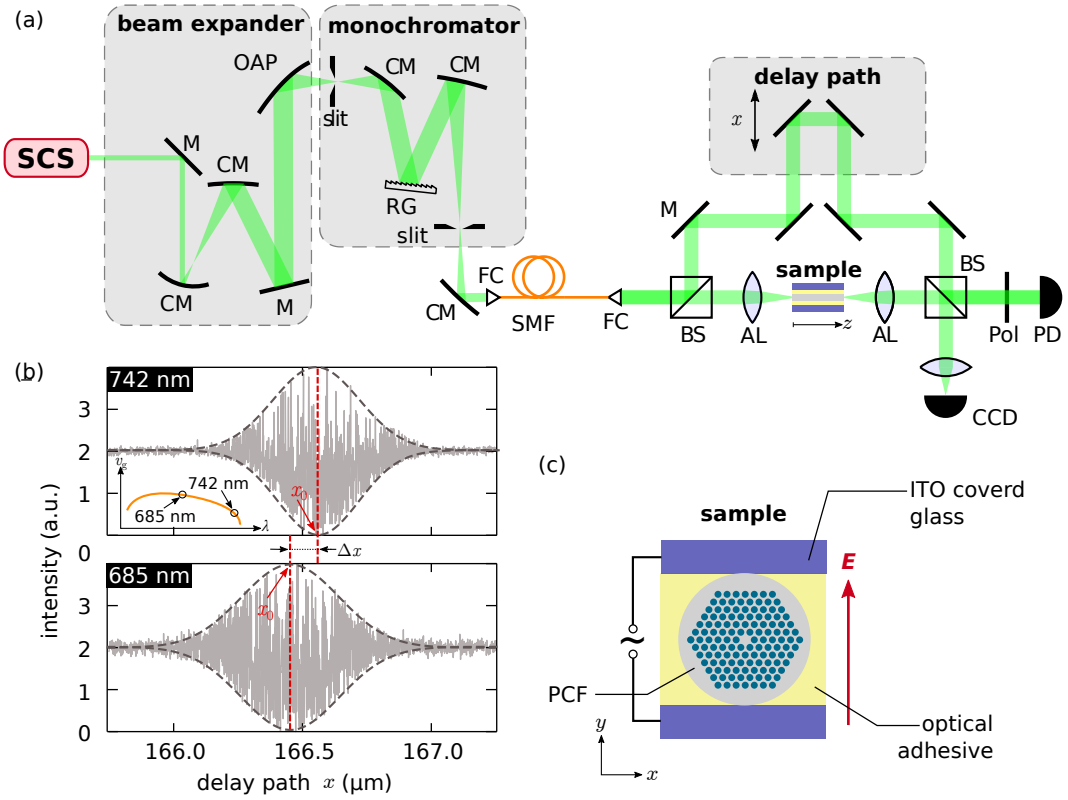

Figure 5.9. (a) Sketch of the optical setup for measuring the group delay in optical fibers: supercontinuum source (SCS), mirror (M), concave Mirror (CM), off-axis parabolic mirror (OAP), reflective grating (RG), fiber coupler (CC), beam splitter (BS), achromatic lense (AL), polarizer (Pol), photo diode (PD), CCD Camera (CCD). (b) Measured interference pattern at two different wavelengths generated by adjusting the delay path. The inset shows the group velocity. (c) Schematic of the cell for electrical addressing of the liquid crystal filled photonic crystal fiber (PCF).

In practice, the optical pulses are generated by a supercontinuum source (NKT SuperK Compact, 450 nm to 2000 nm, ~1.5 ns). The pulses are spectrally filtered with a Czerny-Turner monochromator. For spatial filtering, the monochromator output is coupled into a single mode LMA10 (NKT Photonics) fiber. The output of the fiber is collimated and then split with a beam splitter. One part passes through the variable reference path. The other beam is coupled into the fiber sample. The two beams are overlapped by a second beam splitter. Finally, the recombined beams are detected with a silicon photodiode (Femto FWPR-20-Si).

The delay path is scanned for each measurement in order to detect the interference pattern. In Fig. 5.9 (b), two interference patterns measured at different wavelengths are shown. There is a clear shift of center position x_0 of the delay path. Light at the

longer wavelength travels slower than light at shorter wavelengths. The difference is mainly caused by the higher curvature of the effective refractive index at 742 nm [cf. inset top figure]. From this change in center position the dispersion can be calculated with Eq. (3.56).

To investigate the effect of electric fields on the dispersive properties of LCPCFs, we sandwich the LCPCF between conducting indium tin oxide (ITO) plates. We fix it with an optical adhesive (Norland Optical Adhesive NOA 65), which is cured with a UV LED at 365 nm. The voltages applied to the samples are generated by a waveform generator (WaveTek 270) and are amplified (Krohn-Hite amplifier). Throughout this chapter, we use sine waves with frequencies of either 1 kHz or 50 kHz. These frequencies allows us to make use of the dual-frequency behavior of the liquid crystal MLC2048. The root mean square values of the applied voltages range from 0 V to 200 V.

5.3. Results

In this section we present and discuss some experimental results on the group delay and dispersion of liquid crystal filled photonic crystal fibers (LCPCF). We will focus on the polarization dependent effects which occur due to the electrically induced anisotropic director field.

We will start out by discussing planar aligned liquid crystals as the simplest example. We then move on to the more complex case of a homeotropically aligned dual frequency liquid crystal. Finally, we describe the interesting features of hybrid guiding fibers.

5.3.1. Planar aligned liquid crystal photonic crystal fibers

The first example of group delay measurements in an LCPCF is an LMA8 filled with the nematic LC mixture E7. The inclusions of the fiber have been treated with poly-vinylcinnamate to achieve axial anchoring [cf. Sec. 5.2.2.1].

The transmission spectrum of a sample with a length of 11.9 cm is shown in Fig. 5.10 (a). We observe multiple spectral transmission windows as expected from a photonic band gap fiber. The fiber shows no polarization dependence with respect to light coupled being x- or y-polarized. This is in agreement with the axial director field.

We measured the group delay of this fiber [red cricles in Fig. 5.10 (b)] with the setup described in Sec. 5.2.4. We find that each of the transmission windows has a very distinct group delay curve. Close to the edges of these transmission windows, the group delay curves show the expected strong bending, which leads to a minimum of the group delay within each window (except for the band gap at ~ 460 nm). This minimum is roughly located at the center of the transmission windows.

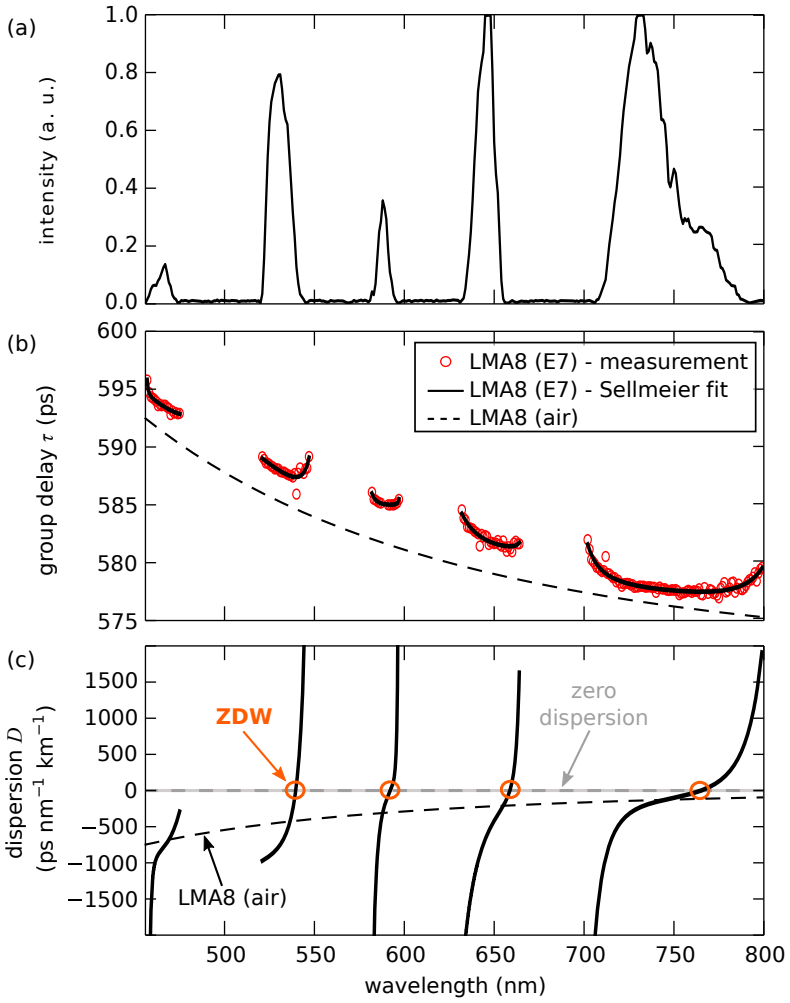

Figure 5.10. (a) Transmitted white light intensity through a LMA8 fiber with axially aligned liquid crystal E7. (b) Measured group delay (red circles) with fitted line (solid black line) over at over the visible wavelength range in an 11.8 cm long E7 filled LMA8. As a reference, the group delay of an empty LMA8 fiber (dashed black line) of similar length is plotted. (c) The dispersion curves (solid black lines) obtained from the fits in (a). Again an empty LMA8 fiber serves as a reference (dashed black line). The zero dispersion line is plotted (dashed gray line) and the positions where the dispersion of the E7 filled LMA8 crosses this line are marked (ZDWs).

If we focus on the general course of the group delay, we see that it decreases with increasing wavelength, which is caused mainly by the material dispersion. This is also confirmed by the group delay of an unfilled LMA8 fiber of similar length (11.8 cm), which we measured. For the unfilled fiber, we know from Fig. 5.3 that its properties are determined to great extent by the background material (silica).

In order to calculate the dispersion of the fiber from the group delay, we fitted the effective refractive index n_{eff} of the guided fundamental mode in each transmission window with a Sellmeier fit of the form

$$n_{\text{eff}}^2 - 1 = \sum_{i=1}^{3} A_i \frac{\lambda^2}{\lambda^2 - \lambda_i^2}. \tag{5.1}$$

The effective index and the group delay are connected by [Eqs. (3.54) and (3.55)]

$$\tau = \frac{L}{v_\mathrm{g}} = \frac{L}{c_0}\left(n_\mathrm{eff} - \lambda\frac{\partial n_\mathrm{eff}}{\partial\lambda}\right)$$

where L is the fiber length, λ the wavelength and c_0 the speed of light. As initial values for the resonances λ_i in Eq. (5.1), we use the band gap edges for λ_1, λ_2 and $\lambda_3 = 0.2\,\mu\mathrm{m}$ to include the material dispersion. With these initial values, the fitting process was performed by a least-squares method.

The Sellmeier equation is usually used to model refractive indices of materials, of which the absorption resonances are known. In our case, this makes sense in so far that the material absorption resonances have a similar effect as the waveguide resonances. The fit obtained with this procedure is in good agreement with the measured data [solid black line in Fig. 5.10 (b)].

The Sellmeier fits guarantee smooth derivatives close to the resonance wavelengths λ_i. So, by using Eq. (3.56), we are able to obtain the dispersion D from the fits. The results are shown in Fig. 5.10 (c). For comparison, we again plot the dispersion of an air-filled LMA8 (black dashed line). As expected, the dispersion of the LC-filled is fundamentally distinct from dispersion of the unfilled PCFs. For the unfilled fiber, we observe a monotonically increasing negative dispersion over the displayed wavelength range. The dispersion of the LCPCF exhibits positive and negative dispersion for (almost) every transmission window. The window at around 460 nm is an exception because the long wavelength edge could not be measured due limits of the experimental setup in this spectral range.

The strongly varying dispersion leads to the appearance of multiple zero dispersion wavelengths (ZDWs) in the visible wavelength range [marked orange in Fig. 5.10 (c)]. The unfilled fiber, however, does not have a ZDW in this range.

In the next step, we applied an electric field to the LCPCF and tried to measure the group delay. Unfortunately, these experiments did not yield results, from which we could retrieve the group delay and the dispersion. We believe that this is a consequence of the strong changes in the director field induced by the Fréedericksz-like switching Sec. 2.3. We have already seen in the case of microstructured optical fibers (Sec. 4.3.1.2), that the application of a voltage can lead to broad band losses due to coupling of various modes.

A more promising idea than using a Fréedericksz transition is a continuously tunable LCPCF which can be realized by using a homeotropic anchoring. This will be discussed in the subsequent sections.

5.3.2. Homeotropically aligned liquid crystals in photonic crystal fibers

The use of a homeotropically anchored LC allows for continuous tuning of the spectral positions of the photonic bands. Furthermore, by using a dual frequency

addressable LC (DFLC), the band gaps can either be red or blue shifted depending on the applied frequency [27]. In this section we will first give a qualitative description of the induced shift and then will show the experimental results for the prepared fibers.

5.3.2.1. Director field simulations

To get a qualitative picture of the influence of electric fields on a homeotropically aligned DFLC in microcapillaries, we use finite element simulations to calculate the director field. We already presented the governing partial differential equation for the director deformations [Eq. (2.16)] in Sec. 2.1.5.

Here, we work in the one constant approximation (all elastic constants of the LC are equal) and further assume that the director is anchored normal to the surface. Due to these approximations, the results can only be interpreted qualitatively. But the picture we gain from this will help to explain what we measure in the experiment.

We will further simplify the problem of a DFLC filled PCF [Fig. 5.11 (a)] by considering a single inclusion in the center of a plate capacitor [Fig. 5.11 (b)]. There is some error involved by leaving out other inclusions which influence the electric field distribution but as we are only interested in a qualitative picture this error is acceptable. Treating the material surrounding the inclusion as homogeneous is justified as the dielectric constant of the cladding (silica, $\epsilon = 3.8$) is very similar to the adhesive ($\epsilon = 3.9$) [113].

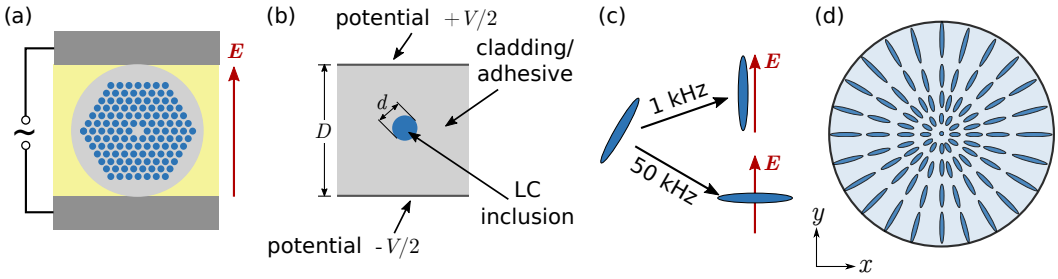

Figure 5.11. (a) Schematic of a liquid crystal filled photonic crystal fiber sandwiched between conducting ITO plated. The result electric field is perpendicular to the fiber axis and to the ITO plate. (b) Simplified of modeling of the structure in (a) considering only a single inclusion in a plate capacitor. (c) Effect of voltage at different frequencies on a liquid crystal molecule. (d) Schematic of a escaped radial director field inside a single inclusion with perpendicular anchoring on the walls.

We simulate the director field by solving Eq. (2.16) with the applied voltages $V = 0\,\mathrm{V}$ and $V = 200\,\mathrm{V}$ with the finite element software COMSOL 4.2 [122]. We treat the field as static thus we can use the electrostatics module supplied by COMSOL 4.2 to solve the corresponding Maxwell equations. We model the dual frequency behavior of the liquid crystal MLC2048 by choosing the dielectric anisotropy to be $\Delta\epsilon = +3.3$ to describe the dielectric response at 1 kHz and $\Delta\epsilon = -3.3$ at 50 kHz. As shown in [Fig. 5.11 (c)], this will force the director to be parallel to the electric field $\boldsymbol{E}$ in

the former case and perpendicular to $\boldsymbol{E}$ in the latter case. The elastic constant is assumed to be $K = 13.0\,\mathrm{pN}$. Further physical properties of MLC2048 can be found in Appendix A.3.4. As a reminder of the redial escaped director field, Fig. 5.11 (d) shows a sketch of the LC director orientation in the absence of an electric field (cf. Sec. 2.5).

The geometric parameters [cf. Fig. 5.11 (d)] are adapted from a LMA10 fiber, which means that the distance D of the capacitor plates is the fiber diameter without coating (125 µm) and the hole diameter equals the inclusion diameter of $d = 2.91\,\mu\mathrm{m}$.

The results of the simulations are shown in Fig. 5.12 . We plot the distributions of the refractive indices n_x and n_y inside the inclusions which follow from the calculated director field. As a measure of how the refractive indices are effected by the electric field, we calculated the refractive index averaged over the inclusion area. In the field off state ($V = 0$), which can also be derived analytically (cf. Sec. 2.5), the distributions of n_x and n_y [Fig. 5.12 (a, b)] are identical (apart from the rotation by $\pi/2$) as is expected from a radial symmetric director field. This is confirmed by the the averaged indices: $\bar{n}_x = \bar{n}_y = 1.584$.

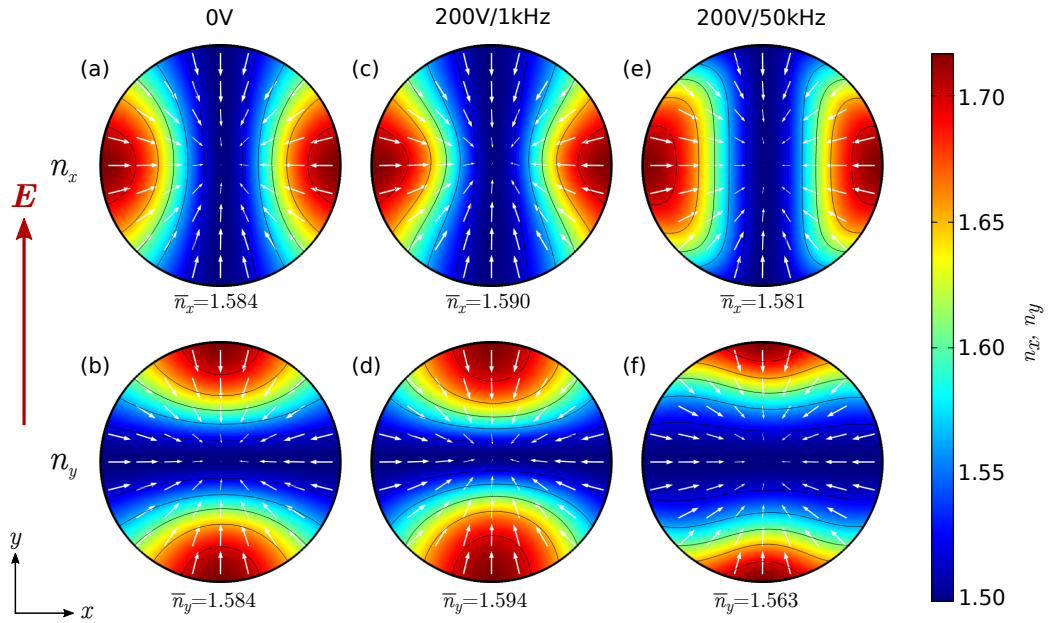

Figure 5.12. Simulation results of modeling a single liquid crystal inclusion with a radial escaped director field [cf. Fig. 5.11(d)] in a plate capacitor at (a, b) 0 V, (c, d) 200 V/1 kHz and (c, d) 200 V/50 kHz. The top row shows the refractive index in x direction, n_x. Bottom row shows n_y.

Under a low frequency voltage [200 V, 1 kHz, $\Delta\epsilon = +3.3$, Fig. 5.12 (c, d)] the director field becomes distorted whereas the LC molecules try to align parallel to the external electric field [red arrow in Fig. 5.12]. This reorientation increases both, n_x and n_y, by a small amount. The increase in $\bar{n}_y$ (= 1.594) is larger than the increase in $\bar{n}_x$ (= 1.590), since as the director orients mainly in the y-direction. Effectively, the director is rotated into the xy-plane by the electric field favoring the

y-direction.

The situation is fundamentally different for high frequency fields [200 volt, 50 kHz, $\Delta\epsilon = -3.3$, Fig. 5.12 (e, f)]. The LC molecules are now forced to be perpendicular to the electric field. This mainly affects molecules along the y-axis as those are initially parallel to the electric field and experience therefore the highest free energy due to the electric field. Their reorientation strongly decreases the average refractive index $\bar{n}_y$ to 1.563. This is a much stronger effect than the increase in $\bar{n}_y$, which we expect for low frequency fields with $\Delta\epsilon > 0$. Again, this reorientation affects also $\bar{n}_x$, which drops only slightly to 1.581, though. So, for high frequencies the director is effectively pushed out of the (x,y)-plane, again mainly affecting the y-component.

In summary, the application of low frequency electric field forces the director into the plane perpendicular to the fiber axis (z-axis). This increases both average refractive indices $\bar{n}_x$ and $\bar{n}_y$, in this plane. Conversely, a high frequency field rotates the director to be parallel to the fiber axis which then lowers the transverse (x and y) indices. Both effects are stronger for n_y than for n_x. We will use these theoretical expectations together with the ARROW model (Sec. 3.5.2.1) in order to understand the results of the experiments, which we will discuss in the next section.

5.3.2.2. Experimental results

For the experiments, we use a LMA10 fiber which is prepared to exhibit homeotropic anchoring as described in Sec. 5.2.2.2. The sample part exhibits a length of 5.5 cm which has been sandwiched between conducting ITO plates. In Fig. 5.13 (a), we show the transmission spectrum in the visible light of the prepared sample. Again, we observe the effects of the photonic band gap guiding mechanism, which leads to the formation of spectral transmission windows. Here, the measurement is shown for the vertical polarization, i. e. parallel to the direction of the external electric field.

In Fig. 5.13 (b), we focus on a single band gap and plot the influence of an external voltage. In the field-off state (black) the maximum of the band gap is centered at 690 nm. If we apply a voltage with at low frequency (1 kHz), the position of the maximum intensity shifts by ∼6 nm to longer wavelengths (red curve). In contrast, high frequency fields (50 kHz) lead to a blue shift of about 4 nm.

We can understand this behavior by remembering how the photonic bands which limit the spectral transmission windows (or photonic band gaps) form. In the ARROW model (Sec. 3.5.2.1) we interpreted the photonic bands as cladding modes at their cut-off which are in resonance with the core. This gave us a simple formula [Eq. (3.51)] to calculate the spectral positions of the photonic bands. Equation (3.51) already tells us that a change in refractive index n_{incl} leads to a change in resonance position: A increase of the refractive index results in a shift to longer wavelengths.

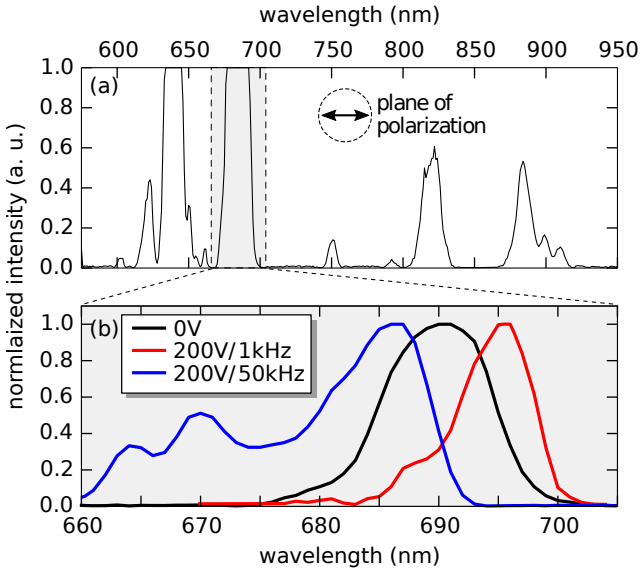

Figure 5.13. (a) White light transmission through a LMA10 fiber filled with homeotropically anchoring liquid crystal MLC2048. (b) Induced shift of a single band (around 690 nm) due to different external voltages/frequencies.

In Fig. 5.12 we have already shown that low frequency fields increase the transverse (xy-plane) refractive index and high frequency fields lower it. This is the actual effect behind the shift of the band gaps. In the discussion of Fig. 5.12, we distinguished between the refractive index in x-direction, n_x, and in y-direction, n_y. This, however, cannot be translated one-to-one to how light polarized along the x- or y-axis is affected because the inclusion modes are generally not linearly polarized and thus will be influence by both components of the refractive index.

Group delay

We now focus on the group delay and dispersion properties, which are displayed in Fig. 5.14. The general behavior of these properties is very similar to the observation for the axial aligned liquid crystal. In general, we were not able to obtain reliable results for the band gap at around 750 nm, due to the low intensity [cf. Fig. 5.13 (b)]. This band gap is therefore missing in Fig. 5.14.

For each band gap we performed three different measurements: in the field-off state, i. e. 0 V [black solid lines in Fig. 5.14 (a)], 200 V at 1 kHz (red lines) and 200 V at 50 kHz (blue lines). The polarization of light (x-direction) is perpendicular to the external electric field (y-direction). A general observation is that at low frequencies (1 kHz) the curves shift to longer wavelengths; at high frequencies (50 kHz), a shift to shorter wavelengths occurs. This fits with our qualitative discussion above, which was based on the director field simulations. The band gap at 825 nm could not be measured at 50 kHz. In fact, it seemed to have vanished as even at higher input power no transmission was measured.

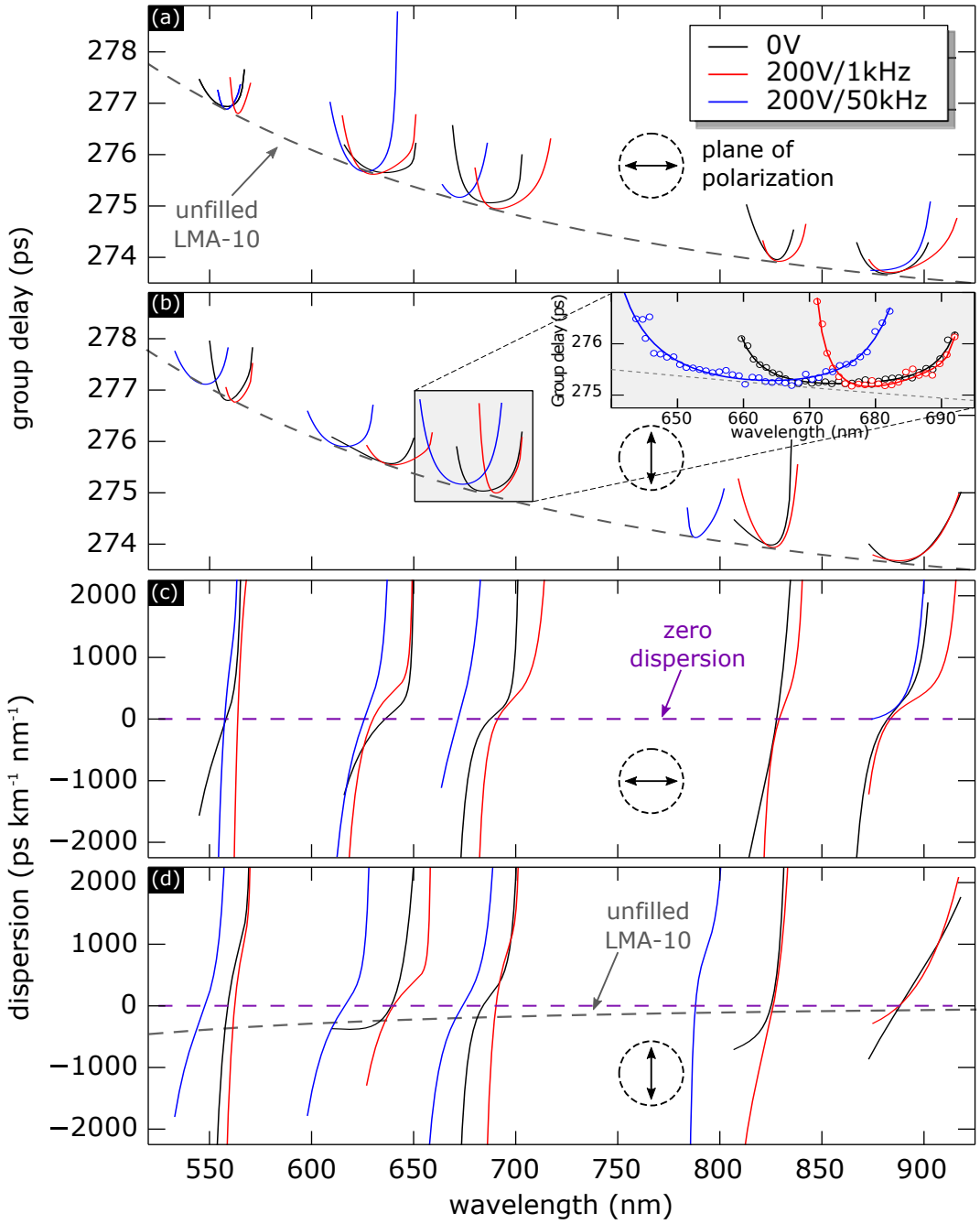

Figure 5.14. Measured group delay (a, b) in a LMA10 photonic crystal fiber filled with homeotropically aligned dual frequency liquid crystal MLC2048 at different externa lvoltages/frequencies. (a) Polarization of light is horizontal, i. e. perpendicular to the external electric field. As a reference, the group delay of an unfilled LMA10 is plotted (black dashed line). (b) Polarization of light is vertical, i. e. parallel to the external electric field. The inset shows the data points for a single band gap from which the fit is dervied. The fit is used to calculate the dispersion for the (c) horizontally and (d) the vertically polarized light. The purple dashed line in (c) marks the zero dispersion line. An empty (air filled) LMA10 (dashed black line) serves as a reference.

Besides the general trend of blue or red shift due to high and low frequency fields, there seems to be no overall trend of the magnitude of the shifts. This is probably

due to the cladding modes, which usually involve mode specific mixtures of x- and y-polarizations and thus react very differently to changes in the refractive indices.

In Fig. 5.14 (b) we plot the results of the group delay measurements for y-polarized light, i. e. the polarization direction coincides with the direction of the external field. For the field-off state, there are only minor differences for the group delays of the two orthogonal polarizations. No difference should be expected since the director field in the inclusions are rotational symmetric. But some deviations may be caused by the hexagonal structure of the PCF, which may lead to a small birefringence.

Under the influence of an applied voltage, we observe the same behavior for the y-polarized input as for the x-polarized light. The group delay is red shifted for low frequencies and blue shifted for high frequencies. The blue shift is larger for y-polarized light, though. This is in accordance with the conclusions we drew from the simulations discussed in Sec. 5.3.2.1. There, we saw that the refractive index in y-direction decreases much more compared to the x-direction (cf. Fig. 5.12).

We mentioned that the effect of the externel electric field can have very different effects on the band gaps due to the modal structure. The inset of Fig. 5.14 (b) confirms this expectation. There, we focus on the shifts of a single band gap and see that low frequency external field (red line) lead to a significant shrinking of the transmission. The opposite effect occurs for this band gap at high frequencies field. This is by no means a general observation, it varies strongly from band gap to band gap.

The shifts of the dispersion curves [Fig. 5.14 (c, d)] due to the applied electric field closely follow the shifts of the group delay. This is also true for the zero dispersion wavelengths, which we again observe for each transmission window.

5.3.3. Homeotropically aligned liquid crystals in hybrid PCFs

So far, we discussed two examples of liquid crystal filled photonic crystal fibers, for which all inclusions are filled with the liquid crystal. Both of the fibers uncovered the inherent problem of scattering losses due to the liquid crystal. A promising route to reduce the attenuation is to fill only a small amount of inclusions with the liquid crystal. This will lead to hybrid guiding fibers (HGF) [32, 150, 151]. We briefly introduced these fibers in Sec. 5.2.2.3. Now we will present some results on these fibers.

5.3.3.1. Design related attenuation of hybrid guiding fibers

We compare three different structures for the reduction of the attenuation (Fig. 5.15): the fully filled structure [FF, Fig. 5.15 (a)], which serves as a reference, the inner ring filled [IRF, Fig. 5.15 (b)] and the half line filled structure [HLF, Fig. 5.15 (c)]. We used a LMA10 fiber and prepared the structures as described in Sec. 5.2.2.3. Before the sealing of the inclusions, which should stay free of the LC, we functionalized the

inner surface by lecithin to achieve homeotropic anchoring. After the sealing, the fibers were filled with MLC2048. Finally, the fiber ends were cut-off to remove the parts filled with optical adhesive.

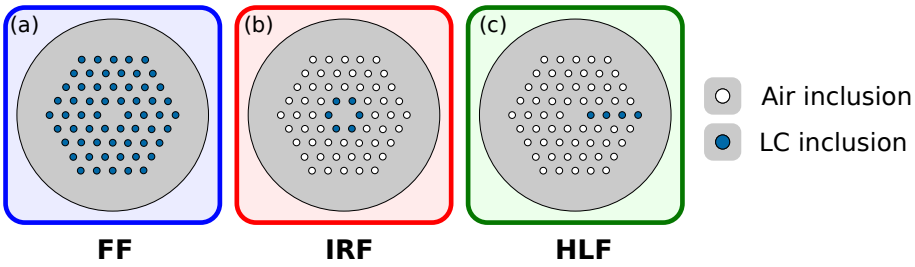

Figure 5.15. Schematic representation of photonic crystal fibers where different air holes have been infiltrated with liquid crystals. (a) A fully filled (FF) fiber, (b) a fiber with only its inner ring filled (IRF) and (c) a fiber with a half line filled (HLF).

We measured the attenuation of these fiber types via the cut-back method, which we already employed for the attenuation measurements of the microstructured fibers [cf. Sec. 4.2.4.2]. The fully filled structure exhibits the lowest attenuation within the spectral transmission windows (or band gaps). Its attenuation varies between 0.5 and 1 dB cm^{-1}. The attenuation inside the transmission windows decreases with increasing wavelength. This fits with the interpretation, that the main loss mechanism is due to scattering by the liquid crystal orientational fluctuations; the scattered intensity scales with λ^{-4} [46]. Naturally, the attenuation is highest between the band gaps, it exceeds 4 dB cm^{-1}, where the interaction of the core mode with the inclusions is the strongest.

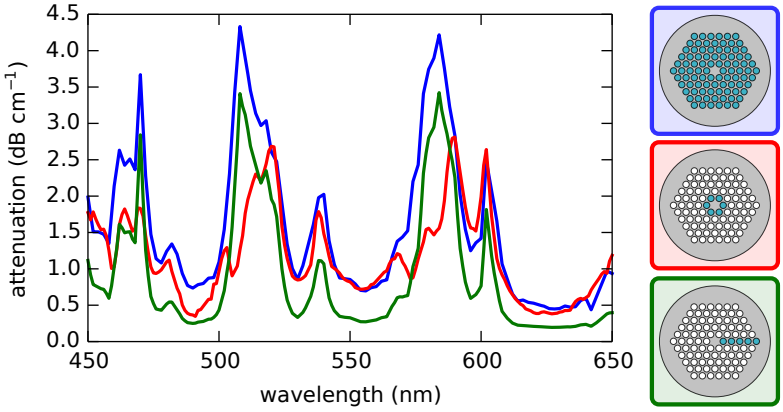

Figure 5.16. Measured attenuation spectra of the different fiber types with a schematic representation of the structure (right).

The inner ring filled structure shows a significantly smaller attenuation between the gaps compared to the FF type. But inside the band gaps the attenuation is almost identical. For the half line filled structure, the situation is somehow reverse: inside the band gaps, the attenuation is reduced to about one third of the FF or

IRF structures. Between the band gaps, however, the magnitude of the attenuation is closer to the one of the FF structure than the IRF fiber.

To explain this behavior, we carried out modal analyses of these fibers with the COMSOL FEM software package. For the simulations we used the LMA10 geometry, the properties of liquid crystal MLC2048 (Appendix A.3.4) and assumed homeotropic anchoring with $\sigma = 2.41$ The modal distributions of the normalized electric field are shown in Fig. 5.17 . We chose a wavelength (620 nm) very close to the edge of a transmission window. Consequently, we expect significant core-cladding interaction. We observe that for the FF fiber [Fig. 5.17 (a)] the core and the cladding exhibit a strong coupling. The resulting waveguide mode reaches far into the cladding, which leads high scattering loss and also confinement loss.[†]

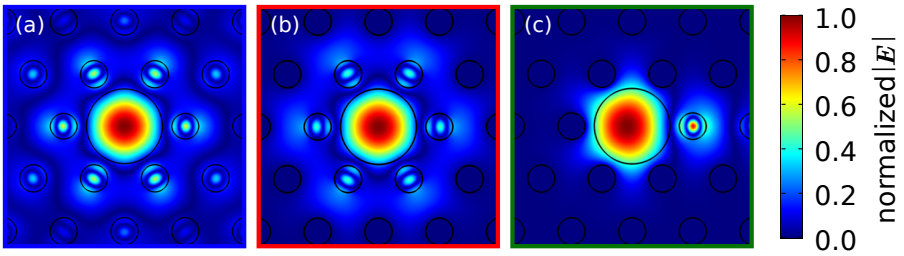

Figure 5.17. Results of the modal analysis with the finite element method for three fiber types: (a) Fully filled type, (b) inner ring filled type and (c) half line filled type. The surface plot shows the absolute electric field distribution.

The IRF structure [cf. Fig. 5.17 (b)] also exhibits strong coupling similar to the fully filled fiber. But the strong interaction is limited to the inner ring as only here adequate waveguide modes exist. This has two effects: first, the light is better confined compared to the fully filled type because beyond the first layer of LC inclusions the air filled inclusions confine light by modified total internal reflection. This reduces the confinement loss. And secondly, the scattering loss is reduced because only six LC inclusions are involved. This explains why the IRF type has lower loss between the band gaps. In the middle of the band gaps (or transmission windows) the attenuation of the IRF type is comparable to the FF type. This follows from the fact that the mode is well confined within the core and only interacts with the inner ring anyway. The LC inclusions deeper into the cladding do not play an important role for the IRF structure.

For the half line filled type [Fig. 5.17 (b)], if the interaction is strong between the core and the LC inclusion, light is efficiently transported out of the structure due to confinement loss. Therefore, the losses are quite high in these regions. In the middle of the transmission windows, the attenuation is drastically reduced as the interaction of core is limited to a single LC inclusion. However, intuitively we would assume a reduction in attenuation by a factor of six, the actual reduction is about

[†]We did not discuss the confinement loss in detail. It basically describes the loss which occurs due to the finite extent of the cladding. If the mode spreads out further than the cladding structure, the confinement due to the band gaps is no longer given and power is lost.

a factor of three. By comparing the Fig. 5.17 (a-c), we observe that the interaction with the single inclusion of the HLF fiber is stronger than the interaction with the inclusions of the FF and the IRF structures.

In practice, we will always try to operate in the middle of a band gap because there the loss is minimal in any case. Therefore, we prefer the half-line filled structure over the ring filled structure for the following measurements. We are aware that a structure with only a single filled inclusion would provide low attenuation over the whole spectrum. But as it turned out, such a fiber is to delicate to produce with the simple method we are using.

5.3.3.2. Group delay and dispersion of hybrid guiding fibers

For the experiments on the hybrid guiding fibers, we use a LMA8 fiber ($d = 2.58\,\mu m$, $\Lambda = 5.61\,\mu m$) treated with lecithin for homeotropic anchoring and then selectively closed with the method described above (Sec. 5.2.2.3). The investigated sample below has an overall length of 8.6 cm. We restrict ourselves to the discussion of the case where the input polarization is parallel to the external electric field.

From the transmitted intensity in Fig. 5.18 (a), we directly observe that even narrow photonic band gaps show high transmission. We were also able to record a band gap in the blue wavelength region (∼480 nm) rather close to the emission spectrum edge of the supercontinuum source. The enhancement of the transmission properties also becomes clear when we compare the transmission spectrum in Fig. 5.18 (a) with the spectra of the fully filled LMA8 in Fig. 5.10 (a) and LMA10 in Fig. 5.13 (a). The spectral transmission windows of the hybrid guiding fiber are much broader and more homogeneous in intensity.

We were able to perform the group delay measurements for all transmission windows, which was not possible for the fully filled fibers. This includes the measurements performed under applied voltages at low (1 kHz) and high (50 kHz) frequency fields. Here, we limit ourselves to the visible wavelength range and only consider the electrooptic effects on y-polarized light, i. e. polarized parallel to the external electric field.

The group delay [Fig. 5.18 (b)] a red shift under low frequencies and a blue shift under high frequencies. The explanation is the same as for the fully filled fibers. The band gap centered around 675 nm seems to be an exception from this rule. This might be caused by the complicated structure of the cladding modes under the influence of a voltage. Naturally, we observe a similar behavior for the dispersion [Fig. 5.18 (c)]. Each of the dispersion curves crosses the zero dispersion line which is an indicator for us that four-wave mixing might be possible in the visible range. We explore this option in the following section by calculating the phase matching curve.

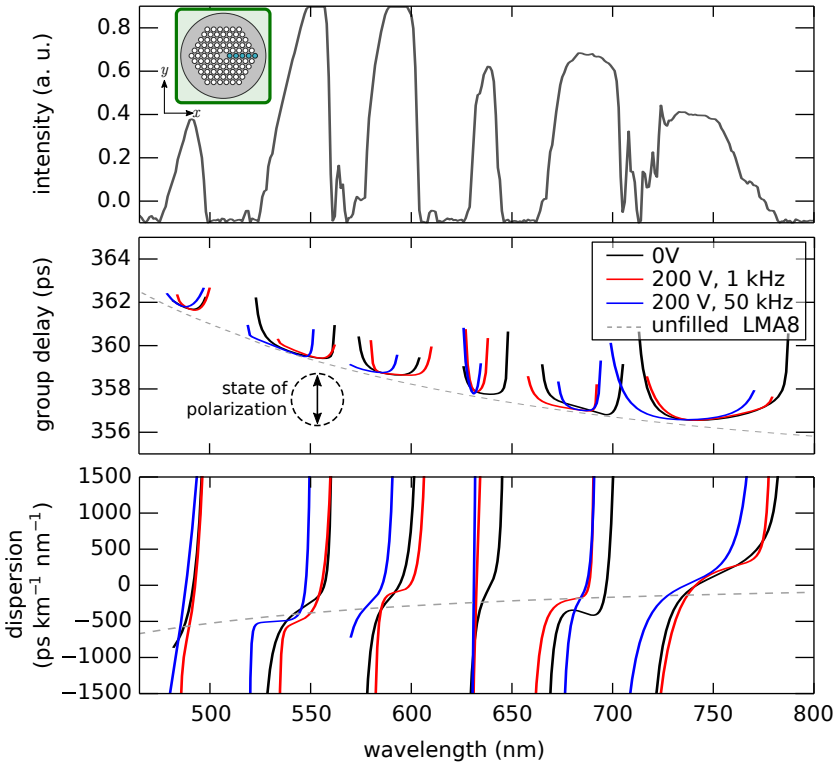

Figure 5.18. (a) Measured white light transmission spectrum of a LMA8 fiber in which only a half line is infiltrated with the liquid crystal MLC2048 (cf. inset). (b) Fits to the measured group delay of the fiber. The polarization of light is parallel to the external electric field. (c) Dispersion derived from the fits to the group delay in 8(b). In (b) and (c) the values for an empty (air filled) LMA8 (dashed gray line) is plotted as a reference.

5.3.4. Phase matching in hybrid guiding fibers

For calculation of the phase matching [cf. Eq. (3.59)], the values for the propagation constants β have to be known. We saw in Fig. 5.3 (a) that the effective refractive index $n_{\text{eff}} = \beta/k$ is discontinuous. Thus, we cannot expand it in a Taylor series as we did when we introduced the phase matching in Sec. 3.7.2. For the calculation of the phase matching curves from the experimental results of the group delay we therefore use simulated data for reference. For each band gap we have to assign a reference wavelength, for which we extract the propagation constant.

This procedure introduces some errors because the simulations do not precisely match the actual recorded spectra of the group delay. Nevertheless, as we only need one reference value for each band gap, we can choose the middle of a band gap where the waveguide effects are minimized. In Fig. 5.19 we show the group velocity we measured together with the simulated data. We marked the hand-picked wavelengths which serve us as a reference for the calculations of the propagation constants.

If we designate β_0^{BG} as the reference value for the propagation constant per transmission window, we can determine the propagation constant for the transmission

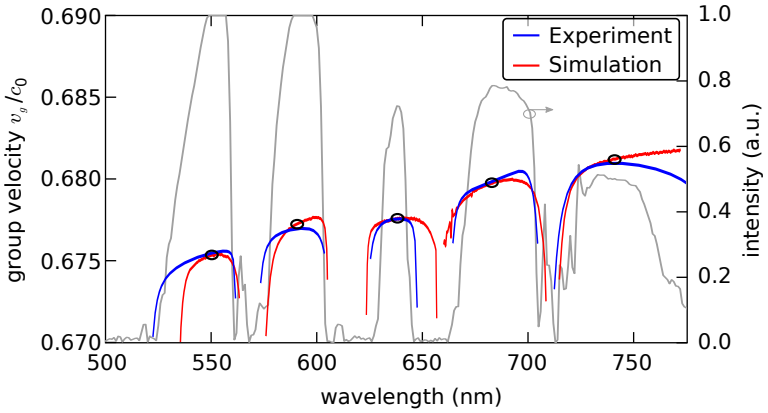

Figure 5.19. Comparison of the group velocity measured in the experiment with the simulated data. The wavelength positions which will serve as a reference for the calculation of the propagation constant are marked (black circles). The simulations were performed for a LMA8 structure selectively filled with MLC2048 under homeotropic anchoring with $\sigma = 2.41$ assumed.

windows by

$$\beta^{\mathrm{BG}}(\omega) = \beta_0^{\mathrm{BG}} + \int_{\omega_0}^{\omega} v_{\mathrm{g}}^{-1}(\omega')\,\mathrm{d}\omega'.$$

For simplicity, we perform the numerical integration in the frequency space. We display the results in Fig. 5.20. For better visibility we plot the effect refractive index in (a) instead of the propagation constant ($\beta = 2\pi n_{\mathrm{eff}}/k$). As references we plotted the effective indices of pure silica and of an empty (air filled) LMA8 fiber. The refractive index of the hybrid guiding fiber is very similar to the LMA8. Noticeable differences can be seen close to the edges of the transmission window as is expected from the group delay curves.

To make these differences more apparent, we plot the difference between the effective indices and the refractive index of silica for the HGF (red) and the LMA8 (black) in Fig. 5.20 (b).

With these results we can calculate the phase matching curves, which are shown in Fig. 5.21 (a-c) for the three different cases: 0 V, 200 V at 1 kHz and 200 V at 50 kHz. We are only considering here the case where pump, signal and idler share the same polarization, namely parallel to the external electric field (y-direction). The plots on the left side show the white light transmission spectrum in the range between 620 nm to 780 nm in order to estimate whether the four wave mixing process for the given signal/idler wavelengths is sensible.

For the calculation of the actual phase matching curves [right in Fig. 5.21] we include the self-phase modulation, thus the phase matching condition reads [134]

$$0 = 2\beta_{\mathrm{p}} - \beta_{\mathrm{s}} - \beta_{\mathrm{i}} - 2\gamma P \tag{5.2}$$

where the non-linear coefficient is set to $\gamma = 3.9\,\mathrm{W}^{-1}\,\mathrm{m}^{-1}$ [152] and the pulse peak

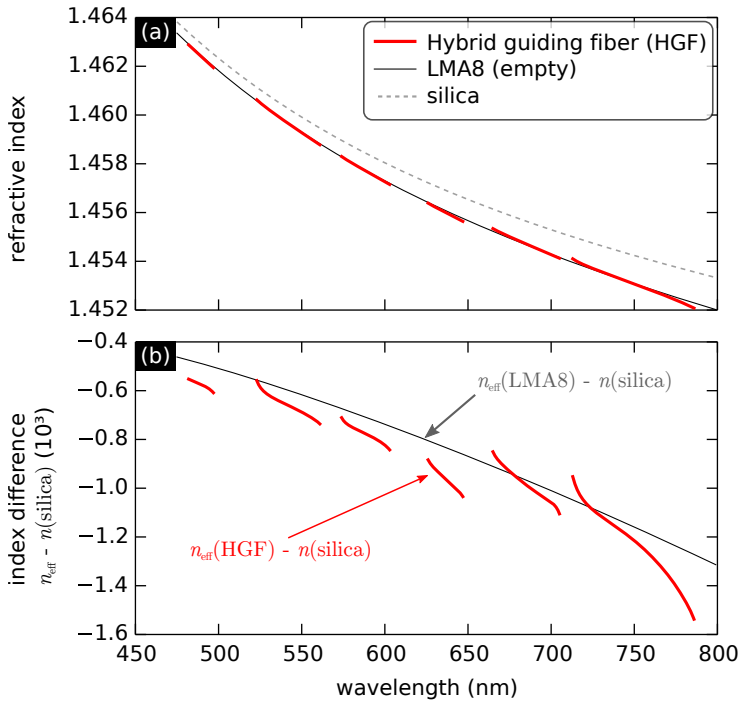

Figure 5.20. (a) Approximate effective refractive index of the core mode (solid red line) calculated from the experimental data for the group velocity in the field-off state. As a reference, the unfilled LMA8 (solid black line) and bulk silica (dashed gray line) are plotted as well. (b) The difference between the selectively filled LMA8 and the bulk silica (solid blue line) is shown. The empty LMA8 (solid black line) again serves as a reference.

power to $P_\mathrm{p} = 100\,\mathrm{W}$. Here, we assume that the non-linearity of silica is driving the process and not the liquid crystal.

The positions where the pump wavelengths match the signal and idler, i. e. $\omega_\mathrm{p} = \omega_\mathrm{s} = \omega_\mathrm{i}$, wavelength are marked with a green dashed line. The self-phase modulation caused by the strong pump power leads to phase matching very close to the pump pulse. For $P_\mathrm{p} \to 0$ these would not exist. The signal and idler generated very close to the pump are usually only of little interest because due to the small spectral separation they are hard to isolate.

In the field-off state [Fig. 5.20 (a)] we observe multiple wavelengths at which the phase matching (solid black line) is fulfilled. We can separate those in two regions: The first region is located at a pump wavelength of around 685 nm, the second region is around 720 nm. This already proves to be very different from standard optical fibers and photonic crystal fibers, which show phase matching only in the infrared.

In the first case, pump, signal and idler occur in different band gaps. In the second case, pump and idler occupy the same band gap. In both cases, the signal and idler are well isolated (each about $\sim 40\,\mathrm{nm}$) from the pump.

Let us consider one example for the FWM process. If we pump at 680 nm (solid green line in Fig. 5.21 (a)), signal and idler will then be generated at 641 nm and 724 nm. All involved photons are located in a region where the intensity of the

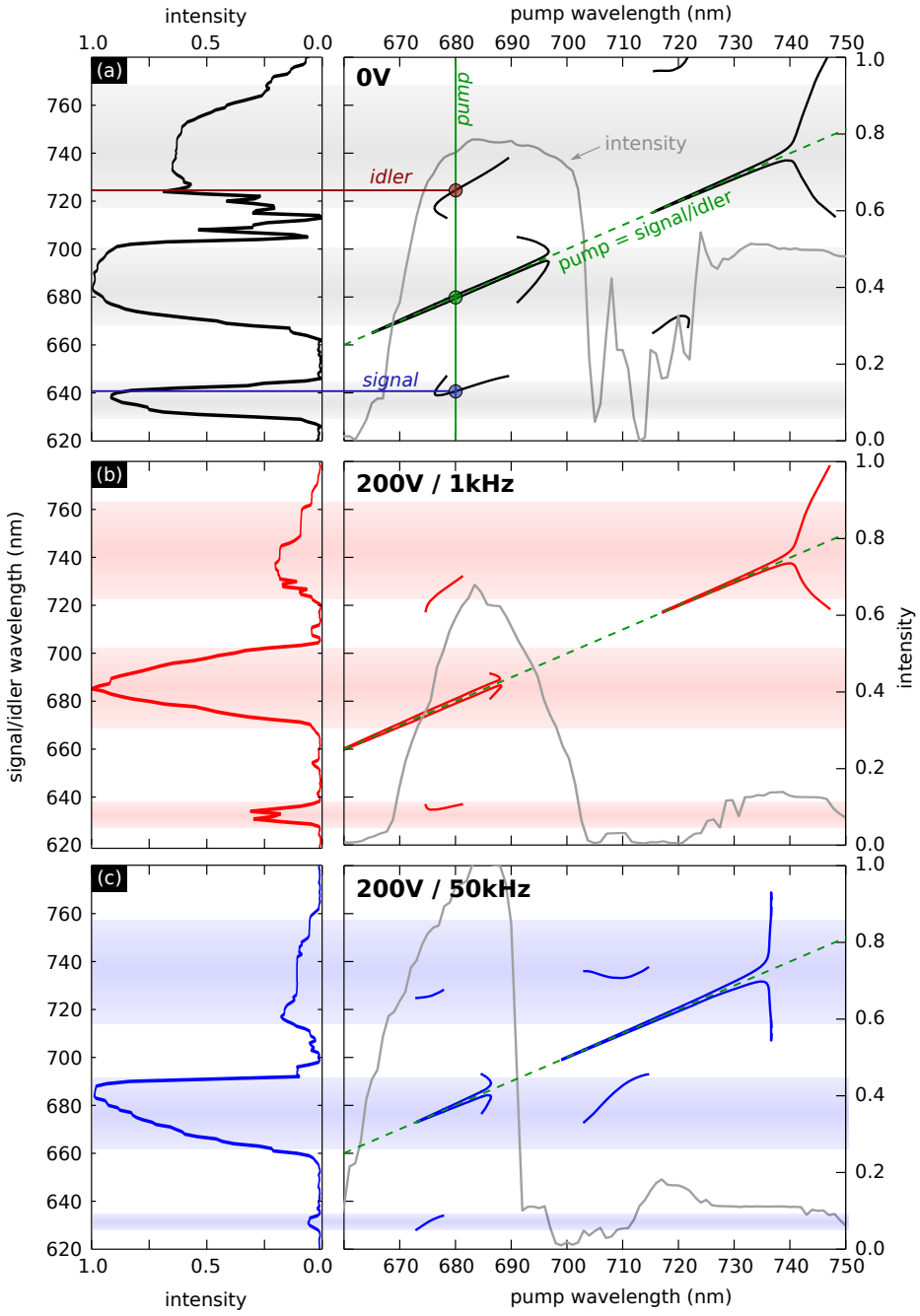

Figure 5.21. Theoretical phase matching curves (right column) at different voltages/frequencies calculated on the basis of the reconstructed effective refractive indices: (a) field-off state, i. e. 0 V, (b) 200 V/1 kHz and (c) 200 V/50 kHz. The dashed green line shows gives the line where pump, signal and idler have identical wavelengths. The gray curve gives the white light transmission over the investigated pump range. The left columns show the white light transmission over the range investigated for signal and idler. This extended to the right side by the shading. In (a) an example for the four wave mixing process is indicated: The pump at 640 nm (solid green line) generates signal (blue) and idler (red).

transmitted light is relatively high, thus pumping at 680 nm would be a reasonable choice.

We further observe that if the phase matching is fulfilled, at least one of the photons (pump, signal or idler) is located close to a band gap. This is sensible because in the middle in the transmission windows the influence of the waveguide structure is minimal and the optical properties are dominated by the bulk material. But for the silica material we already know that phase matching is only possible in the infrared.

Under the application of an external voltage [200 V at 1 kHz, Fig. 5.21 (b)], we see that phase matching around 680 nm becomes much smaller and is shifted to shorter wavelengths. This pushes the possible generation of signal and idler to the edges of the transmission windows, which would result in high scattering losses. The second phase matching region, which we observed around 720 nm in the field-off state, vanishes under the application of a low frequency voltage.

This is very different for the high frequency voltage [200 V at 50 kHz, Fig. 5.21 (c)]. The phase matching region [solid blue line] has blue shifted from 720 nm to around 710 nm and is almost twice as broad but the separation of pump and signal/idler has decreased. Despite the smaller spectral distance, an efficient FWM process now seems much more likely compared to the field-off state because signal and idler are located much closer to the center of the transmission windows which will lead to lower losses.

Chapter 6

Conclusion & Outlook

6.1. Conclusion

In this thesis we discussed the combination of optical fiber with liquid crystals (LCs). We employed two different types of fibers: microstructured optical fibers (MOFs) and photonic crystal fibers. In both fibers light is guided within the solid core. The liquid crystal is used to modulate the waveguiding properties of these fibers by external electric fields. We studied different properties depending on the fiber type: In the MOFs we looked at the basic interaction of the waveguiding core the the liquid crystal and and were finally interested in the attenuation of the core mode caused by the presence of the LC. In the PCFs, however, we investigated the propagation of optical pulses. In particular, we measured the group delay and dispersion.

The structure of the MOFs used in this work is particularly simple: It consists of a single high index glass core and a hollow inclusion running parallel to the core. Core and inclusion are in the micrometer range and share a silica cladding. We infiltrated the hollow inclusion with a liquid crystal via capillary forces. The LC was anchored axially, which made the inclusion to a uniaxial waveguide. We studied the interaction between core and inclusion by launching light into the glass core and recorded the attenuation and the transmission as the function of the voltage. We showed that this structure can be described accurately as a system of two coupled dissimilar waveguides using the coupled mode theory (CMT).

In the experiments without an external electric field, we found regions of high attenuation, which we could identify using the CMT as resonances between core and inclusion modes. In these resonance, optical power is transferred from the core to the inclusion. The optical power in the inclusion mode is scattered by the LC, which leads to the high attenuation. The CMT further predicted that for higher order modes in the inclusions the losses become polarization dependent. We found this result confirmed by our experiments.

We used two different fibers with slightly different geometries which made them

suitable either for the visible (VIS) or the near infrared (NIR) wavelength regime. Both fiber showed very low attenuation ($< 0.2\,\mathrm{dB\,cm^{-1}}$) away from the resonant regions. In the visible regime, if efficient coupling between core and inclusion occurs, the associated attenuation was as high as $5\,\mathrm{dB\,cm^{-1}}$. For IR region, we detected no attenuation due to resonant coupling in the field-off state.

In the field-on state, both fiber types exhibited strong polarization dependent losses. We quantified this by calculating the polarization extinction. This quantity was as high as $5\,\mathrm{dB\,cm^{-1}}$ over a range of 100 nm in the visible and over 250 nm in the NIR range. We reasoned that this strongly anisotropic attenuation originates from the appearance of multiple new modes in the inclusion due to the reorientation of the LC. These new modes are mainly polarized along the direction of the external electric field and therefore light with the same polarization direction is attenuated predominantly. The recorded switching times are in the single digit millisecond regime.

We can conclude that these microstructured optical fibers filled with liquid crystal make good candidates for electrically controlled integrated polarization switches. Especially the fiber design for the infrared is promising as it shows a high transmission in the field-off state and a broadband polarization extinction under the influence of an external electric field.

From the microstructered optical fibers (MOFs) we moved to photonic crystal fibers (PCFs). In the PCF structure we have multiple inclusions arranged into an hexagonal lattice within a silica background material. The waveguiding core is formed by a missing inclusion. Again, we infiltrated the inclusions with a liquid crystal. The light guiding in the liquid crystal filled photonic crystal fibers (LCPCFs) is facilitated by photonic band gaps originating from the periodic cladding. The band gap guiding mechanism lead to the appearance of spectral transmission windows.

We investigated the group velocity and the dispersion in these fibers. We started out with an axially aligned liquid crystals and obtained strongly bent dispersion curves in the field-off state. For each of the transmission windows, we found a zero dispersion wavelength (ZDW), which is a unique property of photonic band gap fibers. However, under the application of an external electric field the discontinuous Fréedericksz-like transition of the director field did not provide us with reliable measurements.

Consequently, we moved to a homeotropically aligned liquid crystal, which enabled use to continuously tune the transmission windows and the group delay dispersion. By using a dual frequency LC we were able to show that a blue or a red shift of the ZDWs can occur depending on the frequency of the applied external voltage. With this method, we could shift the ZDWs by up to 30 nm. We presented a simplified model to simulate the effects of the external electric field on the LC director configuration. From this model we were able to explain the origin of the observed shifts.

In a final experiment, we were able to reduce the scattering losses in the LCPCF from $1\,\mathrm{dB\,cm^{-1}}$ to $0.3\,\mathrm{dB\,cm^{-1}}$. We achieved this reduction by filling only a part of the PCF with liquid crystals resulting in hybrid guiding fiber. Based on the experimental results for the group velocity and the dispersion in these fibers, we calculated the phasematching curves with and without external electric fields. With these results we were able to show theoretically that four wave mixing in these fiber is possible in the visible range. And that it can be tuned by external electric fields.

6.2. Outlook

From the conclusion above, we can derive some prospects for future work on microstructured optical fibers (MOFs) and photonic crystal fibers (PCFs) filled with liquid crystals. For both structures an axially aligned nematic liquid crystal is not ideal for electrooptic swichting as it is discontinuous. We discussed this switching process qualitatively and compared it to a Fréedericksz transition in planar cells. In the case of the LCPCFs we circumvented this switching mechanism by using a homeotropically aligned liquid crystal, which facilitated continuous tuning. But this came at the cost of more complicated modeling of the director field.

Another solution to this problem, which we are pursuing at the moment, is to use other liquid crystalline phases such as ferroelectric liquid crystals (FLCs) or blue phase (BP) liquid crystals. These two candidates show a continuous response to external electric fields, which would be much more favorable for applications. However, both of these phases are more complicated to handle in practice.

In the case of FLCs, the alignment inside the capillaries is the most challenging task as the axial alignment is not energetically favored. The axial alignment has to be enforced by the boundary conditions, for which we are currently using the photoalignment technique, which we used for the LCPCFs.

By now, we have succeeded to infiltrate PCFs with blue phases and to show their continuous switching under an electric field [113]. However, BPs only exist in a narrow temperature range of only a few Kelvin. A solution to this problem is polymer stabilization [153], which has been successfully applied to LC cells. We adapted this process and achieved polymer stabilized blue phases in a single microcapillary. Currently we are working on applying this procedure to MOFs and PCFs.

The combination of a microstructured optical fiber with a continuously tunable liquid crystal (FLC or BP) has the potential for electrically addressable polarization filters. They provide low loss ($< 0.1\,\mathrm{dB\,cm^{-1}}$ [154]) in the non-resonant regions, therefore have an advantage over LCPCFs.

The fiber can also be used to mediate the interaction between two glass cores if a liquid crystal inclusion is added, which is between these cores. These structures could serve as an electrically switchable fiber coupler. Or the LC inclusions can

be incorporated in fibers which contain multiple functional elements, which were proposed quite recently [155].

The next step for the liquid crystal photonic crystal fibers is the experimental verification of the four wave mixing process in the hybrid guiding fiber. For this purpose, polymer-stabilized blue phases should be the preferred liquid crystal material. It allows for continuous tuning, and the theoretical description is simple as BPs are isotropic in the field-off state. The behavior under voltage can be described by the Kerr effect.

To conclude, within this thesis we described the basic interaction between glass waveguides and liquid crystal waveguides. We explored the polarizing capabilites in the linear optical regime with the microstructured optical fibers and have glanced into the non-linear optical regime in the context of the photonic crystal fibers. This, together with the ideas on the incorporation of different liquid crystalline phases, should serve a starting point for the application of liquid crystal infiltrated optical waveguides.

Chapter 7

Acknowledgements

Over the last couple of years a lot of people helped me to finish my thesis in one way or the other. So now is the time to thank them. I apologize in advance for the ones I forgot to mention in the following.

First, I would like to thank Prof. Heinz Kitzerow for taking me on as a PhD student and providing me with such an interesting and challenging topic. I always had the possibility to explore my own ideas and numerous occasions to present the results of my work on conferences. Both I do not take for granted.

I thank Prof. Christine Silberhorn for taking the time to be on the dissertation committee and to work through my thesis.

The microstructured fibers we used for this work came from the Max Planck Institute for the Science of Light in Erlangen. I would like to thank Prof. Markus A. Schmidt and Prof. Philip Russell for providing these fibers and for the feedback on the related publication.

I am glad that Alex Lorenz employed me as a student helper since my early years as a bachelor student. He introduced me to liquid crystals and photonic crystal fibers and endured my first miserable attempts in handling optical fibers.

A good working atmosphere is always a result of good colleagues. So I thank Martin Urbanski, who gave me some good advice for my work and performed a couple of experiments for the characterziation of liquid crystals. Andreas Hoischen for sharing some insider knowledge about the lab equipment and for always being available to take a look at broken devices. Bernhard Atorf, Gaby Nordendorf and Bingru Zhang for being such good lab neighbors.

Special thanks to Isabella Koralewicz, who took care of most of the paperwork.

No experiment runs if there is nothing to experiment with, so a big thank you goes to Susanne Keuker-Baumann, Rita Egert-Tiesbohnenkamp and Gilla Jünnemann-Heldt. They kept track of the chemicals and kept many devices running. The latter also includes the coffee machine.

Through the year I had a couple of students working for me. Amazingly they

did not become bitter over my jabbering. Therefore, my respect goes out to Justus Ebel, Tarik Rust and Steffen Knust.

Finally, I thank Katharina Brassat for proof reading my thesis and giving frank and helpful advice. She kept me on track and was always willing to shoot down (at least some of) my stupid ideas.

Chapter A

Appendix

A.1. Refractive indices of silica and Germanium doped silica

The refractive n index of silica is given by the Sellmeier formula [156]

$$n^2 - 1 = \sum_{k=1}^{3} \frac{S_k \lambda^2}{\lambda^2 - \lambda_{S,k}^2}, \tag{A.1}$$

where S_k and $\lambda_{S,k}$ are silica specific material parameters and λ is the wavelength. For germanium doped silica, a different relation is approximately valid, which include the mole-doping fraction X [157]

$$n^2 - 1 = \sum_{k=1}^{3} \frac{\left[(1-X)S_k + XG_k\right] \lambda^2}{\lambda^2 - \left[(1-X)\lambda_{S,k} + X\lambda_{G,k}\right]^2}, \tag{A.2}$$

where $\lambda_{S,k}$ are Germanium specific material parameters. Obviously, by setting $X = 0$ in Eq. (A.2) we obtain Eq. (A.1). The material specific parameters are given in Tab. A.1.

Table A.1. Material coefficients for silica [156] and germanium [157].

k	S_K	$\lambda_{S,k}$	G_K (μm^{-2})	$\lambda_{G,k}$ (μm^{-2})
1	0.69616630	0.06840430	0.80686642	0.068972606
2	0.40794260	0.11624140	0.71815848	0.15396605
3	0.89747940	9.8961610	0.85416831	11.841931

A.2. Refractive index measurements

A.2.1. Refractometer

The wavelength dependence of the employed liquid crystals have been measured with a Jelly microrefractometer [Fig. A.1]. The glass wedge cell is rubbed 200 times along the z direction to achieve a good alignment for the liquid crystal. From the angles ϑ_e and ϑ_o the extraordinary refractive index n_e and the ordinary refractive index n_o can be calculated by

$$n = \sin\vartheta + \left(n_\mathrm{w}^2 - \sin^2\vartheta\right)^{\frac{1}{2}} \tag{A.3}$$

where $n = \{n_\mathrm{e}, n_\mathrm{o}\}$, $\vartheta = \{\vartheta_\mathrm{e}, \vartheta_\mathrm{o}\}$ and n_w is the refractive index of the wedge cell.

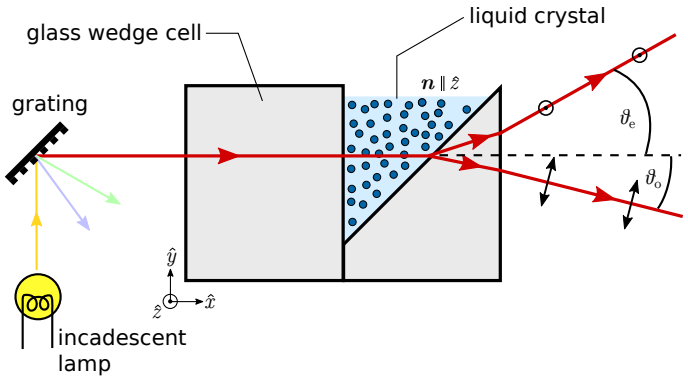

Figure A.1. Setup to measure the wavelength dependence of the refractive index of liquid crystals. An incadescent lamp emits a broad optical spectrum, from which the wavelengths are selected with a grating monochromator. The monochromatic light passes through a wedge cell which contains a well oriented liquid crystal sample. The different refractive indices, n_e and n_o, lead to different refraction angles ϑ_e and ϑ_o.

A.2.2. Cauchy fit

In order to be able to determine the refractive index for an arbitrary wavelength, a Cauchy fit according to

$$n(\lambda) = A_0 + A_1\lambda^{-2} + A_2\lambda^{-4} \tag{A.4}$$

is used to interpolate the refractive indices. The coefficients A_0, A_1 and A_2 are found by a least squares fit. For these fits, the wavelength is usually rescaled to micrometer, thus the dimensions of A_1 and A_2 are $[A_1] = \mu\mathrm{m}^{-2}$ and $[A_2] = \mu\mathrm{m}^{-4}$, respectively.

A.3. Liquid crystal mixtures

A.3.1. E7

Table A.2. Physical properties of liquid crystal E7 [135].

Description	Symbol	Value
Transition temperature nematic isotropic	$T_{\text{N-I}}$	58 °C
Dielectric permittivities (20 °C, 1 kHz)	$\epsilon_\perp$	5.2
	$\epsilon_\parallel$	19.0
Dielectric Anisotropy (20 °C, 1 kHz)	$\Delta\epsilon$	+13.8
Refractive indices (20 °C, 589 nm)	n_{o}	1.5222
	n_{e}	1.7390
Optical Anisotropy (20 °C, 589 nm)	Δn	0.2670
Elastic Constants (20 °C)	K_{11}	10.8 pN
	K_{22}	6.5 pN
	K_{33}	17.5 pN

Table A.3. Cauchy coefficient by least squares fit.

Description	A_0	A_1 (µm^{-2})	A_2 (µm^{-4})
ordinary refractive index	1.499	0.720×10^{-2}	0.3×10^{-3}
extraordinary refractive index	1.693	0.780×10^{-2}	2.8×10^{-3}

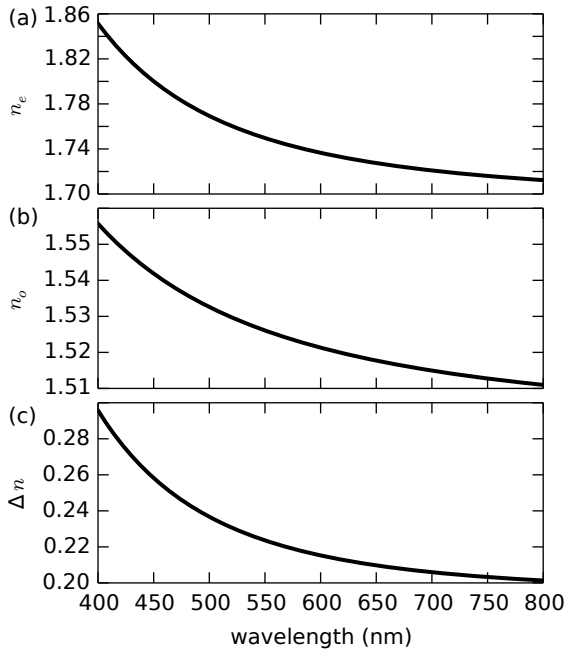

Figure A.2. Refractive indices of E7 vs. wavelength: (a) Extraordinary refractive index, (b) ordinary refractive index and (c) optical anisotropy.

A.3.2. BL036

Table A.4. Physical properties of liquid crystal BL036 [135].

Description	Symbol	Value
Transition temperature nematic isotropic	$T_{\text{N-I}}$	95 °C
Dielectric permittivities (20 °C, 1 kHz)	$\epsilon_\perp$	6.1
	$\epsilon_\parallel$	23.1
Dielectric Anisotropy (20 °C, 1 kHz)	$\Delta\epsilon$	+17.0
Refractive indices (20 °C, 589 nm)	n_o	1.5270
	n_e	1.7940
Optical Anisotropy (20 °C, 589 nm)	Δn	0.2670
Elastic Constants (20 °C)	K_{11}	15.1 pN
	K_{33}	27.0 pN

Table A.5. Cauchy coefficient by least squares fit.

Description	A_0	A_1 (µm^{-2})	A_2 (µm^{-4})
ordinary refractive index	1.513	0.419×10^{-2}	0.367×10^{-3}
extraordinary refractive index	1.733	1.372×10^{-2}	2.540×10^{-3}

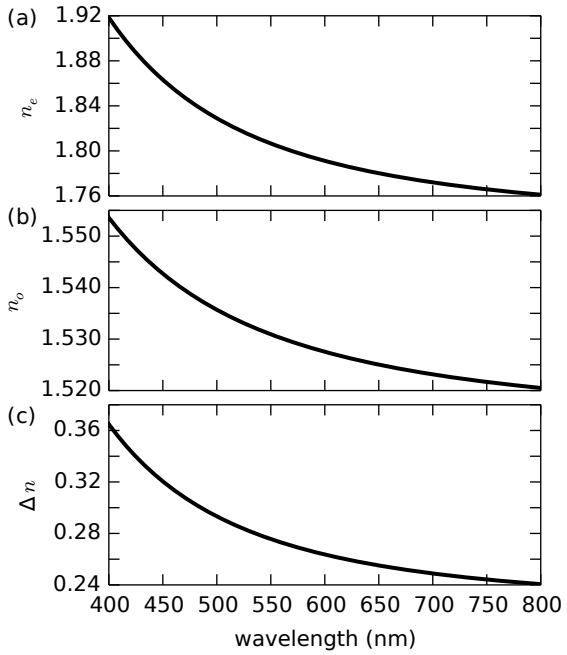

Figure A.3. Refractive indices of BL036 vs. wavelength: (a) Extraordinary refractive index, (b) ordinary refractive index and (c) optical anisotropy.

A.3.3. MLC2103

Table A.6. Cauchy coefficient by least squares fit.

Description	A_0	A_1 (µm^{-2})	A_2 (µm^{-4})
ordinary refractive index	1.472	0.151×10^{-2}	-0.474×10^{-4}
extraordinary refractive index	1.538	0.611×10^{-2}	-3.770×10^{-4}

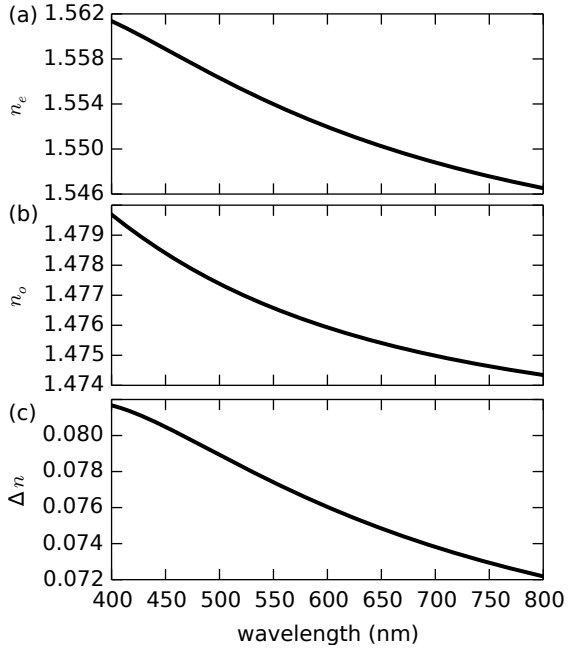

Figure A.4. Refractive indices of MLC2103 vs. wavelength: (a) Extraordinary refractive index, (b) ordinary refractive index and (c) optical anisotropy.

A.3.4. MLC2048

Table A.7. Physical properties of liquid crystal MLC2048. [158]

Description	Symbol	Value
Transition temperature nematic isotropic	$T_{\text{N-I}}$	110 °C
Dielectric Anisotropy (20 °C, 1 kHz)	$\Delta\epsilon$	+2.84
Dielectric Anisotropy (20 °C, 50 kHz)	$\Delta\epsilon$	-2.99
Refractive indices (20 °C, 589 nm)	n_{o}	1.4980
	n_{e}	1.7164
Optical Anisotropy (20 °C, 589 nm)	Δn	0.2184
Elastic Constants (20 °C) [159]	K_{11}	12.4 pN
	K_{22}	10.1 pN
	K_{33}	24.7 pN

Table A.8. Cauchy coefficient from by least squares fit.

Description	A_0	A_1 (µm^{-2})	A_2 (µm^{-4})
ordinary refractive index	1.472	0.903×10^{-2}	0
extraordinary refractive index	1.660	1.961×10^{-2}	0

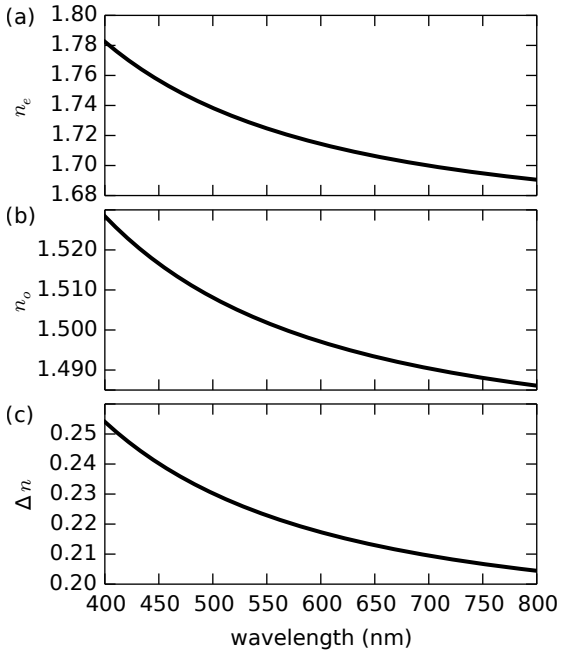

Figure A.5. Refractive indices of MLC2048 vs. wavelength: (a) Extraordinary refractive index, (b) ordinary refractive index and (c) optical anisotropy.

Chapter B

Bibliography

[1] D. R. Goff, K. S. Hansen, and M. K. Stull, *Fiber Optic Video Transmission: The Complete Guide* (Focal Press, 2003).

[2] F. P. Kapron, "RADIATION LOSSES IN GLASS OPTICAL WAVEGUIDES," Appl. Phys. Lett. **17**, 423 (1970).

[3] D. Gloge, "Optical waveguide transmission," Proc. IEEE **58**, 1513–1522 (1970).

[4] D. Gloge, "Weakly guiding fibers." Appl. Opt. **10**, 2252–8 (1971).

[5] D. Gloge, "Dispersion in weakly guiding fibers." Appl. Opt. **10**, 2442–5 (1971).

[6] D. Marcuse and R. M. Derosier, "Mode Conversion Caused by DIameter Changes of Round Dielectric Waveguide," Bell Syst. Tech. J. **48**, 3217 (1969).

[7] D. Marcuse, "Pulse distortion in single-mode fibers. Part 2." Appl. Opt. **20**, 2969–74 (1981).

[8] D. Marcuse, *Theory of dielectric optical waveguides* (Acad. Press, Boston, 1991).

[9] A. W. Snyder, "Asymptotic expressions for eigenfunctions and eigenvalues of a dielectric or optical waveguide," Microw. Theory Tech. IEEE Trans. **17**, 1130–1138 (1969).

[10] A. W. Snyder and D. J. Kinsley, "Excitation and Scattering of Modes on a Dielectric or Optical Fiber," IEEE Trans. Microw. Theory Thechniques **17**, 1138–1144 (1969).

[11] A. W. Snyder, "Continuous Mode Spectrum of a Circular Dielectric Rod," IEEE Trans. Microw. Theory Tech. **19**, 720–727 (1971).

[12] J. C. Knight, T. A. Birks, P. S. J. Russell, and D. M. Atkin, "All-silica single-mode optical fiber with photonic crystal cladding," Opt. Lett. **21**, 1547 (1996).

[13] J. C. Knight, T. A. Birks, P. S. J. Russell, and D. M. Atkin, "All-silica single-mode optical fiber with photonic crystal cladding: errata." Opt. Lett. **22**, 484–5 (1997).

[14] E. Yablonovitch, "Inhibited Spontaneous Emission in Solid-State Physics and Electronics," Phys. Rev. Lett. **58**, 2059–2062 (1987).

[15] S. John, "Strong localization of photons in certain disordered dielectric superlattices," Phys. Rev. Lett. **58**, 2486–2489 (1987).

[16] J. D. Joannopoulos, S. G. Johnson, J. N. Winn, and R. D. Meade, *Photonic Crystals: Molding the Flow of Light (Second Edition)* (Princeton University Press, 2008), 2nd ed.

[17] T. Schreiber, J. Limpert, S. Nolte, H. Zellmer, A. Tunnermann, R. Iliew, F. Lederer, J. Broeng, G. Vienne, A. Petersson, and C. Jakobsen, "High-power air-clad large-mode-area photonic crystal fiber laser," Conf. Lasers Electro-Optics Eur. - Tech. Dig. **11**, 656 (2003).

[18] J. K. Ranka, R. S. Windeler, and A. J. Stentz, "Visible continuum generation in air–silica microstructure optical fibers with anomalous dispersion at 800 nm," Opt. Lett. **25**, 25 (2000).

[19] J. C. Knight, A. Bjarklev, and J. Broeng, "Photonic crystal fibres." Nature **424**, 847–51 (2003).

[20] P. S. J. Russell, "Photonic crystal fibers." Science **299**, 358–62 (2003).

[21] H. W. Lee, M. A. Schmidt, P. Uebel, H. Tyagi, N. Y. Joly, and P. S. J. Russell, "Optofluidic refractive-index sensor in step-index fiber with parallel hollow micro-channel." Opt. Express **19**, 8200–8207 (2011).

[22] H. K. Tyagi, H. W. Lee, P. Uebel, M. A. Schmidt, N. Joly, and P. S. J. Russell, "Plasmon resonances on gold nanowires directly drawn in a step-index fiber," Opt. Lett. **35**, 2573 (2010).

[23] F. Reinitzer, "Beiträge zur Kenntniss des Cholesterins," Monatshefte für Chemie - Chem. Mon. **9**, 421–441 (1888).

[24] O. Lehmann, "Über fliessende krystalle," Z. phys. Chem **4**, 462–472 (1889).

[25] H. Kawamoto, "The history of liquid-crystal displays," Proc. IEEE **90**, 460–500 (2002).

[26] C. Slinger, C. Cameron, and M. Stanley, "Computer-generated holography as a generic display technology," Computer (Long. Beach. Calif). **38**, 46–53 (2005).

[27] L. Scolari, T. T. Alkeskjold, J. Riishede, A. Bjarklev, D. Hermann, A. Anawati, M. Nielsen, and P. Bassi, "Continuously tunable devices based on electrical control of dual-frequency liquid crystal filled photonic bandgap fibers." Opt. Express **13**, 7483–7496 (2005).

[28] A. Lorenz, H.-S. Kitzerow, A. Schwuchow, J. Kobelke, and H. Bartelt, "Photonic crystal fiber with a dual-frequency addressable liquid crystal: behavior in the visible wavelength range." Opt. Express **16**, 19375–81 (2008).

[29] A. Lorenz, R. Schuhmann, and H.-S. Kitzerow, "Infiltrated photonic crystal fiber: experiments and liquid crystal scattering model." Opt. Express **18**, 3519–3530 (2010).

[30] T. Larsen, A. Bjarklev, D. Hermann, and J. Broeng, "Optical devices based on liquid crystal photonic bandgap fibres." Opt. Express **11**, 2589–96 (2003).

[31] T. T. Alkeskjold, J. Lægsgaard, A. Bjarklev, D. S. Hermann, J. Broeng, J. Li, S. Gauza, and S.-t. Wu, "Photonic Bandgap Fiber," Appl. Opt. **45**, 2261–2264 (2006).

[32] Y. Peng, J. Hou, Y. Zhang, Z. Huang, R. Xiao, and Q. Lu, "Temperature sensing using the bandgap-like effect in a selectively liquid-filled photonic crystal fiber." Opt. Lett. **38**, 263–5 (2013).

[33] S. Ertman, T. R. Woliński, D. Pysz, R. Buczynski, E. Nowinowski-Kruszelnicki, and R. Dabrowski, "Low-loss propagation and continuously tunable birefringence in high-index photonic crystal fibers filled with nematic liquid crystals." Opt. Express **17**, 19298–310 (2009).

[34] K. Szaniawska, T. Nasilowski, T. R. Woliński, and H. Thienpont, "Tunable properties of light propagation in photonic liquid crystal fibers," Opto-Electronics Rev. **14**, 339–343 (2006).

[35] M. Tefelska, M. Chychlowski, T. R. Woliński, R. Dkabrowski, and J. Wójcik, "Tunable attenuation in photonic liquid crystal fibers," Photonics Lett. Pol. **1**, 97–99 (2009).

[36] L. Wei, T. T. Alkeskjold, and A. Bjarklev, "Tunable and rotatable polarization controller using photonic crystal fiber filled with liquid crystal," Appl. Phys. Lett. **96**, 5–8 (2010).

[37] F. Luan, A. K. George, T. D. Hedley, G. J. Pearce, D. M. Bird, J. C. Knight, and P. S. J. Russell, "All-solid photonic bandgap fiber." Opt. Lett. **29**, 2369–2371 (2004).

[38] S. R. Petersen, T. T. Alkeskjold, and J. Lægsgaard, "Degenerate four wave mixing in large mode area hybrid photonic crystal fibers," Opt. Express **21**, 18111–18124 (2013).

[39] S. R. Petersen, T. T. Alkeskjold, C. B. Olausson, and J. Lægsgaard, "Extended parametric gain range in photonic crystal fibers with strongly frequency-dependent field distributions." Opt. Lett. **39**, 4891–4 (2014).

[40] P. J. Collings and M. Hird, *Introduction to liquid crystals* (Taylor & Francis, London, 2004).

[41] P. P. Crooker, "Blue Phases," in "Chirality Liq. Cryst.", H.-S. Kitzerow and C. Bahr, eds. (Springer Science \& Business Media, New York, 2001), pp. 186–222.

[42] W. Maier and A. Saupe, "Eine einfache molekular-statistische Theorie der nematischen kristallinflüssigen Phase. Teil I." Z. Naturforsch. **15A**, 882–889 (1959).

[43] W. Maier and A. Saupe, "Eine einfache molekular-statistische Theorie der nematischen kristallinflüssigen Phase. Teil II," Z. Naturforsch. **14A**, 287–292 (1960).

[44] P. Yeh and C. Gu, *Optics of Liquid Crystal Displays* (Wiley Publishing, 2009), 2nd ed.

[45] C. Hu and J. R. Whinnery, "Losses of a nematic liquid-crystal optical waveguide," J. Opt. Soc. Am. **64**, 1424 (1974).

[46] P. G. de Gennes and J. Prost, *The Physics of Liquid Crystals*, International Series of Monographs on Physics (Clarendon Press, 1995).

[47] C. Oseen, "The theory of liquid crystals," Trans. Faraday Soc. **29**, 883–889 (1933).

[48] F. C. Frank, "I. Liquid crystals. On the theory of liquid crystals," Discuss. Faraday Soc. **25**, 19 (1958).

[49] I. W. Stewart, *The Static and Dynamic Continuum Theory of Liquid Crystals: A Mathematical Introduction*, Liquid Crystals Book Series (CRC Press, 2004).

[50] E. G. Virga, *Variational Theories for Liquid Crystals*, Applied Mathematics (Taylor & Francis, 1995).

[51] R. P. Feynman, R. B. Leighton, and M. L. Sands, *The Feynman Lectures on Physics*, no. Vol 2 in The Feynman Lectures on Physics (Addison-Wesley, 1963).

[52] L. M. Blinov and V. G. Chigrinov, *Electrooptic effects in liquid crystal materials.* (Springer-Verlag, New York, 1994), 1st ed.

[53] M. Schadt, "Low-Frequency Dielectric Relaxations in Nematics and Dual-Frequency Addressing of Field Effects," Mol. Cryst. Liq. Cryst. **89**, 77–92 (1982).

[54] W. De Jeu, C. Gerritsma, P. Van Zanten, and W. Goossens, "Relaxation of the dielectric constant and electrohydro-dynamic instabilities in a liquid crystal," Phys. Lett. A **39**, 355–356 (1972).

[55] H. K. Bücher, "Frequency-addressed liquid crystal field effect," Appl. Phys. Lett. **25**, 186 (1974).

[56] W. H. De Jeu and T. W. Lathouwers, "Nematic Phenyl Benzoates in Electric Fields. II. Instabilities Around the Frequency of Dielectric lsotropy," Mol. Cryst. Liq. Cryst. **26**, 235–243 (1974).

[57] G. Baur, A. Stieb, and G. Meier, "Controlled decay of electrically induced deformations in nematic liquid crystals," Appl. Phys. **2**, 349–350 (1973).

[58] V. Fréedericksz and A. Repiewa, "Theoretisches und Experimentelles zur Frage nach der Natur der anisotropen Flüssigkeiten," Zeitschrift für Phys. **42**, 532–546 (1927).

[59] V. Fréedericksz and V. Zolina, "Forces causing the orientation of an anisotropic liquid," Trans. Faraday Soc. **29**, 919–930 (1933).

[60] D.-K. Yang and S.-T. Wu, *Fundamentals of Liquid Crystal Devices* (John Wiley & Sons, Ltd, Chichester, UK, 2014).

[61] Y. Cui, R. S. Zola, Y.-C. Yang, and D.-K. Yang, "Alignment layers with variable anchoring strengths from Polyvinyl Alcohol," J. Appl. Phys. **111**, 063520 (2012).

[62] J. Stöhr and M. Samant, "Liquid crystal alignment by rubbed polymer surfaces: a microscopic bond orientation model," J. Electron Spectros. Relat. Phenomena **98-99**, 189–207 (1999).

[63] I. M. Syed, G. Carbone, C. Rosenblatt, and B. Wen, "Planar degenerate substrate for micro- and nanopatterned nematic liquid-crystal cells," J. Appl. Phys. **98**, 1–5 (2005).

[64] M. Schadt, K. Schmitt, V. Kozinkov, and V. Chigrinov, "Surface-Induced Parallel Alignment of Liquid Crystals by Linearly Polymerized Photopolymers," Jpn. J. Appl. Phys. **31**, 2155–2164 (1992).

[65] H.-S. Kitzerow, B. Liu, F. Xu, and P. P. Crooker, "Effect of chirality on liquid crystals in capillary tubes with parallel and perpendicular anchoring," Phys. Rev. E **54**, 568–575 (1996).

[66] Apple Inc., "http://www.apple.com/imac/design/," (2016).

[67] V. P. Vorflusev, H.-S. Kitzerow, and V. G. Chigrinov, "Azimuthal Anchoring Energy in Photoinduced Anisotropic Films," Jpn. J. Appl. Phys. **34**, L1137–L1140 (1995).

[68] A. A. Sonin, *The Surface Physics of Liquid Crystals* (Gordon and Breach Publishers, 1995).

[69] J. Cognard, *Alignment of nematic liquid crystals and their mixtures*, Molecular crystals and liquid crystals: Supplement series (Gordon and Breach Science Publishers, 1982).

[70] G. Crawford, D. Allender, and J. Doane, "Surface elastic and molecular-anchoring properties of nematic liquid crystals confined to cylindrical cavities," Phys. Rev. A **45**, 8693–8710 (1992).

[71] J. D. Jackson, *Classical electrodynamics* (Wiley, New York, 1999), 3rd ed.

[72] A. W. Snyder and J. Love, *Optical Waveguide Theory*, Science paperbacks (Springer, 1983).

[73] J. A. Buck, *Fundamentals of Optical Fibers* (Wiley-Interscience, 2004), 2nd ed.

[74] M. Abramowitz and I. A. Stegun, *Handbook of Mathematical Functions with Formulas, Graphs, and Mathematical Tables* (Dover, New York, 1970), ninth dove ed.

[75] E. Snitzer, "Cylindrical dielectric waveguide modes," JOSA **51** (1961).

[76] R. Paschotta, "RP Photonics," (2016).

[77] C. Hussey and F. Martinez, "Approximate analytic forms for the propagation characteristics of single-mode optical fibres," Electron. Lett. **21**, 1103 (1985).

[78] S. E. Miller, "Coupled Wave Theory and Waveguide Applications," Bell Syst. Tech. J. **33**, 661–719 (1954).

[79] J. R. Pierce, "Coupling of Modes of Propagation," J. Appl. Phys. **25**, 179 (1954).

[80] J. R. Pierce, "The Wave Picture of Microwave Tubes," Bell Syst. Tech. J. **33**, 1343–1372 (1954).

[81] D. Marcuse, "The Coupling of Degenerate Modes in Two Parallel Dielectric Waveguides," Bell Syst. Tech. J. **50**, 1791–1816 (1971).

[82] A. A. Barybin and V. A. Dmitriev, *Modern Electrodynamics and Coupled-Mode Theory: Application to Guided-Wave Optics* (IOS Press, 2002).

[83] A. Hardy and W. Streifer, "Coupled mode solutions of multiwaveguide systems," IEEE J. Quantum Electron. **22**, 528–534 (1986).

[84] H. Haus, W. Huang, S. Kawakami, and N. Whitaker, "Coupled-mode theory of optical waveguides," J. Light. Technol. **5**, 16–23 (1987).

[85] B. E. Little and W. P. Huang, "Coupled-Mode Theory for Optical Waveguides," Prog. Electromagn. Res. **10**, 217–270 (1995).

[86] H. Haus, W. P. Huang, and A. W. Snyder, "Coupled-mode formulations." Opt. Lett. **14**, 1222–4 (1989).

[87] A. Hardy and W. Streifer, "Coupled mode theory of parallel waveguides," J. Light. Technol. **3**, 1135–1146 (1985).

[88] W. Streifer, M. Osinski, and a. Hardy, "Reformulation of the coupled-mode theory of multiwaveguide systems," J. Light. Technol. **5**, 1–4 (1987).

[89] A. Hardy, W. Streifer, and M. Osifiski, "Coupled-mode equations for multimode waveguide systems in isotropic or anisotropic media," Opt. Lett. **11**, 742–744 (1986).

[90] Shun-Lien Chuang, "A coupled-mode theory for multiwaveguide systems satisfying the reciprocity theorem and power conservation," J. Light. Technol. **5**, 174–183 (1987).

[91] A. W. Snyder, "Coupled-Mode Theory for Optical Fibers," J. Opt. Soc. Am. **62**, 1267 (1972).

[92] P. Yeh and A. Yariv, "Bragg reflection waveguides," Opt. Commun. **19**, 427–430 (1976).

[93] P. Yeh, A. Yariv, and E. Marom, "Theory of Bragg fiber*," J. Opt. Soc. Am. **68**, 1196 (1978).

[94] T. A. Birks, J. C. Knight, and P. S. J. Russell, "Endlessly single-mode photonic crystal fiber." Opt. Lett. **22**, 961–3 (1997).

[95] J. C. Knight, T. A. Birks, P. S. J. Russell, and J. P. de Sandro, "Properties of photonic crystal fiber and the effective index model," J. Opt. Soc. Am. A **15**, 748 (1998).

[96] D. C. Zografopoulos, R. Asquini, E. E. Kriezis, A. D'Alessandro, and R. Beccherelli, "Guided-wave liquid-crystal photonics," Lab Chip **12**, 3598 (2012).

[97] A. Wang, A. K. George, and J. C. Knight, "Three-level Neodymium fiber laser incorporating photonic bandgap fiber," Conf. Lasers Electro-Optics Quantum Electron. Laser 2006 **31**, 1–2 (2006).

[98] D. G. Lona, H. E. Hernández-Figueroa, A. Cerqueira S. Jr., G. Stefanini, and H. L. Fragnito, "Applicability of low macrobending loss hollow-core PCF to FTTH applications," J. Microwaves, Optoelectron. Electromagn. Appl. **10**, 251–258 (2011).

[99] T. A. Birks, D. M. Bird, T. Hedley, J. Pottage, and P. S. J. Russell, "Scaling laws and vector effects in bandgap-guiding fibres." Opt. Express **12**, 69–74 (2004).

[100] P. Domachuk, H. C. Nguyen, B. J. Eggleton, M. Straub, and M. Gu, "Microfluidic tunable photonic band-gap device," Appl. Phys. Lett. **84**, 1838 (2004).

[101] A. Lorenz, "Switchable waveguiding in photonic liquid crystal microstructures," Ph.D. thesis, Paderborn University (2010).

[102] R. F. Cregan, "Single-Mode Photonic Band Gap Guidance of Light in Air," Science (80-.). **285**, 1537–1539 (1999).

[103] F. Benabid, "Stimulated Raman Scattering in Hydrogen-Filled Hollow-Core Photonic Crystal Fiber," Science (80-.). **298**, 399–402 (2002).

[104] P. T. Marty, J. Morel, and T. Feurer, "Pulsed erbium fiber laser with an acetylene-filled photonic crystal fiber for saturable absorption," Opt. Lett. **36**, 3569 (2011).

[105] N. Y. Joly, J. Nold, W. Chang, P. Hölzer, A. Nazarkin, G. K. L. Wong, F. Biancalana, and P. S. J. Russell, "Bright spatially coherent wavelength-tunable deep-UV laser source using an Ar-filled photonic crystal fiber," Phys. Rev. Lett. **106**, 1–4 (2011).

[106] NKT Photonics, "www.nktphotonics.com," .

[107] P. S. J. Russell, "Photonic-Crystal Fibers," J. Light. Technol. **24**, 4729–4749 (2006).

[108] Y.-F. Li, C.-Y. Wang, and M.-L. Hu, "A fully vectorial effective index method for photonic crystal fibers: application to dispersion calculation," Opt. Commun. **238**, 29–33 (2004).

[109] G. K. Wong, a. Y. Chen, S. Ha, R. Kruhlak, S. Murdoch, R. Leonhardt, J. Harvey, and N. Joly, "Characterization of chromatic dispersion in photonic crystal fibers using scalar modulation instability." Opt. Express **13**, 8662–8670 (2005).

[110] F. Brechet, J. Marcou, D. Pagnoux, and P. Roy, "Complete Analysis of the Characteristics of Propagation into Photonic Crystal Fibers, by the Finite Element Method," Opt. Fiber Technol. **6**, 181–191 (2000).

[111] N. A. Mortensen, J. R. Folkenberg, M. D. Nielsen, and K. P. Hansen, "Modal cutoff and the V parameter in photonic crystal fibers." Opt. Lett. **28**, 1879–1881 (2003).

[112] M. Koshiba and K. Saitoh, "Applicability of classical optical fiber theories to holey fibers," Opt. Lett. **29**, 1739 (2004).

[113] M. Wahle, J. Ebel, D. Wilkes, and H.-S. Kitzerow, "Asymmetric band gap shift in electrically addressed blue phase photonic crystal fibers," Opt. Express **24**, 22718 (2016).

[114] N. M. Litchinitser, A. K. Abeeluck, C. Headley, and B. J. Eggleton, "Antiresonant reflecting photonic crystal optical waveguides." Opt. Lett. **27**, 1592–1594 (2002).

[115] N. M. Litchinitser, S. Dunn, P. Steinvurzel, B. J. Eggleton, T. White, R. McPhedran, and C. de Sterke, "Application of an ARROW model for designing tunable photonic devices." Opt. Express **12**, 1540–50 (2004).

[116] P. Steinvurzel, B. T. Kuhlmey, T. White, M. J. Steel, C. M. de Sterke, and B. J. Eggleton, "Long wavelength anti-resonant guidance in high index inclusion microstructured fibers," Opt. Express **12**, 5424 (2004).

[117] A. W. Snyder and D. J. Mitchell, "Leaky rays on circular optical fibers," J. Opt. Soc. Am. **64**, 599 (1974).

[118] A. W. Snyder, "Leaky-ray theory of optical waveguides of circular cross section," Appl. Phys. **4**, 273–298 (1974).

[119] R. Sammut and A. W. Snyder, "Leaky modes on circular optical waveguides." Appl. Opt. **15**, 477–82 (1976).

[120] N. M. Litchinitser, S. C. Dunn, B. Usner, B. J. Eggleton, T. P. White, R. C. McPhedran, and C. M. de Sterke, "Resonances in microstructured optical waveguides." Opt. Express **11**, 1243–51 (2003).

[121] J. Sun, C. Chan, and N. Ni, "Analysis of photonic crystal fibers infiltrated with nematic liquid crystal," Opt. Commun. **278**, 66–70 (2007).

[122] COMSOL, *www.comsol.com*.

[123] G. Ren, P. Shum, J. Hu, X. Yu, and Y. Gong, "Polarization-dependent bandgap splitting and mode guiding in liquid crystal photonic bandgap fibers," J. Light. Technol. **26**, 3650–3659 (2008).

[124] K. Busch and S. John, "Photonic band gap formation in certain self-organizing systems," Phys. Rev. E **58**, 3896–3908 (1998).

[125] T. A. Birks, G. J. Pearce, and D. M. Bird, "Approximate band structure calculation for photonic bandgap fibres." Opt. Express **14**, 9483–9490 (2006).

[126] K. Saitoh and M. Koshiba, "Empirical relations for simple design of photonic crystal fibers." Opt. Express **13**, 267–74 (2005).

[127] K. Inoue and H. Toba, "Wavelength conversion experiment using fiber four-wave mixing," IEEE Photonics Technol. Lett. **4**, 69–72 (1992).

[128] S. Yoo, "Wavelength conversion technologies for WDM network applications," J. Light. Technol. **14**, 955–966 (1996).

[129] J. G. Rarity, J. Fulconis, J. Duligall, W. J. Wadsworth, and P. S. J. Russell, "Photonic crystal fiber source of correlated photon pairs," Opt. Express **13**, 534 (2005).

[130] J. Fulconis, O. Alibart, J. O'Brien, W. J. Wadsworth, and J. Rarity, "Nonclassical Interference and Entanglement Generation Using a Photonic Crystal Fiber Pair Photon Source," Phys. Rev. Lett. **99**, 120501 (2007).

[131] C. Söller, B. Brecht, P. J. Mosley, L. Y. Zang, A. Podlipensky, N. Y. Joly, P. S. J. Russell, and C. Silberhorn, "Bridging visible and telecom wavelengths with a single-mode broadband photon pair source," Phys. Rev. A **81**, 031801 (2010).

[132] W. Tittel, J. Brendel, H. Zbinden, and N. Gisin, "Quantum Cryptography Using Entangled Photons in Energy-Time Bell States," Phys. Rev. Lett. **84**, 4737–4740 (2000).

[133] N. Gisin and R. Thew, "Quantum communication," Nat. Photonics **1**, 165–171 (2007).

[134] G. P. Agrawal, "Four-Wave Mixing," in "Nonlinear Fiber Opt.", G. P. Agrawal, ed. (Elsevier, San Diego, 2006), Optics and Photonics, pp. 368–423, 4th ed.

[135] Merck KGaA, "Data sheet," (2003).

[136] EVONIK Industries, "Dynasylan ® GLYMO Datasheet," .

[137] D.-K. Yang and S.-T. Wu, *Fréedericksz Transition* (John Wiley & Sons, Ltd, Chichester, UK, 2014), pp. 149–189.

[138] F. Du, Y.-Q. Lu, and S.-T. Wu, "Electrically tunable liquid-crystal photonic crystal fiber," Appl. Phys. Lett. **85**, 2181 (2004).

[139] M. Haakestad, T. T. Alkeskjold, M. Nielsen, L. Scolari, J. Riishede, H. Engan, and A. Bjarklev, "Electrically tunable photonic bandgap guidance in a liquid-crystal-filled photonic crystal fiber," IEEE Photonics Technol. Lett. **17**, 819–821 (2005).

[140] P. D. Rasmussen, J. Lægsgaard, and O. Bang, "Chromatic dispersion of liquid-crystal infiltrated capillary tubes and photonic crystal fibers," J. Opt. Soc. Am. B **23**, 2241 (2006).

[141] J. Sun and C. C. Chan, "Effect of liquid crystal alignment on bandgap formation in photonic bandgap fibers." Opt. Lett. **32**, 1989–91 (2007).

[142] G. Ren, P. Shum, X. Yu, J. Hu, G. Wang, and Y. Gong, "Polarization dependent guiding in liquid crystal filled photonic crystal fibers," Opt. Commun. **281**, 1598–1606 (2008).

[143] J. J. Hu, G. Ren, P. Shum, X. Yu, G. Wang, and C. Lu, "Analytical method for band structure calculation of photonic crystal fibers filled with liquid crystal." Opt. Express **16**, 6668–74 (2008).

[144] G. Ren, P. Shum, J. Hu, X. Yu, and Y. Gong, "Polarization-Dependent Bandgap Splitting and Mode Guiding in Liquid Crystal Photonic Bandgap Fibers," J. Light. Technol. **26**, 3650–3659 (2008).

[145] P. D. Rasmussen, J. Laegsgaard, and O. Bang, "Degenerate four wave mixing in solid core photonic bandgap fibers." Opt. Express **16**, 4059–4068 (2008).

[146] J. Zhao, P. Yan, J. Shu, C. Du, S. Ruan, H. Wei, and J. Luo, "Efficient anti-stokes signal generation through degenerate four wave mixing in an all solid photonic bandgap fiber," Opt. Commun. **284**, 5208–5211 (2011).

[147] S. R. Petersen, T. T. Alkeskjold, C. B. Olausson, and J. Lægsgaard, "Polarization switch of four-wave mixing in large mode area hybrid photonic crystal fibers," Opt. Lett. **40**, 487 (2015).

[148] M. Vieweg, T. Gissibl, S. Pricking, B. T. Kuhlmey, D. C. Wu, B. J. Eggleton, and H. Giessen, "Ultrafast nonlinear optofluidics in selectively liquid-filled photonic crystal fibers," Opt. Express **18**, 25232 (2010).

[149] Y. Wang, D. N. Wang, F. Yang, Z. Li, and M. Yang, "Sensitive hydrogen sensor based on selectively infiltrated photonic crystal fiber with Pt-loaded WO_3 coating," Opt. Lett. **39**, 3872 (2014).

[150] J. H. Liou, S. S. Huang, and C. P. Yu, "Loss-reduced highly birefringent selectively liquid-filled photonic crystal fibers," Opt. Commun. **283**, 971–974 (2010).

[151] B. Sun, Z. Zhang, W. Wei, C. Wang, C. Liao, L. Zhang, and Y. Wang, "Unique Temperature Dependence of Selectively Liquid-Crystal-Filled Photonic Crystal Fibers," IEEE Photonics Technol. Lett. **28**, 1282–1285 (2016).

[152] K. S. Kim, W. A. Reed, K. W. Quoi, and R. H. Stolen, "Measurement of the nonlinear index of silica-core and dispersion-shifted fibers," Opt. Lett. **19**, 257 (1994).

[153] H. Kikuchi, M. Yokota, Y. Hisakado, H. Yang, and T. Kajiyama, "Polymer-stabilized liquid crystal blue phases." Nat. Mater. **1**, 64–8 (2002).

[154] M. Wahle and H.-S. Kitzerow, "Liquid crystal assisted optical fibres," Opt. Express **22**, 262 (2014).

[155] M. A. Schmidt, A. Argyros, and F. Sorin, "Hybrid Optical Fibers - An Innovative Platform for In-Fiber Photonic Devices," Adv. Opt. Mater. **4**, 13–36 (2016).

[156] I. H. Malitson, "Interspecimen Comparison of the Refractive Index of Fused Silica," J. Opt. Soc. Am. **55**, 1205 (1965).

[157] J. W. Fleming, "Dispersion in GeO 2 -SiO 2 glasses," Appl. Opt. **23** (1984).

[158] Y.-Y. Kao and P. C.-P. Chao, "A New Dual-Frequency Liquid Crystal Lens with Ring-and-Pie Electrodes and a Driving Scheme to Prevent Disclination Lines and Improve Recovery Time," Sensors **11**, 5402–5415 (2011).

[159] Y. W. Li and H. S. Kwok, "Bistable twisted-bend and twisted-nematic liquid crystal display," Appl. Phys. Lett. **95** (2009).